NASA CR-143827

(NASA-CR-143827) ELECTRONIC MAGNIFICATION FOR ASTRONOMICAL CAMERA TUBES Final Report (Westinghouse Research Labs.) 144 p HC $5.75 CSCL 03A
N75-29961
Unclas
G3/89 33008

NAS5-20511

ELECTRONIC MAGNIFICATION FOR ASTRONOMICAL CAMERA TUBES

J. Vine, J. R. Hansen, J. P. Pietrzyk

Westinghouse Research Laboratories
Westinghouse Electronic Tube Division

FINAL REPORT

December 1974

National Aeronautics & Space Administration
Goddard Space Flight Center
Greenbelt, Maryland

NAS5-20511

ELECTRONIC MAGNIFICATION FOR ASTRONOMICAL CAMERA TUBES

J. Vine, J. R. Hansen, J. P. Pietrzyk

Westinghouse Research Laboratories
Westinghouse Electronic Tube Division

FINAL REPORT

December 1974

National Aeronautics & Space Administration
Goddard Space Flight Center
Greenbelt, Maryland

Westinghouse
Electric Corporation

Research and Development Center
RESEARCH LABORATORIES
Beulah Road
Pittsburgh Pennsylvania 15235

National Aeronautics & Space Administration
Goddard Space Flight Center
Greenbelt Road
Greenbelt, Maryland 20771

Attention: Hugh K. Warren, 286
Contracting Officer

Reference: Contract NAS5-20511, Electronic Magnification for Astronomical Camera Tubes

Transmitted herewith is one (1) copy of the Final Report. Distribution of these reports to the other designated recipients is shown below.

NASA Goddard Space Flight Center
Greenbelt Road
Greenbelt, Maryland 20711

	Final Report
Systems Reliability Directorate	1
Space & Earth Sciences Directorate	1
Publication Branch	1
Patent Counsel	1
Carole Scott - 604	1
T. Kelsall - 601	22
Reproducible Copy: Documentation Center Code 256	1

C. F. Wood, Manager
Problem Analysis
Computer Sciences

mms

Attachment

TABLE OF CONTENTS

ELECTRONIC MAGNIFICATION FOR ASTRONOMICAL CAMERA TUBES

J. Vine, J. H. Hansen, J. P. Pietrzyk

Westinghouse Research Laboratories
Westinghouse Electronic Tube Division

1. INTRODUCTION

This is the final report on Contract NAS5-20511 with the Goddard Space Flight Center of NASA. The program's objectives are to define, analyze and test schemes to provide variable magnification in the image section of the television sensor for the Large Space Telescope (LST). The reference sensor for the study is the Westinghouse WX32193 SEC camera tube. The work statement defined the following five tasks:

Task 1

Perform a parametric study relating magnetic field pattern and electron optic trajectories with special emphasis on aberrations and distortions for different field configurations.

Task 2

Provide the design for a system incorporating solenoids external to the sensor to allow photocathode to target magnifications of 1X and 4X (nominal values).

Task 3

Analyze in explicit terms the interaction of the solenoids controlling magnification and those producing the focus within the image section. How must the focus field be altered as the magnification is changed (in discrete steps).

Task 4

Demonstrate the imaging properties of the proposed design utilizing a laboratory test camera system expressing the results in terms of the modulation transfer function (MTF) for edge and central image plane. Field distortions shall be quantitatively expressed.

Task 5

Power requirements including stability, range, and ripple content shall be specified. Environmental effects particularly thermal perturbation caused by the electronic magnification system shall be investigated and described.

The LST application involves the TV transmission of star-field images and high resolution spectra, over a range of wavelengths from 100 to 1000 nm. This will require the use of more than one camera. As extremely low light levels are involved, an image will be integrated on the SEC target of a tube for a period of minutes to many hours before read-out with a single slow scan of several seconds duration. The ability to zoom from unit magnification to 4X magnification in the sensor is seen as an economical method of increasing the flexibility of the instrument, permitting effectively a choice of f number to suit a particular observation.

The WX32193 is a magnetically focussed camera tube with a large SEC (Secondary Electron Conduction) target, 2" by 2.2" (nominal image field 50 x 50 mm). It was designed for nominally unit magnification in the image section, and employs a direct-beam read-out section based on an orthodox vidicon design. It can be manufactured with glass or magnesium fluoride input windows, as appropriate to the wavelength range of application. The slow-scan read-out mode of operation permits high resolution to be achieved. This is characterized by a current working figure of 50% response at 20 line-pairs/mm for the modulation transfer function (MTF). In its standard operating mode the tube employs a nominal 80 gauss magnetic field for focussing both image and reading sections. In a preliminary investigation, J. L. Lowrance has shown(1) that the use of a booster coil in front of the tube to strengthen the field at the photocathode can give a magnification of 2.7 in the image section.

The approach adopted to tasks 1, 2, and 3 of the work statement is computational, employing a well-established computer program package that has been developed at Ⓦ Research Laboratories in recent years.(2) These programs permit accurate computational modelling of electrode and coil configurations, and produce output of the main electron-optical imaging properties in a concise form. Their use provides a rapid "turnaround" between design concept and performance evaluation, which is very advantageous for exploratory work. A brief outline of the programs is given in Appendix 1. The experimental work of tasks 4 and 5 was broadened to include the manufacture and testing of image intensifier tubes with phosphor viewing screens, in addition to camera tube demonstration. The reason is that imaging assessment is more accurate by direct viewing than by camera-tube read-out, due to fewer variables in the system. In addition, as camera tube testing had to be carried out on special test-sets at Ⓦ Tube Division in Elmira, it was felt that an image tube test system set up at the Research Laboratories would facilitate interaction between the computational and experimental programs. The work reported falls into three main parts, computational, image tube testing, and camera tube testing. These are dealt with in order in Section 3, 4, and 5.

The principal result of the computational study is a clear definition of the form of magnetic field distribution necessary to achieve magnification in the range 3X to 4X. Coil systems to establish the required field shapes were built, and both image intensifiers and camera tubes were operated at high magnification. The experiments confirmed that such operation is practical and can provide satisfactory image quality. The main problem is identified as heating of the photocathode due to concentration of coil power dissipation in that vicinity. Suggestions for overcoming this problem are made. The conclusions and recommendations are given in greater detail in Sections 7 and 8.

2. ELECTRON OPTICS BACKGROUND

The purpose here is to establish some basic concepts to assist understanding of the main body of the report, and to collect together important equations and definitions for later reference.

Magnetic focusing - The image intensifier focusing relation is

$$z_{fn} = 10.6\ n\ V_T^{1/2}/B \tag{2.1}$$

for the n-loop focal length (cm) where V_T is the final (target) voltage, and B is the magnetic field strength (gauss), both fields being assumed to be uniform. In this report n = 1, there being no particular advantages offered by multi-loop focusing. For non-uniform field distributions the constant on the right changes but the form of the relationship remains if B represents field strength at some particular point (say B_c for the value at the photocathode). The constant can be established for given shapes of the two field distributions, and Equation (2.1) is of general utility for calculating the effects of scaling the absolute values of the fields, e.g., to maintain a given focal length at twice the magnetic field strength requires four times the target voltage.

Magnification and radial distortion - The ray-tracing computer program traces a principal ray from a point on the object (photocathode) to a point on the image and calculates a magnification M defined as

$$M = \frac{r_{out}}{r_{in}} \tag{2.2}$$

the ratio of the radial coordinates of image and object points. This is a function of r. If M(r) is the magnification at radius r, the percentage radial distortion D(r) is defined by

$$D(r) = 100[M(r)/M(0) - 1] \tag{2.3}$$

M(0) being the paraxial magnification. In this report magnification is to be taken as meaning M(0) unless otherwise stated. It is emphasized that D is not a coefficient, but a function of r, because in the large-area imaging involved in image tubes, aberrations are usually not restricted to third-order. The complete aberrations must be considered, and these cannot be characterized by simple coefficients. Values of D quoted in this report usually refer to the corner of the image field of interest, i.e. r_{out} = 3.5 cm (note that the value of r_{in} corresponding to this depends on the magnification of the particular case being discussed).

Rotation and S-distortion - Figure 2.1 shows a view of the electron-optical system looking in the positive direction along the axis of symmetry. Let the origin of coordinates be the center of the object plane and consider the imaging of the x-axis. A point with coordinate x_o images into one with coordinates x_1, y_1 and the rotation ϕ is defined by

$$\tan \phi = y_1/x_1 \tag{2.4}$$

This is a function of x_o, and so the line image is curved as shown. Usually the term rotation is used in this report to mean the paraxial value ϕ_o shown in Figure 2.1. The variation of ϕ with r at the output is the

S-distortion. The total angular error $\Delta\phi$ at radius r is defined as

$$\Delta\phi = \phi(r) - \phi_o \qquad (2.5)$$

Values quoted for this will usually refer to the corner point r_{out} = 3.5 cm. Unlike the radial distortion, the S-distortion is in many cases observed to be dominated by the third-order contribution, as a result of which $\Delta\phi$ is almost proportional to r^2, so that a coefficient S can be defined by

$$\Delta\phi = Sr_{out}^2 \qquad (2.6)$$

In some instances S (in rad/cm^2) is quoted instead of $\Delta\phi$.

Resolution - In an image-intensifier resolution is influenced by statistical properties of the spectral distribution of the incident radiation and the energy distribution of the photoelectrons. These present a complex problem, a rigorous solution of which can only be valid for specifically defined operating conditions, and must be expressed in the form of a point-spread function. To avoid these complications the computer program used in this study makes use of the concept of a typical electron emission energy ε, corresponding to emission velocity v, in order to quantify in a simple way the important electron-optical effects relating to resolution. At the first-order focus on the axis of the imaging system the size of the confusion disk is dominated by the chromatic aberration, which is an effect of second-order in v the emission velocity (i.e., proportional to emission energy ε). The confusion disk diameter can be written

$$d_o = 2\varepsilon/(eE) \tag{2.7}$$

where E is the electric field strength at the object point. This is the disk size referred to the object (photocathode) (Note: ε/e expresses the emission energy in volts). To derive the disk size at the image this would be multiplied by M. Equation (2.7) is the calculation done by the computer program but, to make the result more immediately meaningful, it is inverted and expressed as limiting resolution in line-pairs/mm. Use of the same value for ε in all computations allows meaningful comparisons to be made <u>between computations</u> of different cases. Experience has shown that these results can further be <u>roughly</u> related to practical results for visible-response photocathodes by choice of the value $\varepsilon = 0.2$ electron volts. It must be stressed that these are strictly "ballpark" estimates and that they refer to electron optical capability only, with no allowance for other components in the system, such as the phosphor screen of an intensifier tube.

At points off axis, in the plane of the paraxial focus, there is a contribution to the confusion disk that is of first-order with respect to v (i.e. proportional to $\varepsilon^{1/2}$), which can be written

$$d_1 = c_1\left(\frac{\varepsilon}{eE}\right)^{1/2} \tag{2.8}$$

where c_1 is a function of r_{in}. For a given object point the computer program computes c_1, and hence d_1, in the course of tracing the principal ray. It then combines this disk with the chromatic disk according to the formula

$$d = (d_o^2 + d_1^2)^{1/2} \qquad (2.9)$$

to obtain the total disk diameter estimate. Close to the axis, d_1 is negligible and d is effectively equal to d_o. Typically d_1 increases quite rapidly with r_{in} and becomes dominant at the edges of the field. In considering the question of resolution variation with tube operating voltage V it should be noted from equations (2.7) and (2.8) that d_o and d_1 vary inversely as V and $V^{1/2}$ respectively. Hence the center resolution varies directly as V while edge resolution will vary usually as $V^{1/2}$, with points between varying at a rate intermediate between the two.

As well as being a function of r_{in}, c_1 is dependent on the direction of electron emission in the object plane--the astigmatic effect. For each object point the computer program carries out the process described for the two cases of radial and tangential emission directions, and expresses the results as the limiting resolution estimates for tangential and radial lines respectively.

3. COMPUTATIONAL STUDY

The reference sensor is an existing camera tube of essentially fixed design, and so work is restricted mainly to manipulating the image by means of electromagnetic coils around the image section, while maintaining the standard uniform E-field distribution. Consideration of the use of non-uniform E-field distributions is of secondary importance, and is described separately in Section 3.8. The order of the following sub-sections represents a compromise between a logical and a chronological presentation.

3.1 E-Field Computer Model

Figure 3.1 shows the electrode model used to compute the electrostatic field distribution in the WX32193 image section (see Figure 6.1). The interior walls of the ceramic section of the tube are all coated with a conducting layer (chrome oxide) which provides a very high resistance leakage path from cathode to target, preventing charge build-up. The electrode voltages are imposed externally by a high resistance potential divider, and the conductive coating is assumed to set up a linear variation of electrostatic potential at the wall between each pair of adjacent electrodes. As the Kovar washers are thin, this arrangement is capable of a very high degree of field uniformity, provided the applied electrode voltages are proportional to distance from the cathode (throughout this report voltages and electrostatic potential are measured with respect to the photocathode as zero). The most significant disturbance of field uniformity would arise from the center cylindrical copper section in which the exhaust tubulation is mounted.

In view of the high degree of field uniformity, the computer model is set up with a rather coarse relaxation net of 2.74 mesh/cm which is shown superimposed in Figure 3.1. The computational origin is the center of the cathode, relative to which the target is represented at z = 32.2 mesh, corresponding to the original design dimension 11.8 cm. This was held throughout most of the computational study, although the cathode-target design figure increased slightly during the project as a result of constructional modification, reaching the value 12.8 cm in the third image intensifier built. The washer electrodes are represented as thin, and the relative potential settings shown in the figure are calculated in proportion to z-coordinate. The relative electrode potentials establish the field shape, absolute voltage level being important only for ray tracing. At mesh points on the outer wall represented by the dotted line, linear potential variation between electrodes was impressed. As expected, the field solution obtained was highly uniform over the active region of the tube (out to r = 9 mesh), showing just slight disturbance close to the central cylindrical electrode. This solution was used as the standard for the entire study, except for that part specifically concerned with the effect of non-uniform E-fields, described in Section 3.8. Ray tracing tests performed early in the project indicated the degree of E-field non-uniformity in the standard solution to be practically negligible (see Section 3.3). In fact, advantages might have been obtained by building this uniformity algebraically into the ray tracing computer program in place of the standard interpolation procedures on the numerical solution.

3.2 B-Field Computation

The magnetic field configuration is defined to the ray tracing program by specifying the on-axis field values at a set of evenly spaced points by means of a data array BA. The computer program employs numerical interpolation and differentiation on this array to generate the field components at an arbitrary electron position via the expansion formulas given in Appendix A1.2.2. Three different ways are available for setting up the array BA, corresponding essentially to three different versions of the program:

(a) direct input

(b) algebraic definition

(c) solenoid system

(a) The field values at evenly spaced points along the axis of the system are specified as data to the program. These mav be, for example, empirical values, so that a means is provided for assessing the imaging properties of a practical system as is described in Section 3.3. Another possibility is that the data array is generated by a separate computer program for magnetic field computation.

(b) The input of a relatively small number of parameters defines an algebraic form for the axial field distribution, by means of which the BA values are calculated. This method was devised for this project as a convenient means of varying field shape in a general way, divorced from practical considerations of establishment of the field. In Section 3.4 use is made of polynomial forms of different degrees up to 3. Consider the cubic form

$$B_z(z) = B_c\ (1 + a_1z+a_2z^2 + a_3z^3) \qquad (3.1)$$

where B_c is the field at the photocathode ($z = 0$). This form has apparently 4 degrees of freedom corresponding to choice of the four coefficients B_c, a_1, a_2, a_3. However, B_c is used by the program to establish a paraxially focused condition at the operating voltage specified. It is simply a scaling factor that adjusts the absolute level of the field without affecting the shape of the distribution (the operating voltage of the tube, also an input quantity to the ray tracing program, acts equivalently on the E-field as mentioned in Section 3.1). Thus, three degrees of freedom remain to fix the shape of the axial magnetic field distribution. Inspection of equation 3.1 shows that a_1 is simply proportional to the slope of the field at the cathode,

$$a_1 = B_c'/B_c \ (= b_c') \tag{3.2}$$

As a_2 and a_3 are not very convenient the program is arranged to accept instead two other parameters

$$b_1 = B_1/B_c$$

$$b_1' = B_1'/B_c$$

where B_1 and B_1' are respectively the field and its gradient at a specified on-axis point of coordinate z_1. The input parameters b_c',b_1, and b_1' , are related to a_1,a_2,a_3 by equation (3.2), together with two equations that follow from (3.1).

$$b_1 = 1 + a_1z_1 + a_2z_1^2 + a_3z_1^3 \tag{3.4}$$

$$b_1' = a_1 + 2a_2z_1 + 3a_3z_1^2$$

The program uses the inverse of this transformation to obtain a_1,a_2,a_3, and hence the data array BA.

Similar means are provided for setting up second and first degree polynomial forms for B_z. In the second degree case only the parameters b_c' and b_1 are used, and in the linear case only the parameter b_1.

(c) The geometrical parameters and current densities for one or more solenoids are specified and the program computes the axial field solution as a preliminary task. This is a straightforward process described elsewhere.(3) It is capable of accuracy limited only by that of the solenoid data. This method provides a convenient means of relating field shape and imaging properties to particular practical systems such as those used in the camera and image tube tests conducted under this project. However, it is not applicable if the field is affected by the presence of ferromagnetic material (the latter problem may be handled by a relaxation type program similar to that used in E-field computation - see Section 3.5).

3.3 Preliminary Assessment of Normal Operating Mode

At the start of the computational study it was decided to make an assessment of the image section performance in the design mode of operation. The standard Penntran focusing coil was operated with a current of 258 mA, without a tube in, and measurements made of the field strength as a function of position along the axis of the system. The distribution obtained is shown in Figure 3.2 (curve 1) where the z-coordinate is referenced to the normal photocathode location at 1" from the front end of the coil. The field strength displays a rather steep rise at the cathode. Readings from this curve at 1 cm intervals were fed to version (a) of the ray-tracing program. The more significant imaging properties estimated for the system are summarized by Figure 3.3 in which (a) shows the magnification M and distortion D, and (b) shows the limiting resolution, all as functions of image point radius at the target. Magnification is slightly less than 0.9 at the center and increases all the way to the edge. At 3 cm radius the distortion level is close to 4% and is likely to be above 5% in the corner of our image field (r = 3.5 cm, not included in this particular computer run). This is at the high end of what is usually considered to be an acceptable distortion range and implies a visually noticeable pin-cushion effect. Figure 3.3 (b) shows the limiting resolution capability falling very sharply outside of the paraxial imaging region. Beyond 1 cm radius this is likely to be a significant limiting factor in overall camera tube performance.

These results raise the question as to what extent the image faults are attributable to the magnetic field distribution or to slight imperfections in the E-field discussed in Section 3.1. Therefore, the computation was repeated with a perfectly uniform magnetic field. In this case, over the same image area, the distortion was found to be below 0.1%, and the limiting resolution above 160 line-pairs/mm - practically perfect image uniformity. Hence, the imaging non-uniformities displayed in Figure 3.3 are entirely due to the magnetic field shape, in particular the steep rate of change at the cathode surface.

Returning to Figure 3.2, curve 2 shows the results of a further experiment with the Penntran coil conducted late in the program, this time with an open-ended camera tube in position. The current reading in this case was 250 mA. The fact that the two curves were taken at different times by different operators leaves room for doubt about their comparability, but there is obviously a suggestion that the field shape may be quite noticeably modified by the presence of the Kovar elements in the tube structure. A check computation of imaging properties has been made using curve 2. The results, while different in detail, are qualitatively similar to those from curve 1. The conclusion is that further design work is warranted to improve magnetic field uniformity in the image section in the standard operating mode. The simple expedient of locating the photocathode deeper in the Penntran coil, say another 1", should improve matters, but that ignores the requirements of the reading section.

3.4 Study of Algebraically Defined B-Field

The magnification study proper was started by considering general algebraic forms for the axial B-field shape, using version (b) of the ray tracing program described in Section 3.2. The computer program permits any polynomial form up to degree 3 to be used. Initially the simplest case was chosen, of a linear variation of magnetic field from a value B_c at the cathode to the value B_T at the target.

3.4.1 Linear variation of B-field

As discussed in Section 3.2, a linear field variation implies a one-parameter study. A single case is specified to the ray tracing program by choice of the parameter $b_1 = B_T/B_c$, the ratio of field strengths at target and cathode, the operating voltage being fixed. For a given b_1 and operating voltage V_T, there is a particular field strength B_c that will produce a single-loop paraxial focus condition at the target. Corresponding to this focused condition there is a particular magnification value M. The ray tracing program conducts an iterative procedure to establish the focus field B_c, at the same time computing the magnification M. Then, with B_c at the paraxial focus value, it computes the imaging properties at off-axis points specified by the user.

The paraxial results for a range of values of b_1 are summarized in Figure 3.4 which shows the variation of focus field B_c, magnification M, and image rotation ϕ. The operating voltage assumed is 8 KV, and the cathode-target distance $z_T = 11.8$ cm. The case $b_1 = 1$ is the uniform field condition. As b_1 decreases, M, B_c and ϕ increase. At $B_T = 0$ the value $M = 1.72$ obtains. The main region of interest is where $b_1 < 0$, which implies that B_T is reversed in direction. M reaches a maximum of 2.3 where B_T is approximately equal and opposite to B_c. The focus field B_c is in the region 120 to 130 gauss at this peak. Image rotation always occurs to some extent with non-unit magnification. Throughout this work uniform rotation has been regarded as of no great consequence and is frequently omitted from the results that follow. In connection with the possible development of a zoom system, however, it should be appreciated that change in M will almost invariably involve image rotation, which means that the orientation of the circular image field at the target changes with respect to the scanning raster, so that the image contents of the rectangular scanned area are not readily predictable between one magnification and another.

The off-axis properties for this series of results will not be presented in detail. They are generally good in the region $b_1 \geq -1.0$, but to the left of the magnification peak in Figure 3.4 they deteriorate rapidly. For example, between $b_1 = -1$ and $b_1 = -1.25$ the radial distortion changes from - 1% to -74%, and the S-distortion becomes greater than 4 radians (being the image rotation difference between center and edge). In practice the useable image area would be too small to be of any value, and so the region $b_1 < -1$ is considered to be of no practical interest.

The tentative proposition made from these results was that equal and opposite field strengths at cathode and target might be a good condition for the attainment of high magnification. Subsequent experience has largely denied this, but it is mentioned to explain the course of some of the work that follows. In fact, more attention should probably have been paid to the parameter $b_c' = B_c'/B_c$, a point that will be developed later.

3.4.2 Parabolic B-field

The study of a second degree variation for $B_z(z)$ is a 2-parameter study, requiring for each case the selection of the parameters b_1 and b_c' defined in Section 3.2. Systematic exploration of this two-dimensional parameter space was not considered to be economically feasible. Taking a lead from the results of the preceding section, the value of b_1 was first set at - .75, close to, but safely to the right of, the peak of the M curve in Figure 3.4. A series of computations was made for different values of b_c', the results of which are summarized in the following table.

Parabolic B-Field Distribution

$b_1 = -.75$, $V_T = 8$ KV, $z_T = 11.8$ cm

b_c' (cm^{-1})	B_c (gauss)	M	ϕ (radians)	D%	S (radians cm^{-2})
-.149	124	2.29	-1.08	+3.2	-.009
-.17	129	2.38	-1.22	+2.5	-.012
-.20	135	2.49	-1.38	-1.0	-.021
-.22	139	2.52	-1.49	-6.8	-.033
-.25		2.51			

The values of M and B_c are plotted against b_c' in Figure 3.5. The first case in the table corresponds to the linear B-field case for this value of b_1, while the following cases follow a progressively steeper field gradient at the cathode. Here the magnification reaches a peak of $M = 2.5$ at $b_c' = -.22$. For steeper field gradients ($b_c' < -.22$) the image quality deteriorates very quickly, just as it does to the left of the peak in the M curve in Figure 3.4. The magnification peak in this case is somewhat higher than that reached in the linear B-field study, and the required focus field is correspondingly higher.

The chronological sequence of work proceeded from here to the consideration of a cubic form for the B-field, the results of which are described in the following section. However, it is appropriate to include here a second sequence of computations for the parabolic case which was actually conducted later in the project. This sequence is for the fixed value $b_1 = 0$ (zero field strength at the target), still with 8 KV operating voltage. The results are displayed in Figure 3.6 where (a) shows the focus field B_c and magnification, and (b) shows the distortions D and S, all as functions of b_c'. The results are generally similar to those already presented, with M increasing as the cathode gradient steepens, to a maximum beyond which image quality becomes unacceptable as the magnification decreases again. In this case, however, a much higher magnification peak of 3.2 obtains, to the right of which, $b_c' \simeq -.25$, magnification of about 3 is attained with quite low image distortions. In the latter case also the resolution uniformity is estimated to be very good, with a corner value ($r_{out} = 3.5$ cm) of better than 40 line-pairs/mm (referred to the photocathode, as are all resolution figures quoted here unless specifically stated otherwise). The magnetic field distributions for 3 cases in this sequence $b_c' = -.2, -.25$ and $-.3$, are shown in Figure 3.7. In each case the magnetic field reverses direction in the image section and reverses again at the target, assuming the original direction in the reading section of the camera tube. Best imaging occurs for a first reversal at about 5.5 to 6 cm from photocathode. Of all the algebraic forms studied, this set appears to represent the most promising basis for development of a practical system with magnification greater than 3.

3.4.3 Cubic B-field

As in the parabolic case, no systematic search through the parameter space (in this case 3-dimensional) could be contemplated. The approach adopted was to take some more or less random stabs and try to detect significant trends. Influenced by the results of the linear study (Section 3.4.1) the value of b_1 was fixed at $-.75$ while the parameters b_c' and b_1' ($= B_T'/B_c$) were varied. Some results for magnification as a function of b_1' are displayed in Figure 3.8 (a), where each curve corresponds to a different value of b_c'. Each curve has a maximum for some value of b_1', and the steeper the gradient b_c', the higher is the peak magnification attained. As might be expected from description of earlier results, operating conditions to the left of the peak values show unuseable imaging qualities. Figure 3.8 (b) shows the variation of the distortion parameters with b_1' for the particular case $b_c' = -.35\ \text{cm}^{-1}$. Both D and S pass through zero but not, unfortunately, at the same value of b_1'. It is worthy of record that the position of zero S, $b_1' = -.28$ cm^{-1} was found to be constant over the range of values of b_c' considered. For the case $b_c' = -.35$ cm^{-1}, Figure 3.9 shows the field configurations for the two extreme conditions of $b_1' = -.149$ and $-.35$. At the time these results were obtained, the latter case was singled out as being of particular interest. It can be seen from Figure 3.8 to provide M = 3 with possibly acceptable distortion levels, and was also estimated to have extremely good resolution uniformity, maintaining better than 70 line-pairs/mm over the entire image field. This interest reduced subsequently following consideration of power requirements, and in view of developments from the parabolic cases of Figure 3.7 which probably represent a better performance/power optimum.

3.4.4 Conclusions

The main conclusion drawn from this part of the study is that the achievement of high magnification ($M \geq 3$) requires a strong magnetic field at the cathode, with a high negative field gradient, causing the field strength to decrease rapidly into the tube. Up to a point, the steeper the field gradient the higher the magnification, but a maximum is reached at a level dependent on the general form of the whole field shape. Considering the higher level attained in the parabolic and cubic forms as compared with the linear form, it appears that a positive second derivative is advantageous, causing the curve to flatten out, as in Figures 3.7 and 3.9. In this way a steeper gradient can be attained at the cathode, without the curve heading straight down to zero so that the field reverses direction in close proximity to the cathode. The poor imaging associated with conditions to the left of the peaks in the various magnification curves is attributed to field reversal too close to the cathode. In the more favorable cases encountered the field strength approaches zero in the vicinity of about 5 cm from the cathode and remains at low levels, positive or negative, in the central region of the tube. Towards the target the field shape is less influential on M, but can be important in determining other properties.

3.5 Preliminary Power Estimate - Effect of Iron

At an early stage in the project steps were taken to get some appreciation of the coil power levels associated with the magnetic field distributions being considered in the study of algebraically defined B-field distributions. The case chosen for this purpose was the cubic form characterized by parameter values $b_1 = -.75$, $b_c' = b_1' = -.35\ \mathrm{cm}^{-1}$ (see Figure 3.9) which provides M = 3. At 8 KV operating voltage the field strength for this case is $B_c = 154$ gauss. In order to achieve this, and the steep field gradient $B_c' = -\ 54$ gauss/cm, it is necessary to position the photocathode between a closely spaced pair of strongly opposing coils -- what can be loosely termed a "dipole" arrangement. The roughly antisymmetric field condition at the other end similarly requires a second such dipole straddling the target. The arrangement is shown schematically in Figure 3.10. With this basic concept a series of optimization computations was conducted using the Patternsearch technique (PAT for short) coupled with a subroutine for calculating the axial field distribution due to a specified solenoid system in the absence of iron (i.e. ferromagnetic material). The latter routine is essentially that mentioned in Section 3.2(c). An outline of this application of PAT is given in Appendix 2. Variables in this study were coil dimensions, positions, and strengths (current density), although not all were varied in a single computation. Constraints were imposed to maintain the 4 main characteristics of the desired field configuration, namely the field strengths and gradients at cathode and target. Additional constraints were used to restrict the coils to reasonable dimensions and prevent them overlapping the tube space.

To reduce power consumption large coils are obviously advantageous since for a given total ampere-turns the resistance is inversely proportional to cross-sectional area, and hence so also is the power. When the current is spread too far from the active field region, however, the return diminishes and is paid for in excessive bulk. The main requirement appears to be to fill the available space with copper as close to the regions of high field strength as possible. Gaps between the opposing coil segments in Figure 3.10, for example, do not appear to be beneficial. From the many computer runs made, the smallest power figure obtained for this field configuration was 151 watts, which involved a coil system of 20 cm outside diameter and 20 cm length. This is a very high power level compared with the 5 watts necessary to operate the image section alone in the normal mode, or the 15 watts necessary to run the whole camera tube coil system. Furthermore it is an "ideal" figure based on the use of solid copper rings rather than wire-wound coils. The figure for real coils would be 25% to as much as 100% higher, depending on design details.

Given the restriction on internal diameter imposed by the WX32193 image section, it is unlikely that this power requirement can be reduced significantly by further effort along the lines described above. Therefore the question arises as to the extent to which the use of iron in the system, to concentrate the field strength at the two ends, might improve the efficiency. The problem of magnetic field distribution in the presence of iron is more difficult than that without iron, being similar in principle to the electrostatic field problem posed by a system of conducting electrodes. It can also be solved by the same relaxation technique, and the computer program used in this project for the E-field solution (Section 3.1) is provided with an input option for application to the magnetic problem. The computation of a single case is sufficiently expensive that it was not appropriate at this stage to incorporate it into our optimization schemes, although there is no reason in principle why it could not be. Such an approach may be appropriate in later consideration of a final coil design for an LST camera. What was wanted at this point was simply an indication of the possible effectiveness of iron.

The sample geometry shown in Figure 3.11 was designed, based on the concept of Figure 3.10. The coil system is shrouded by iron to reduce spreading of the field, and so increase efficiency within the system. In addition, the four coils are separated by iron disks, the idea being to increase isolation of the individual coil contributions and prevent them fighting each other to the extent they do in the unshielded case.

This system is simply a computer model designed to test a concept, and is not proposed as a practical system, the evolution of which would require a longer and more detailed study. Superimposed on Figure 3.11 is the relaxation net used in the computation. This is coarse, 1 mesh/cm, since high accuracy was not considered important. The thickness of iron was chosen for computational convenience and may not relate to practical requirements. It is assumed that no saturation occurs -- in a practical development choice of the material and its thickness would attempt to justify this. A value of 100 was chosen arbitrarily for the permeability of iron.

This fixed geometry has four free parameters, the coil current densities, J_1, J_2, J_3, J_4, and the problem is to select these so as to satisfy the 4 field conditions imposed by choice of the field strengths and gradients at cathode and target. To solve this problem it is necessary in principle to have four independent solutions of the field problem, corresponding to the four independent parameters J_i. Let $B\ (J_1,J_2,J_3,J_4)$ be a general solution of the magnetic field problem, i.e. the solution corresponding to coil strengths $J_1 \ldots J_4$, then define 4 basis solutions as

$$B_1 = B(1,0,0,0)$$

$$B_2 = B(0,1,0,0) \text{ etc.}$$

If the assumption of no saturation is valid, the principle of superposition holds, so that

$$B\ (J_1,J_2,J_3,J_4) = \sum_{i=1}^{4} J_i B_i$$

i.e. the solution corresponding to any set of coil strengths can be constructed from the four basis solutions. Imposing the four field constraints on B we develop from this 4 simultaneous linear equations which can be solved for the strengths J_i. For convenience the target is placed at $z = 32$ (a slight change in cathode-target distance from 11.8 to 12 cm) to make the geometry symmetrical about the center plane $z = 26$. This reduces the required number of basis solutions to 2. The results obtained for the coil current densities and power corresponding to $B_c = 154$ gauss were as follows:

coil	1	2	3	4	
amp/cm^2	121	-43.1	55.1	-109	
watts	22.0	2.5	4.1	17.8	46 Total

For comparison, the same set of four coils with the iron removed requires the following:

Coil	1	2	3	4	
amp/cm^2	223	-147	161	-208	
watts	74.9	28.9	34.5	64.7	203 Total

The effect of the iron is very appreciable. The power reduction for this particular coil geometry is a factor of 4, and there is a factor of more than 3 improvement over the optimized coil geometry previously quoted (151 watts). This improvement might be further enhanced by optimization of the shrouded coil system. These results give grounds for optimism that careful design with the use of iron can yield considerable reduction in coil power, and consequently even some of the more exotic field shapes suggested by this study might warrant further consideration.

The field distribution on the axis of the shielded coil system is shown in Figure 3.12 in comparison with the cubic form from which the design developed. The two curves have the same values and slopes at cathode and target, but show considerable disparity elsewhere. The new curve maintains steepness to a greater distance from the cathode before flattening off to a very low field level over the middle region of the tube. In view of the conclusions drawn from the algebraic study (Section 3.4.4) these properties might be expected to result in higher magnification. Ray tracing shows this to be the case, the computed value being 3.78. Correspondingly, for the fixed 8 KV operating voltage the new field shaping requires higher focus field strength with $B_c = 171$ gauss. The calculated coil power requirement increases as the square of the field-strength, and so rises from 46 to 57 watts. In view of the possible importance of this system as a basis for future practical development, the computed imaging properties are presented fully in Figure 3.13. The resolution uniformity is not as good as that obtained from the original cubic field form, but is still good, holding up to 40 line-pairs/mm in the corner. Radial distortion is only about 2% and the total rotational error $\Delta\phi$ rises to about 2.5 degrees. All of these properties would be rated as very good by the generally accepted standards of the camera tube field, where the imperfections of the reading section usually dominate the overall imaging performance.

3.6 Power V. Magnification Optimization - Image Tube Test Study

In the preceding section detailed predictions have been made regarding a high magnification system that could conceivably be developed into a practical system for the LST camera. Those predictions, however, could not be practically tested within the scope of this contract, where it was necessary to restrict attention to rather simple coil systems that could be quickly designed, built, and modified if necessary. In this section the emphasis is directed more towards consideration of operating conditions that could be readily tested in the laboratory. At the start of the project it was not known whether or not high magnification, $M \geq 3$, was possible in the WX32193, with its large area (70 mm output diameter) image section. Prime importance was therefore attached to demonstrating high magnification, with secondary regard being given to considerations of its suitability for the LST application. Problems associated with the LST would become defined in the course of the experimentation. In addition to demonstrating a system with high magnification, it was considered important to determine the level of trust to be placed in the predictions of the computer programs. For then, the probability of achieving success with more advanced systems, such as described in Section 3.5, could be assessed.

The computational search for suitable test cases was conducted on the basis of getting the highest possible magnification within the capability of the test equipment at hand. Little attention was paid to image quality, beyond the requirement for filling the whole output field. The early work, as described in the preceding section, soon indicated that the main limitation was power -- not so much what could be generated as what could reasonably be dissipated close to the image tube. One measure adopted to ease this problem was the choice of a lower operating voltage of 6 KV, which is standard for the results described in this section. A sequence of optimization computations was conducted in an attempt to quantify the magnification/power trade-off in relation to the test coil system built, which is shown in Figure 3.14. Each of the coils numbered 1 through 4 is made up of two of the basic 1" long coil segments connected in series. Coil #5 slides inside the cylinder on which the other coils are mounted, and sits close to the front of the image tube. The gap between coils #2 and 3 is to accommodate the getter appendage, which was left attached to the later tubes built. The cathode-target distance shown is that used as standard for most of the computer work, and on which all results in this section are based. In practice this dimension was modified to the value 12.8 cm in image intensifier #3, on which the most important experimental work was done.

3.6.1 Optimization problem #1

The computational problem of minimizing power for a given magnification was not approached directly because it was not considered economic to link the ray tracing computation to the optimization routine, although that would be possible. Instead, the optimization goals were expressed in terms of the magnetic field properties that had already been found to be important in determining magnification. Thus, the first optimization problem considered was that of achieving given values of B_c and B_c' with the minimum power to the 5 coils. The problem can be summarized as follows -

Optimization #1

Number of system variables - 5 (coil strengths)
Equality constraints - 2 (B_c and B_c')
Number of degrees of freedom - 3
Inequality constraints - current limits on the coils

B_c and B_c' were specified separately to the computer program although it is really the ratio that is important (the problem could be alternatively stated in terms of 4 variables, the coil strength ratios, and one equality constraint B_c'/B_c). The number of degrees of freedom is simply the difference between the variables and the equality constraints, and represents the dimensionality of the search space of the optimization routine. The inequality constraints place a limit on the current carrying capacity of the individual coils, in effect putting a boundary around the search space. Some further details of the technique used to solve this type of problem with the Patternsearch routine are given in Appendix 2. To solve a simple case, we fix the field strength at the cathode $\bar{B}_c$ arbitrarily and choose the gradient $\bar{B}'_c$. The optimization program (OPTIM) minimizes the power and outputs the resulting coil strengths, and the power value $\bar{W}$. We then input those coil strengths to the ray tracing program which, for the field distribution shape so defined, evaluates the required focus field strength B_c, and the electron optical properties. Since B_c is not equal to the arbitrary value $\bar{B}_c$ given to OPTIM, the power value corresponding to this case is then obtained by scaling,

$$W = \bar{W}\ (B_c/\bar{B}_c)^2$$

The results obtained for a range of values of the parameter $b'_c = B'_c/B_c$ are summarized in Figure 3.15 where (a) shows the variation of magnification M, focus field B_c and power W, and (b) shows the variation of the distortion parameters D and S. The results display features familiar from the algebraic study in Section 3.4, in that the distortions change rapidly as the field gradient steepens beyond the point of maximum magnification. The peak M exceeds 3.2 and is attained with a surprise-ingly low power of about 20 watts. This is for 6 KV operation -- for other voltages V_T, the B_c for focus scales as $V_T^{1/2}$ and hence the coil power directly as V_T. In the region $b'_c = -.25$ we have high magnification together with reasonably low distortion levels. Figure 3.16 shows the coil strengths J_i in amp/cm^2. As expected, coils 1 and 5 act positively to set up the high B_c value and are opposed by coils 2, 3 and 4 which enforce the steep gradient B_c'. Coil 5 is by far the most heavily loaded and, at the steepest gradient value, becomes limited by the constraint imposed on the optimization program. Hence, in this region the load begins to be taken by coil 1, the current density curve for which takes an upturn. The load on coils 1 and 5 could be more evenly shared by reducing the constraint value -- this would result in increased total power, but reduced power in coil 5, which might be advantageous. However, the gain would not be very great because #5 is much more efficient then #1 by virtue of its closeness to the photocathode, so that a small reduction in J_5 requires a large increase in J_1 to compensate.

Representative field shapes for stated values of b_c' are shown in Figure 3.17 and are seen to resemble the parabolic curves in Figure 3.7. These shapes are essentially a practical realization of that parabolic form, and the imaging properties they produce resemble strongly those presented in Figure 3.6. Note also that with b_c' values to the left of the magnification peak field reversal occurs in the vicinity of $z = 4$ cm which, we conjecture, is detrimental (see Section 3.4.2).

3.6.2 Optimization problem #2

This last observation suggests a further investigation into the properties of field distributions with $b_c' < -.25$ cm^{-1} when the field reversal point is prevented from approaching too close to the cathode. This is the objective of optimization problem #2, which is simply problem #1 with an additional constraint - specification of the coordinate value z_o at which field reversal occurs. This reduces the number of degrees of freedom to 2. In order to attain higher magnification values than in problem #1, the fixed value $b_c' = -.3 \text{ cm}^{-1}$ was chosen. The independent variable for the sequence is z_o, which was varied positively from the value 3.8 cm "natural" to the chosen field gradient according to Figure 3.17. Figures 3.18, 19, and 20 show results in a form similar to the preceding 3 figures. As z_o increases, magnification increases to a peak value of over 3.6, with a calculated power of 35 watts. Figure 3.19 shows that to do this it is necessary to increase the negative current in coil 2, which alone holds the gradient value, while coils 3 and 4 are driven positive to establish the z_o value. Throughout the range the constraint on J_5 is active (213 amp/cm^2) and J_1 varies only slightly. The focus field strength for 6 KV operation was found to be 138 gauss, almost independent of z_o in this range. From the field shapes in Figure 3.20 it is seen that at $z_o = 5.6$ cm the field curve touches zero without crossing. Consequently if z_o is set at higher values, the optimization routine locks onto the second field reversal instead of the first, and the same set of results would be generated in reverse order. Figures 3.18 and 3.19 should be symmetrical about that plane.

3.6.3 Some further examples

All these results support earlier conclusions that the magnification can be increased by progressively steepening the field gradient at the photocathode, provided field reversal is not allowed to occur too close to the cathode. Attempts were made to push this concept further. Figure 3.21 shows field shapes relating to some of these, having $b_c' = -.33 \text{ cm}^{-1}$, each case having different additional constraints imposed to control field reversal position z_o. The most important properties of these cases are listed in the following table.

$b'_c = -.33\ \text{cm}^{-1}$, $V_T = 6$ KV, $z_T = 11.8$ cm

Curve	M	W (watts)	D%	S (rad. cm^{-2})	res.	Constraints
1	3.50	63	-6.27	-.0034	23/15	$z_o = 5$
2	3.73	76	-4.73	-.0023	24/17	$z_o = 5$, $J_4 = -60$
3	3.77	89	-3.70	-.0011	25/18	$z_o = 5$, $J_4 = -100$
4	3.60	251	+1.71	+.0026	26/26	$b_T = -.7, b'_T = -.33$

The constraints on the optimization program are as defined in the last column. The first 3 curves have $z_o = 5$ cm, with curves 2 and 3 having in addition fixed values for J_4 of -60 and -100 amps/cm^2, respectively. In curve 4 the z_o constraint is removed and instead the parameters b_T and b'_T are set, these being the values of parameters b_1, b'_1 at the target position z_T, i.e. $b_T = B_T/B_c$, $b'_T = B'_T/B_c$. The resolution values given are for the corner of the image field ($r_{out} = 3.5$ cm). Curves 2 and 3 produce greater magnification than was obtained with optimization problems #1 and 2, but only at a disproportionate cost in power. The reason for curve 4 was mainly to connect this group of results with those for the cubic form (Section 3.4.3) and for the shielded coil design of Section 3.5. In particular it was of interest to check if the rather high corner resolution noted for the latter cases (e.g. see Figure 3.13) would be reproduced, but that does not appear to be the case.

3.6.4 Conclusions

It appears that the conditions covered in optimization problem #2 represent something of an optimum region in the magnification/power trade-off for our system. The reason can be seen by reference to Figure 3.19. The gradient constraint $b_c' = -.3$ acting alone results in $z_o = 3.8$ cm. To constrain z_o to about 5 cm it is only necessary to reverse coil currents 3 and 4, and drive J_2 correspondingly more negative. At steeper gradients, however, the conflict between J_2, tending to reduce z_o, and J_3 trying to hold it, becomes more severe. In addition, J_4 must begin to oppose J_3 in order to hold down the field strength near the target, as suggested by the results of Figure 3.21. This leads to a natural trend towards the "two-dipole" form discussed at the outset of Section 3.5, with consequent steepening of the power v. M curve. Therefore, the appropriate cases for demonstration purposes are chosen from the set described in Section 3.6.2. In particular, the case defined by $b_c' = -.3$, $z_o = 5$ cm, is singled out as having good overall imaging properties. This is discussed further in Section 4.4 in connection with the experimental work. See also Section 3.8 where this case is considered in conjunction with a non-uniform E-field distribution.

3.7 Camera Tube Test Study

In considering suitable test cases for demonstration of the camera tube use was made of some of the concepts developed in connection with the image intensifier study described in the previous section. It was only necessary to adapt those ideas to a different coil system, and to take into account additional constraints on field shaping arising from the needs of the reading section. The arrangement of coils in relation to the tube is shown in Figure 3.22. It is similar in principle to the image tube system of Figure 3.14, but the detailed dimensions are different. Coils 3, 4 and 5 were constant throughout the testing, but the physical coils used in positions numbered 1, 2 and 2A were changed from one test to the next. The geometries shown in the figure pertain to the final system. In practice coils 2 and 2A are connected in series. Coil 2A was ignored in some of the computations because it differs from #2 in thickness, and is relatively weak. Coil #4 is the focusing coil for the reading section of the tube, and this represents the main point of difference as compared with the image intensifier test study. If the camera tube is operated in continuous read/write mode the B-field distribution in the image section must be shaped so that it blends smoothly through the target region with the roughly uniform field required in the reading section. If the tube is operated in sequential read/write mode, as it will be in the LST application, then this restriction does not necessarily apply, as the reading section coils may be switched off during the writing period. We decided to test in the continuous mode (see Section 5), and to solve the field matching problem by arranging the reading section focus coil #4 to overlap the image section side of the target. The amount of overlap shown in Figure 3.22 is about 1 cm in the case of the original design dimension for photocathode-target spacing shown there.

In selecting coil currents for magnification, the current in coil 4 was held fixed at the value required by the reading section. This implies one less degree of freedom in the optimization processes used. Having fixed the magnitude of J_4, however, there still remains open the choice of its sign. The magnetic field in the reading section may have either the same direction as that at the photocathode (positive), or the opposite direction, just as in the preceding section both positive and negative field strengths at the target were considered (see Figure 3.17, 20 and 21). A sequence of optimization computations was carried out, similar to those described in Sections 3.6.1 and 3.6.2. The problem posed in this case is optimization problem #2 with an additional constraint added by fixing the value of J_4. Thus, we choose values for the gradient b_c', the field reversal point z_o, and J_4, and the program evaluates the other coil strengths J_1, J_2, J_3 and J_5 to minimize the total power W. In view of the knowledge already gained the value of z_o was set at 5 cm. For the two cases $J_4 = \pm 40$ amp/cm^2, which correspond to the nominal reading-section focus field of 80 gauss, b_c' was varied over the range - .26 to -.3 cm^{-1}. The power variation results are shown in Figure 3.23(a). The curves for the 2 values of J_4 cross at about $b_c' = -.27$. For shallow field gradients, i.e. lower magnification, the negative J_4 provides the lower power, but at the steeper gradients positive J_4 becomes advantageous. These curves are not adjusted for focus field strength in the manner described in Section 3.6.1, because all the imaging computations were not completed, but assume a fixed value $B_c = 135$ gauss. Such adjustment would modify the details but not the main features of the curves. Figure 3.23(b) shows the variation of field strength at the target, which will influence uniformity of field in the reading section. Negative J_4 appears to be advantageous in that respect throughout the gradient range, and was therefore the condition chosen for the camera tube testing. Figure 3.24 shows the different field shapes resulting from positive and negative J_4 in the case $b_c' = - .28$. These fields provide magnification values of 3.37 for $J_4 = + 40$ and 3.30 for $J_4 = -40$. The greater steepness of field in the target region in the positive J_4 case is evident.

3.8 Non-Uniform E-field

All the work described under Section 3 up to this point has made use of a single electrostatic field distribution, namely that defined by the model and electrode potentials shown in Figure 3.1, which for all practical purposes represents a perfectly uniform field. As there is no a-priori reason to assume that E-field shape to be optimum for purposes other than unit magnification, it seemed appropriate to give some consideration to the properties of some other configurations. Attention was restricted to mildly non-uniform E-fields because it is considered that strong non-uniformity must involve strong variation of conditions across the photocathode, which is likely to be detrimental to image uniformity. The electrode potentials in Figure 3.1 for the standard field solution are set on a linear relationship to z, the distance of the electrode from the cathode. The simplest departure from that was to introduce a second-degree term into the relationship, the coefficient of which can be varied to alter the degree of non-uniformity. A single choice of the coefficient defines all the electrode voltages on a smoothly rising curve from cathode to target, and these in turn ensure a smooth E-field solution from the relaxation program. A series of computations was performed for various voltage curves. in conjunction with the cubic form B-field distribution, with $b_1' = -.35$ shown in Figure 3.9 (this was considered to be the most interesting case at the time this series was done). This B-field with the standard uniform E-field gave a magnification of 3.0.

The results obtained for M, B_c, and D are shown in Figure 3.25 plotted against E_c/E_u, the ratio of the E-field strength at the cathode to that in the uniform E-field condition. It is seen that an increase in E_c provides an increase in magnification and requires an accompanying increase in magnetic field strength to focus. This may be advantageous at relatively high magnification in view of the results of Section 3.6.3, where the power v M curve was found to steepen rapidly beyond a certain point. A variation of E_c may be able to increase M beyond that point relatively economically. Figure 3.25(a) shows that the distortion increases positively with E_c, giving rather large values in this instance. However, applied to a B-field shape with low or negative distortion this trend might be acceptable. The S-distortion and corner resolution were found to be constant over the range of E_c considered here, the values being .0045 rad/cm^2 and 70 lp/mm. Figure 3.25(c) shows electrode-voltage curves for the two extreme cases considered, which correspond to values E_c/E_u = .775 and 1.23. These are plotted in the form of fraction of total voltage vs. fraction of tube length, and the positions of the plotted points correspond to the electrode positions in the model of Figure 3.1.

In view of the possible advantage of strengthening E_c suggested above, the E-field condition represented by E_c/E_u = 1.23 was tried in conjunction with the B-field shapes of the shielded coil design Figure 3.12, and curve (b) of Figure 3.20. Results for these are shown in Figure 3.26 (a) and (b) respectively. The first of these can be compared directly with Figure 3.13 which shows the corresponding case with uniform

E-field. The magnification is increased from 3.78 to 4.08 with an increase in power from 57 watts to 70 watts (8 KV operation). Apart from a small increase in distortion, image quality is largely unchanged. In Figure 3.26 (b) a magnification of 3.99 is achieved with only 41 watts (6 KV operation), which can be compared with M = 3.6 and 35 watts for the corresponding uniform E-field case in Figure 3.18 (a) (z_o = 5 cm). The distortion, slightly negative in the original, has become slightly positive, and the imaging properties appear good overall. The non-uniform E-field has produced a significant magnification increase for a modest increase in power, which contrasts strongly with results of Section 3.6.3, where attempts to increase M beyond 3.6 by steepening the B_c' involved disproportinate power increases. It is concluded that increasing E_c is advantageous for minimizing the power requirements for magnification values in the region of 4.

4. IMAGE INTENSIFIER TESTING

4.1 Experimental Equipment and Techniques

Figure 4.1 shows a schematic of the image intensifier test arrangement, consisting basically of a symmetrical optical system with the tube under test at the middle. The object of the system is a 25 μm wide slit for the MTF measurements, or a USAF 1951 test pattern for the visual resolution readings. This is demagnified by a factor of 20 onto the photocathode by the input lens. The image produced at the phosphor target of the tube is correspondingly magnified by a factor of 20 by the output lens, directly onto the photographic film, there being no separate lens in the camera. The magnification values were accurately set up and the correct component positions recorded for convenient resetting. Each of the lenses is a 50 mm El-Nikkor lens set at f4 aperture. To suit these, the light spectrum is restricted to a band at 520 nm wavelength by use of the green filter between lamp and test object. Under these conditions the lenses provide near diffraction-limited resolution. A calibration measurement of their capability is described below. In addition to the green filter, a slot is provided in front of the lamp for a neutral density filter, which is necessary to the technique used to derive the line-spread functions for the MTF measurements. For the visual resolution readings the output optics and camera are replaced by an 80-power microscope of virtually perfect resolution over the range of interest to us (i.e. MTF > 90% at 80 line-pairs/mm).

A schematic of the tube located in the coil system has been given in Figure 3.14. Photographic views of this from the side, input end, and output end respectively, are shown in Figures 4.2, 3 and 4. The tube in position is image tube (IT) #3, and the getter appendage can be seen protruding through the center gap in the coils. In the early part of the experimentation, with IT #1, there was no appendage, and the 8 coils were closely packed. Figure 4.2 shows the viewing microscope in position. Beneath the coil assembly is a set of resistors and a multi-position switch for monitoring up to 5 separate coil currents. The table supporting the coil assembly and tube can be moved laterally by the calibrated crank at the bottom, which facilitates off-axis observations . In Figure 4.3 the input optics can be seen in position close to the photocathode, and coil #5 is visible inside the plexiglass cylinder. This is a push fit in the cylinder and rests against the front end of the tube separated only by a plastic insulating ring. The tube is centered in the cylinder by means of sponge rubber spacers at 6 points and the resulting concentricity and alignment of the system is very good. Two of the spacers can be seen in Figure 4.4 with the high-voltage cables to the tube electrodes passing around them. The resistor chain supplying the voltages is mounted on a panel attached to the side of the assembly opposite to the coil terminals. Each resistance in the chain is 30 Mohm, made up by 2 parallel-connected 60 Mohm resistors. When supplied with a total of 8 KV the 8 voltage steps down the chain were measured to be in the range 985 to 1040.

Coil Data - The 8 coil segments visible in Figure 4.2 are nominally identical. They are connected in series - pairs to make the 4 coils numbered 1 through 4 in Figure 3.14. The following table summarizes their properties:

		Coils 1 through 4	Coil 5
internal dia.	(inch)	5.0	3.28
external dia.	(inch)	7.0	4.70
length	(inch)	2.06	1.50
X-section	(cm^2)	13.3	6.86
Wire	(AWG)	21	22
turns		1912	1134
turns/cm^2		143.5	165.4
resistance	(ohms)	40	20

Optics Calibration - In order to obtain an MTF curve for the optical system, with which to correct subsequent measurements made on the tubes, the arrangement shown in Figure 4.2 was set up without the tube in. In its place we put 2 glass plates in close contact, simulating the effects of the tube windows. The 2 halves of the optical system were closed together so that the image formed by the input system was located at the common plane of the plates, and was in turn imaged by the output system onto the photographic film. This should provide a good measure of the optics performance under actual operating conditions. A possible improvement in this respect might be to make the second glass plate a diffuser, so that the object to the output lens would have an angular emission distribution similar to that seen when viewing the phosphor. However, because of the symmetry of the system, with both lenses set at f4, the output cone from the input lens fills the input cone to the output lens, and so the use of a diffuser was not considered vital. Figure 4.5 shows (a) the resulting line-spread function (LSF) derived from the densitometer readings and (b) the sine-wave MTF curve obtained from it. The slit image has a width of 3 μ m at the half-height point. The MTF curve shows a response of 40% at 80 cycles/mm and limiting resolution capability well beyond 250 cycles/mm.

<u>MTF Measuring Technique</u> - The 25 μ m object slit is reduced by the input optics to 1.25 μ m at the photocathode. The final image produced by the system, remagnified by a factor of 20, is viewed on the ground-glass screen of the camera for focusing purposes. A sequence of 8-separate photographs is then taken using different neutral density filters between the lamp and slit, such that the density advances by 0.2 at each step, there being no other intentional differences between exposures. The photographs are developed and scanned in the microdensitometer (Jarrell-Ash 23-100) providing 8 separate line-spread profiles in density form. Each 0.2 increase in density between exposures is equivalent to reducing intensity by a factor 0.63. Thus, the peaks of successive LS profiles provide intensity values for 8 points on the density scale of the microdensitometer charts, which calibrate the response of the film. The first of these intensity values (peak of the first profile) is arbitrarily assigned the value 1.0, and the following peaks then take values 0.63, 0.63^2, 0.63^3 etc. down to the intensity level $0.63^7 = 0.04$. The line-spread profile widths are read at these points and the corresponding values from different charts are averaged to produce the final LS profile in intensity form, such as is shown in Figure 4.5(a). Readings are taken from

this curve at equal spatial intervals and fed as input data to the Fourier-Transform computer program which outputs the corresponding sine wave MTF values over the desired frequency range. An outline of that program is given in Appendix 3. Initially we employed Kodak Tri-X film for the slit photographs, which was satisfactory for the optics calibration. When the image tube was introduced, however, the available light was inadequate and the exposure times increased to 2 minutes. We subsequently switched to Kodak 2475 with which an exposure of about 30 seconds was needed.

4.2 Image Tube #1 - Standard Mode Test

We first conducted a series of experiments on IT #1 operating in standard mode, with the objective of establishing a reference level of performance against which to judge later results. "Standard mode" means at nominally unit magnification, and normally involves equal currents in all coil segments connected in series (except coil #5 which is inoperative). IT #1 was constructed to the original design, with a cathode-target dimension of 11.75 cm. The getter appendage was tipped off before delivery and so the need for the center gap in the coil system, shown in Figure 3.14, had not arisen at that point. Figure 4.6 shows the location of the tube in the coil system and the shape of the magnetic field distribution from cathode to target. The overall length of the coil assembly is 21.2 cm, so that the turns density averaged over the total area, including the small spacing between segments, works out to 142 turns/cm^2. The tube is positioned asymmetrically with respect to the center plane of the coils. This is because of physical limitations imposed by the viewing microscope, which sticks into the end of the system close to the output window. The result is better uniformity of field at the photocathode than would obtain in the symmetrical position, which is beneficial to image uniformity.

Magnetic Field Mesurement - Figure 4.7 shows a comparison of the computed field shape (solid curve) with that obtained experimentally. Only one-half of the symmetrical curve is drawn, and the locations of the photocathode and target are both shown (the target of course is actually in the half not drawn). The measurements were made with a Bell 120 gaussmeter, with no tube in the system, and corresponding points on each side of the center plane were averaged to obtain the plotted values (discrepancies between corresponding values were less than 1% of maximum reading). Agreement with the computed shape is good, but there appears to be a small systematic discrepancy making the empirical curve slightly flatter. No comparison was made as to the absolute value of the field strength as the gaussmeter was not reliably calibrated. The strength of the coils according to computation is 344 gauss/amp at the cathode position (367 gauss/amp at the coil center), which appears to be essentially verified by the following focus agreement.

Focusing Conditions - For 8 KV operation the ray tracing computation shows the focusing field strength to be $B_c = 77.0$ gauss which, from the coil strength quoted above, requires $I_c = .224$ amp. The focus conditions set up experimentally were $I_c = .222$ amp at 8.05 KV, which is in satisfactory agreement with computation. The total resistance of the 8 coil segments in series is 160 Ω so that the operating power in the normal mode is

8.0 watts (c.f. the ideallized figure of 5 watts quoted in Section 3.5, calculated from the "solid copper" model).

Visual Resolution Measurement - Observations of limiting resolution under the above conditions were made at image center and at .5 cm intervals to left and right to a radius of 3.5 cm. Corresponding movement in the vertical direction was not attempted as the apparatus does not permit this conveniently. Differences between corresponding positions on the two sides of center were not more than 1 element on the test pattern (12% of the reading) which is within the experimental error typical of this kind of measurement. Astigmatic differences at any point were within the same limit and so are ignored. The figures for the 2 sides were averaged to produce the empirical curve presented in Figure 4.8, showing 80 line-pairs/mm at center, falling smoothly to 40 at the edge (2.5 cm radius) and 24 in the extreme corner (3.5 cm radius). For comparison, the broken curve shows the limiting resolution for the electron optics alone as estimated by the ray tracing computer program. The tube is essentially phosphor limited at the center, as would be expected. The phosphor batch from which this tube was supplied was checked at 153 line-pairs/mm when deposited. This, however, is a measurement made with UV excitation prior to deposit of the aluminum backing layer, and it is normally considered to overestimate the final phosphor capability by an appreciable amount.

In the marginal region the tube is electron-optically limited, and the computer estimate is at about the right level. It can be noted that both the estimated and actual off-axis performance here are appreciably better than that estimated for the Penntran coil (Figure 3.3).

Further observations were made on the variation of focus current and limiting center resolution (when focused) with operating voltage. These results are shown in Figure 4.9. Taking the coil current reading of 224 mA at 8 KV as a reference point, the focus current should follow the solid curve shown, since B-field strength varies as $V^{1/2}$ for constant focal length. Departure of observation from this at the low end is attributable to poor visibility of the image, making the true focus point hard to detect. Resolution variation is more complicated, being compounded of the constant contribution of the optics, the contribution of the phosphor which for practical purposes can be assumed to be independent of electron energy, and the electron optical chromatic aberration disk which theoretically varies directly as the voltage. The flattening of the curve at the upper end is consistent with the assertion of phosphor limitation.

MTF Measurements (focused condition) - In the paraxial focus condition at 8 KV, line spread photographs were taken at center and, with the slit in the tangential direction, at the edge of the field (2.5 cm radius). The resulting MTF curves, corrected for the degradation due to the optical system, are shown in Figure 4.10. The visual limiting resolution observations for these two positions were 80 (center) and 38 line-pairs/mm. The MTF curves fall to the 4% respons[illegible]vel at 66 and 22 cycles/mm. Note that these are sine-wave MTF curves and so will under-estimate the square-wave response which is more pertinent to comparison with the visual limitation measurements. At the 20 cycle/mm point the center curve shows 61% response. This is equal to the goal set for the MTF curve of the complete WX32193 camera tube. If the MTF curves presented here are truly representative of the image tube performance, then the implication is that the [illegible] reading section of the camera tube must together have an MTF as good as the output phosphor of our intensifier. [illegible] for the [illegible] is not directly obtainable, but estimates can be made from measurements at ⓦ Tube Division on the same type of phosphor.(4) Figure 4.11 shows a measured square-wave MTF curve for a phosphor whose limiting resolution figure measured with UV excitation, was 171 line-pairs/mm. This curve was measured under conditions corresponding to image tube use, i.e. with electron-beam excitation, through aluminum backing, and was found to be approximately independent of operating voltage in the range 8 to 14 KV. The estimated curve shown for our phosphor, whose UV resolution figure was 153 line-pairs/mm, is obtained from the measured curve by scaling the horizontal coordinate in the ratio 153/171. This curve appears to be rather high in comparison with curve (a) in Figure 4.10, even after making allowance for the difference between square wave and sine-wave response. The high estimated electron optical limit of 170 line-pairs/mm, together with the observed limit of 80 LP/mm (Figure 4.8), would lead us to suspect a phosphor limitation of about 90 LP/mm which does not look consistent with the MTF curve just deduced. This suggests that either the electron optics capability has been over-estimated or else that our resolution observations are degraded by some factor not accounted for. More evidence relating to the electron optics estimates is discussed in later sections. The most likely sources of degradation in our experiments are (a) mechanical vibration and (b) power supply instability. The first of these is a problem that we have not been able to completely overcome or to quantify. The photographing of the line spread images involves exposures of 30 seconds, and so the results incorporate degradation due to any vibrations occurring in that period, which is a completely unpredictable factor. As the image cannot be observed during exposure, the photographs must be taken on trust. On the other hand, the MTF curves obtained are not strongly inconsistent with the visual resolution readings, which are probably much less likely to be affected by vibration. When observing the test pattern through the microscope it is possible to "look through" the vibration in order to get a true reading. In view of this, and the very high MTF curve obtained for the optics (Figure 4.5), we think the vibration factor is generally not a serious problem, although the possibility exists of some particular curve being unduly degraded. The question of power supply instability is covered by the next experiment described.

incorporate degradation due to any vibrations occurring in that period, which is a completely unpredictable factor. As the image cannot be observed during exposure, the photographs must be taken on trust. On the other hand, the MTF curves obtained are not strongly inconsistent with the visual resolution readings, which are probably much less likely to be affected by vibration. When observing the test pattern through the microscope it is possible to "look through" the vibration in order to get a true reading. In view of this, and the very high MTF curve obtained for the optics (Figure 4.5), we think the vibration factor is generally not a serious problem, although the possibility exists of some particular curve being unduly degraded. The question of power supply instability is covered by the next experiment described.

Resolution vs Coil Current - In order to quantify the sensitivity of resolution performance to power supply stability, observations were made with deliberate departures from the 8 KV focused condition. Figure 4.12(a) shows the visual limiting resolution as a function of coil current with the tube voltage held at 8 KV. Readings were made at intervals of 1 mA on the low side of the established focus current I_c = 222 mA, it being assumed that the curve would follow a symmetrical path on the high side. The 1 mA step represents the limit of our practical system both for current setting capability and measuring capability. A change in resolution was visible immediately at the first step and was recorded as the loss of one element of the test pattern. In looking at this kind of data it should be remembered that the 12% resolution jump between adjacent elements of the AF test pattern limits the accuracy of observation of small resolution changes. Figure 4.12(b) shows MTF curves corresponding to 3 values of coil current, namely the focus value 222 mA, and 1 mA on either side of that. The closeness of the 221 mA and 222 mA curves suggests that this is essentially a range of good focus. It seems likely that the operating voltage in this experiment was set slightly different from that in the limiting resolution observation. The curve for 223 mA shows a considerable loss. We conclude that the depth of focus for this image intensifier in terms of coil current is ± .5 mA which is about 0.25%. Within this range the response of 60% at 20 l.p./mm is maintained. Because the focal length of the tube is proportional to $V^{1/2}/B$, it follows that the tolerance on the high voltage supply is twice that on the coil current, i.e. ± 0.5% which means ± 40 volts at 8 KV operation. The ripple levels on our power supplies were measured under operating conditions to be 0.1 mA on the coil current and 15 volts on the high voltage, both peak-to-peak values. These are well within the tolerances deduced here and so we do not consider ripple content to be of any significance in our resolution measurements. More of a problem was posed by long term variation of the coil current, despite the fact that the supplies involved were supposedly current regulated. Changes of 1 mA on the monitoring meter were frequently observable in the course of operating the system for periods of about 1 hour, necessitating constant attention and resetting while recording data. This problem is probably due to temperature changes in the power supplies.

<u>Other Properties</u> - The computer analysis of this tube in the standard mode showed the paraxial magnification to be 0.98, image rotation 4°, and radial distortion 0.5% at the corner position. The S-distortion was indicated to be negligible. None of these figures was checked experimentally. From the observations made the image rotation and distortions were not noticeable.

4.3 Image Tube #3 - standard mode test

The main purpose of this section is to record some of the basic performance parameters of the standard mode that were not measured on IT #1 (Note: IT #2 was completed by ⓦ Tube Division and delivered, but proved to be gassy - testing therefore proceeded from IT #1 to IT #3). IT #3 was constructed with modified mounting of both input and output windows (see Section 6) giving rise to the increased cathode target dimension of 12.8 cm. The getter appendage was left on the tube, necessitating modification of the coil system to the form shown in Figure 3.14, where the 8 mm gap between coils 2 and 3 accommodates the tubulation to the getter chamber. These changes set the photocathode position at 4.5 cm from the end of the coils instead of 6.1 cm, thereby increasing B-field nonuniformity at the cathode (see

Figure 4.6). Figure 4.13 shows a photograph taken of IT #3 operating in standard mode with a 60.4 per inch mesh shadow-projected onto the input. The photograph was taken actual size and the diameter of the illuminated circle is 7.25 cm. As the useable phosphor diameter is 8 cm and the image size is determined by the photocathode diameter of 7.6 cm, an overall magnification of .95 is indicated. A count of the mesh at the center of the photograph yields 63 per inch, which indicates $M = .96$. The S-distortion is visually evident round the edge, and it is of interest to quantify it to provide a visible comparison to the computed figures. From four readings taken at 90° intervals at $r_{out} = 3.6$ cm, the mean total angular error is 2.4°, which corresponds to the value 0.0032 rad/cm^2 for the S-distortion coefficient used in the computational study. The radial distortion is less apparent, but can be measured by counting the mesh, and is of the order of +3%. Both distortions are significantly bigger than indicated by computation (see discussion of IT #1), which may be due to B-field disturbance near the edge of the image, produced by the Kovar components, or due to a greater degree of E-field non-uniformity then was allowed for. The potential divider chain used to set the electrode potentials is made up so that approximately equal voltage steps are set up, rather than voltage proportional to z-coordinate. This was reasonable on IT #1, but less so on IT #3 where the spacings adjacent to cathode and target are each increased about .5 cm by the mounting flange modification. This discrepancy was discovered too late in the project to be remedied or analyzed.

4.4 Magnifying Mode Test - IT #3

An attempt to operate IT #1 in a magnifying condition failed because of gassiness. When a strongly non-uniform magnetic field was applied the tube would arc and break down. IT #2 was not operable at all, having become gassy in the interval between delivery and setting up for test. Therefore no magnification test was possible until IT #3 was delivered, quite late in the project. Shortness of time and funds meant that experimentation was reduced essentially to a demonstration. For this purpose the condition chosen was that corresponding to the parameter values $b_c' = -.3$ and $z_o = 5$ cm, from the set of results discussed in Section 3.6.2(b_c' is the ratio of gradient to strength of the B-field at the cathode, and z_o is the coordinate of the field-reversal point). Some of the performance parameters and the field distribution computed for this case are shown in Figures 3.18, 19 and 20. In particular we expected to obtain a magnification of about 3.6. The experimental set-up was as shown in Figure 3.14, except that the cathode-target dimension for IT #3 was 12.8 cm instead of 11.75 cm. This discrepancy could be expected to produce a slight divergence from the computed properties. From the computed current density values shown in Figure 3.19 the operating currents for the coils were calcualted as shown in the following table:

Coil	Turns/cm^2	J amp/cm^2	I amp	W_p watts	W_I watts
1	143.5	74.0	.516	10.6	6.2
2	143.5	-97.2	-.675	18.4	10.6
3	143.5	31.6	.220	1.9	1.1
4	143.5	16.44	.115	.5	.3
5	165.4	212.0	1.285	32.8	17.7
		Total Power		64.2	35.9

These currents should set B_c = 138 gauss, the focus condition at 6 KV for the computed case. The column W_p is the practical power obtained from the coil current and resistance, while the column W_I is the idealized power computed on the assumption that the coil cross-section is 100% copper. The two differ by a factor of 1.8, which could be reduced by improved coil design. In our coils insulation layers were used between wire layers in order to keep the winding regular. The use of thicker gauge wire might enable the insulating layer to be dispensed with, thereby increasing the percentage of copper. The power required varies inversely as the areal percentage of copper.

With these coil currents set up the tube was found to focus at 5.17 KV rather than 6 KV. In view of the increased focal length it would be expected to focus at a higher, rather than lower, voltage. Furthermore, the magnification was observed to be appreciably higher than expected. Figure 4.14 (a) shows a photograph of the output of the tube operating with an 80 line/inch mesh shadowed onto the photocathode. Like Figure 4.13, this was taken actual size but, because of the electron-optical magnification, the image in this case covers the full 8 cm diameter of the phosphor instead of being determined by the cathode diameter. A count of the mesh in this image shows an average value 19.6 lines/inch for the two directions, yielding a magnification figure of 4.08. Although the increased focal length should increase magnification, the discrepancy with the original computation value 3.6 is too large. The case was recomputed for a cathode-target dimension of 12.8 cm, with the result M = 3.69 and a focus voltage of 6.6 KV for the same coil currents. These discrepancies were too large to be accounted for by errors in coil modelling or tube positioning, even allowing for possibly greater sensitivity of the system in the magnifying mode. The large M was particularly puzzling in view of the difficulty experienced in the computational study in raising the magnification above 3.7 (Section 3.6.3) even with rather large increases in coil power. The observations suggest that the B-field gradient B_c' is steeper in practice than was allowed for computationally, for that would produce both a higher magnification and a lower focus voltage. This in turn raises again the question of the possible effect of the tube itself on the B-field distribution, which was previously mentioned in Section 3.3. This is discussed further below. Figure 4.14 (b) is similar to 4.14 (a), but the image is masked with a 50 mm square aperture to give a visual appreciation of the area accepted by the WX32193 target. The geometrical fidelity is good with a slight S-distortion in evidence.

To investigate the accuracy of the B-field computation, measurements of the field distribution were first made with no tube in the coil system. These values are plotted as circles in Figure 4.15 where the solid curve is the computed field distribution reproduced from Figure 3.20. The measurements agree with the curve to within experimental error (less than

2% of maximum field). After a lapse of time during which checks were made on the accuracy of the computational modelling and of some aspects of the ray tracing program, it was decided to remeasure the B-field shape with a dummy tube in position. The tube available was one with a window and mounting flange at one end only, the other end being open. This was inserted into the coil system with the window at the cathode position, and the gaussmeter probe was inserted through the open target end. The results of the experiment are plotted as crosses in Figure 4.15. To confirm the comparability of these curves the tube was removed and the field remeasured immediately with results again in good agreement with the computed curve. With the tube in place the field strength appeared to be about 1% greater at the cathode, but more significant is the appreciable increase in gradient to a value $b_c' = -.36$ instead of $-.3\ \mathrm{cm}^{-1}$. Accompanying this is a movement of the field reversal point to $z_o = 3.8$ cm. It is clear from the results presented in Section 3.6 that these changes in field shape are likely to have marked effects on the imaging properties.

The new empirical field values were fed to the ray tracing program for a recomputation of the tube properties, with allowance also made for the increased focal length 12.8 cm. Comparison of the main results with observation is as follows:

	Measured	Computed
focus voltage (B_c = 138 gauss)	5.17	5.62
magnification	4.08	4.13
rotation ϕ	47°	41°

Agreement here is satisfactory and confirms the accuracy of the computation in respect of the first-order geometrical properties. The discrepancies remaining are probably attributable to modelling accuracy and some degree of E-field non-uniformity in the practical set-up. The measured rotation value was taken from Figure 4.14 and is approximate because no great attention was paid in the experiment to the mesh orientation although it was roughly horizontal/vertical. The direction of the rotation is deducible from the appearance of the S-distortion and the fact that the angular error $\Delta \phi$ is computed to be negative. Hence the rotation is clockwise as viewed in Figure 4.14. A divergence in procedure between experiment and computation arises at this point. In practice it is convenient to keep the 5 coil currents constant and focus with the high voltage control, but the computer program is set up to hold the operating voltage constant and focus by scaling the B-field (corresponding to the practice adopted in the standard mode). The computation was run at 6 KV in this case, and the focus field value derived was $B_c = 142.5$ gauss. The focus voltage quoted in the table for $B_c = 138$ gauss is deduced from this result (V proportional to B^2 for constant focal length).

Image Distortion - Figure 4.16 shows the computed distortion parameters $\Delta \phi$ and D as functions of radius at the output. In the corner of the field ($r_{out} = 3.5$ cm) the angular error is $\Delta \phi = -3.4^{\circ}$, which corresponds to the value $S = -.0049$ rad/cm^2. From Figure 4.14(a) a mean value of $\Delta \phi$ from measurements at 4 positions round the edge ($r_{out} = 4$ cm) is -4°, which gives the value $S = -.0044$ rad/cm^2. Radial distortion is not appreciable in Figure 4.14, but measurements do suggest a slight negative value at the edges. The corner value computed for D is -1.4%. Both distortion components are slightly worse than for the original case from which the test condition derived (see Figure 3.18(b)).

Visual Limiting Resolution - This was read at 1 cm intervals across the output and values for the two sides were averaged. Some astigmatism was evident and so readings for two perpendicular directions were recorded. These are shown in Figure 4.17 in comparison with the computed estimates. Separate scales are drawn for reference to input and output. The computer estimates are based on a 0.2 volt electron emission energy, just as are all other estimates given. The reduction in estimated center resolution to 118 LP/mm (referred to input) reflects the increased tube length and reduced operating voltage of 6 KV assumed in this computation, both of which reduce the E-field strength at the cathode. Note that the peak resolution referred to the output is now only 30 LP/mm and so the phosphor-limited condition that held in the normal mode is relieved. The observation should therefore directly reflect the electron-optical capability in this case. The estimated curves would be slightly lower when adjusted to the practical operating voltage, but even so the agreement is satisfactory in view of the simplistic computational method used.

4.5 Attempt to improve standard mode - IT#1

The results of Section 4.2, coupled with those of Section 3.1, confirm that the image intensifier section of the WX32193 has poor resolution uniformity when operating in standard mode. Furthermore, it appears that the problem arises from non-uniformity of the B-field in the cathode region. An experiment was therefore conducted to see if this condition could be improved. For this purpose, coil #5 was removed, and the outer coils were separated into the basic eight segments, providing eight current control variables. A special computer program was set up to define an optimum set of current values to achieve good field uniformity. The question of how to define "good uniformity" is a difficult one. Attention was concentrated on the axial distribution, since field variation generally, merely reflects the variations on axis. A set of 30 points was chosen, that being a convenient number significantly greater than the number of variables. The distribution of the points was weighted in the vicinity of the cathode, that being the most important region for image quality, and a penalty function was defined for the PATternsearch routine, as the sum of the squares of the departures of the field strengths at these points from the specified uniform value. The routine then varied the eight coil currents in search of a set that would minimize the penalty function value. In this form the problem was found to be badly behaved, in that solutions were obtained showing non-smooth coil current distributions. To rectify this, the program was modified so as to constrain the coil currents to be a cubic function of the axial coordinate z of the coil centers. This reduced the number of search variables to four--the coefficients of the cubic. The result was the magnetic field distribution shown in Figure 4.18 (solid curve). The positions of the tube and eight coils are shown, and the "optimized" coil strengths in amps/cm^2 are marked on the coils. For comparison, the equal-current field curve is shown by the broken line (reproduced from Figure 4.7). Currents corresponding to the optimum condition were set up in practice and the tube was focused by voltage adjustment at 7.74 kV, in very good agreement with the computed value of 7.80 kV. The resolution performance observed in this condition was disappointing. Figure 4.19 shows the observed readings in comparison with computed estimates. Whereas the computation suggests a considerable improvement in uniformity over the results shown in Figure 4.8 (corresponding to the broken field-curve in Figure 4.18) this is not borne out by the measurements, which show the same kind of decline off axis, but now with appreciable astigmatism.

Further investigation of this topic was prevented by the need to get on with the magnification testing of IT#3 which was delivered at that point, leaving a serious discrepancy between computation and experiment unexplained. In the light of subsequent experience described in Section 4.3, it seems likely that the unaccounted factor in this experiment was the effect of the tube on the magnetic field distribution. An experimental check was made on the field without the tube, and good agreement with the computed curve shown in Figure 4.18 was found.

5. CAMERA TUBE TESTING

The original program of work was to conduct the testing of camera tubes on the slow-scan test set (Model E154AJ). This idea was modified because the development of that test set to full operational status had been delayed by higher priority projects. The set is useable only in slow-scan mode which, while satisfactory for routine tube testing under standard conditions, is inconvenient for exploratory work because of the slow reaction of the monitor picture to control adjustments. Instead we decided to begin testing on a different test-set, operating at standard TV scan rates. This test set was assembled some years ago in connection with development of the smaller WX31958 SEC camera tube, a forerunner of the WX32193. We will refer to it here as the WX31958 test set. A further change in work plan was occasioned by the fact that an operable WX32193 camera tube did not become available until very near the end of the contract. Because of this delay it was decided to start the test program with an available WX31958 camera tube. Apart from a reduced image format of 25 x 25 mm, the image section of the WX31958 is similar to that of the WX32193, with a focal length of 11.8 cm and focus field strength of about 80 gauss. In combination with its own test set it is a suitable vehicle for a preliminary look at magnification effects. The idea was to do exploratory work with this system and to subsequently transfer an established magnification test case to the slow scan test set when a WX32193 tube was produced.

The WX31958 test-set restricts operation to the continuous read/write mode, whereas the sequential read/write mode is more appropriate to the LST application. The important difference to the magnification study is that the sequential mode permits greater operational flexibility, in that either section of the tube can be turned off while the other section is operating. Thus the field shaping requirements of the two sections could be considered completely independently of each other. In the continuous mode on the other hand, the image section field shaping must be constrained to blend smoothly with the uniform field of the reading section in the target region. This would be an important consideration in the application of field shapes such as are shown in Figure 3.12, as these would be likely to introduce scan-distortions and beam landing problems in a camera tube operating in continuous mode. This is the background that motivated the computational modelling discussed in Section 3.7.

5.1 Tests of WX31958 Camera Tube

Figure 5.1 is a schematic showing the important features of the WX31958. The image section, while conceptually similar to that of the WX32193 is constructed differently, having the accelerator electrodes mounted inside a glass envelope. Figure 5.2 shows the camera head layout with focus coil assembly. There are a total of 17 coil segments each 1" long,.8 of which cover the image section. These coil segments are of 6" internal diameter. The scanning coils slide onto an inner cylindrical. mount into which the reading section of the tube fits. Between some of the coil segments in the target region mumetal washers are used to reduce deflection field penetration into the image section. In this project no particular attention was paid to the effects of these washers on the field shape.

The existing coil segments of the camera head shown in Figure 5.2, together with a specially wound coil #5, were connected so as to approximate the system shown in Figure 3.22. The five segments at the photocathode end were used to make up coils numbered 1, 2, 2A and 3, while the remaining segments were left in series connection as coil #4, covering the target region and reading section of the tube. Coil #5 is similar in design to that described in Section 4.1 for the image tube testing, but with a larger outside diameter of 5.25" and corresponding increase in turns to 1620. A schematic of the coil system and tube is shown in Figure 5.3 (a). The coil segments at the photocathode end are different from the remainder (not as implied in Figure 5.2, the same), and the turns data for all the coils are known only approximately. Therefore no attempt will be made here to relate experiment precisely with computation. That comparison has been adequately covered in Section 4. Using the approximate data the computer program OPTIM (see Section 3.6.1) was used to set the B-field gradient at the photocathode, $b_c' = -.23\ \mathrm{cm}^{-1}$. The current in coil #4 was fixed such that the field in the reading section is near uniform and oppositely directed to that at the photocathode, for reasons discussed in Section 3.7. The coil strengths to do this with minimum power are shown in amp/cm on the coils in Figure 5.3 (a). The resulting computed field distribution in the image section is shown in Figure 5.3 (b), with $B_c = 145$ gauss, which is the focus value for 8 KV operation. The computed magnification is 2.96.

On setting up the tube with the calculated currents the focus voltage was found to be only 4[illegible] KV. This was attributed at the time to modelling inaccuracies, but the experience subsequently obtained with the image intensifier tests suggests that it is related to magnetic field modification by magnetic materials in the tube. To obtain a reasonable working voltage for the SEC target the coil currents were scaled by a factor of about 1.25, whereupon the focus voltage became 6.4 KV. A photograph of the monitor screen resulting from this operation is shown in Figure 5.4(a). The tube was overscanned, so that almost the entire target outline can be seen on the monitor (this is almost clipped at the bottom by the camera mount, but the target edge shading is just visible). This provides a reference dimension in the target plane. Figure 5.4(b) is a similar photograph taken during normal operation of the tube (uniform coil currents 1 through 4, coil #5 turned off). Comparing the dimension of the central test pattern in the two cases, with allowance for the displayed target size, the ratio of magnification is found to be 3.29. Since in the normal mode the magnification is about 0.9, Figure 5.4(a) would correspond to M = 3.0 as expected. The rotation between the two cases measured on the photographs is 74 degrees, compared with a computed value of 62. Figure 5.4(c) shows a third condition, intermediate to the other two, with M = 2.7. The distortions visible in the figure arise from non-linearity of the reading-beam scanning circuitry of the test-set, and possibly some misalignment of the tube in the coil system. Both factors were subsequently improved somewhat. Figure 5.5 shows later photographs taken with a different test chart, the magnification factor in this case being 3.2.

With magnification, an immediate improvement in visual resolution referred to the input was seen, to about 1800 TV lines/inch at M = 3 compared with 1000 at M = .9. This can be seen in Figure 5.6 where (a) shows a case (M = 2.8) in the overscanned condition, and (b) the same case following rotation of the scanning coils, with the line slightly underscanned so that detail could be photographed. The top line of resolution elements in this picture starts at 600 TV lines/inch and progresses in 200 line steps to 2000 TVL/inch at the left. 1800 TVL/inch is equivalent to 36 line-pairs/mm, still a long way from the limit of the image-section which is about 100 LP/mm (see image-intensifier measurements given in Figure 4.17). At either magnification the observed resolution is largely limited by the 10 MHz bandwidth of the test-set, with a contribution from the reading beam. In the magnified mode the resolution referred to the output is, of course, somewhat less than in the standard mode, and so the improved resolution of center detail is obtained at the expense of total information content of the transmitted picture.

There appeared to be no unusual effects associated with operating in the magnifying mode, apart from image rotation evident in the photographs.

The reading beam focus and scanning were adjustable in the normal manner, and beam landing quality appeared to be as good as in the standard mode. Of course, use of the WX31958 tests only the central part of the magnetic field, and there could still be problems with the reading beam conditions over the larger image format of the WX32193.

The only problem with our setup was heating of the tube faceplate by coil #5 which dissipates about 50 watts in the M = 3 condition. Continuous operation time was restricted to avoid any possibility of damage to the tube and, with this precaution, no effects on tube functioning due to the heating were observed. Reduction of the heating problem is discussed elsewhere.

Prior to the experiment shown in Figure 5.6 some special coils were wound and mounted on the system in positions 1 and 2, making the final arrangement shown in Figure 3.22. These are much stronger than the standard WX31958 coils, the intention being to provide a greater range of test conditions, possibly including the alternative case of positive reading-section magnetic field discussed in Section 3.7. The system proved to be less predictable than the image intensifier tests, however, probably due to some interaction of the WX31958 with the B-field distribution, and experimentation with alternative test conditions was restricted by shortage of time.

5.2 Tests of WX32193 Camera Tube

Rather late in the project a good operable WX32193 was manufactured. This was set up for testing in the WX31958 test-set. With the larger image format of this tube, problems were encountered due to the limitations of the test-set. Insufficient power was available to scan the 2" target under the standard conditions and so it was decided to reduce the magnetic field strength in the reading section. To do this, coil #4 in Figure 3.22 was reduced to two 1" segments covering the target, and the remaining segments back to the gun, referred to now as coil #4A, were supplied independently with a lower current. Figure 5.7 shows photographs of the monitor screen taken with the tube operating in (a) a unit magnification condition and (b) the same conditions as were used for Figure 5.6 (a). The shading of the corners in both pictures is due to poor collimation of the reading beam caused by magnetic field non-uniformity in the region of the target. This is the problem of matching the write/read sections of the magnetic field, discussed in the introduction to Section 5. Here it is introduced through choosing the current I_4 to suit the image section rather than the reading section. Unfortunately, time was not available to repeat this experiment or the trouble might have been eliminated. The magnification factor in Figure 5.7 (b) appears to be about 3.4, surprisingly different from the value 2.8 found when operating the WX31958 with the same coil currents (Figure 5.6). The photocathode voltage is also significantly different. The focal length of the WX32193 image section is 0.5 cm greater than that for the WX31958, due to the faceplate mounting modification (see Section 6), but this difference is too small to account for the observed performance discrepancies. This suggests strongly differing interactions with the B-field distribution on the part of the two tubes.

The central spot in both pictures is not a target blemish but a mark made on the input window to indicate the center. Around this, for purposes of setting image section magnification, are drawn a sequence of concentric circles of diameters 1", 1.5", 1.8", and 2". These are visible in Figure 5.7 (a) where the 2" circle is arranged to just touch the edges of the target, indicating precisely unit magnification. The cause of the white areas around the edge in Figure 5.7 (b) is not known. Figure 5.8 shows measured MTF curves for the central region of the image at the two magnification settings. Both curves probably reflect the band width limitation of the test-set more than the tube performance. In view of the relatively high resolution of the image section (80 to 100 LP/mm referred to the input) it is not clear why the curves do not differ more markedly.

6. TUBE MANUFACTURE

The project plan budgeted for a total of six tube starts to be made with the objective of obtaining at least one operable image intensifier and one operable camera tube, plus a back-up tube of each type if possible. Ignoring some false starts that ran into early difficulties, six starts were finally logged. Their fates are summarized in the following table (G = good, F = fail).

Start	Aim	Result	Date 1974	Serial No.	Comment
1	IT	G	July	7426811	IT#1 125 μA/ lumen
2	IT	F	July	--	Window fracture at heliarc
3	IT	F	Sept 13	7435665	IT#2 leaked after tip-off
4	IT	G	Oct 6	7444096	IT#3 65 μA/ lumen
5	CT	F	Oct 11	--	Hot leak on pump
6	CT	G	Nov 15	7439955	CT#1 70 μA/ lumen

This represents a good overall record of success, the main flaw being the rather late timing of IT#3 and CT#1 which caused the test program to be squeezed at the end. IT#3 was vital because IT#1 gradually became gassy and could not be operated under magnifying conditions.

A schematic of the tube construction is given in Figure 6.1 which is split at the axis, the upper half showing details for the

WX32193 camera tube image section with MgF_2 input window, and the lower half showing details of the image intensifier with glass input window designed for this project. Differences between the two are negligible for electron-optical considerations. From a constructional viewpoint, the image intensifier design involves simply cutting short the ceramic stack at the target mounting ring and terminating with a glass window/flange assembly similar to that used at the input end. In the camera tube two heliarc welds are involved, one at the window flange and the second at the junction of the image-section and reading section, immediately to the left of the target, the latter being the final operation in assembling the complete tube. For the image intensifier an additional heliarc weld is involved to attach the output window assembly to the ceramic stack assembly.

Problems were encountered with the heliarc welds at the two ends of the intensifier. Start #2 was lost when the input window fractured while being attached to the completed ceramic assembly. The design for the window mounting was subsequently modified as illustrated to in Figure 6.2. In the modified form the window flange is reversed, and the window sealed on the opposite side. This increases the distance between the window seal and the welding point, and provides better stress-relief. In addition to this, improved heat-sink fixtures were employed on heliarc welds subsequent to Start #2. This modification was applicable to both windows. However, some output windows, with settled phosphors, mounted according to the original design remained from the batch made early in the project, and these were used up, relying on the new heat-sinks to prevent problems. Start #3 was successful in this respect (but failed for other reasons). An attempt at Start #4 was aborted when its output window cracked during the weld. At this point a new batch of phosphors was settled on windows mounted according to the modified design, and the problem did not recur in Starts 4, 5, and 6. Figure 6.3 shows photographs of IT#2 with (a) the input window mounted in the modified manner and (b) the output window according to the original design. The modification adds 0.2" to the internal length of the tube at each end, increasing the photocathode-target distance from 11.8 cm (IT #1) to 12.3 cm in IT #2 and CT #1, and to 12.8 cm in IT #3. The appendage at the side of the tube contains the passive getter. In the case of IT #1 the appendage has been tipped off but, as that tube developed gas problems during use, it was decided to leave the appendage on subsequent intensifier tubes. The camera tubes have the getter at the gun end.

IT#2 was really lost during manufacture when a fault opened in one of the kovar rings at the middle heliarc weld. This was simply a chance material failure and so did not raise any design questions. The leak was sealed sufficiently for processing to be completed, but the tube remained operable for only a short time after tip-off. Start #5 appeared to be a good camera tube when assembled but developed a leak during bake-out and could not be pumped down. Out of the oven, the leak was not in evidence and so could not be traced, and the tube was finally scrapped.

7. CONCLUSIONS

Computational Accuracy. The experimental results from the image tubes (Section 4) confirm the validity and usefulness of the computational modelling. However, it was found that the magnetic field distribution in the coil system may be appreciably modified by the presence of the tube. To obtain the highest accuracy allowance must be made for this, either by the use of more sophisticated B-field computation, or by making use of empirical B-field data (as described in Section 4.4).

Standard Operation WX32193. The performance of the WX32193 image section is degraded by non-uniformity of the B-field provided by the standard coil system. This effect is severe enough to contribute to resolution non-uniformity in the complete camera tube. Improvement in the coil design is desirable to improve B-field uniformity in the region near the photocathode. Such design work should take into account the influence of the kovar flange on which the window is mounted. A simple expedient might be to extend the coil at the front, or to boost the current to the front coil section.

The electrode design is capable of providing a highly uniform E-field, provided the right voltages are applied. The design modification to the input window mounting (see Section 6) results in increased spacing from photocathode to first electrode, which may need to be figured into the voltage selection.

Requirements for High Magnification. The B-field characteristics necessary to achieve high magnification are primarily high field strength with sharp negative slope at the object plane. The field should drop to a low level in the first 1/3 to 1/2 of the tube length and remain low (either positive or negative) from that point to the target (as exemplified by Figure 4.15). Detailed shaping of the tail of the curve can provide a degree of control over aberrations, but also adds to the power demand. However, the field shapes determined purely on a minimum-power basis do appear to provide a good overall standard of image quality.

The image section length essentially determines how high a magnification can be achieved and also the power requirement. This has not been stressed in the body of the report, because the tube design was regarded as frozen. The form of the field shape exemplified by Figure 4.15 suggests a strong magnetic lens close to the photocathode, with relatively field-free space out to the target. Moving the target further away increases the image distance, permitting higher magnification for a given lens strength. This is sufficiently important to warrant example. In allowing for increased length from 11.8 to 12.8 cm in Section 4.4, it was found that for a fixed operating voltage (6 KV) the magnification increased from 3.61 to 3.69 (2%) and the power reduced from 36.0 to 32.7 watts (9%).

The use of non-uniform E-field can be advantageous. It is found that shaping the E-field so that it is strong at the photocathode, but diminishes towards the target, can help to achieve higher magnification for a given coil power. The advantages are dependent on circumstances and must be weighed against practical considerations of switching both electrode voltages and coil currents in the LST environment. This effect should be kept in mind as a design tool.

Practical Demonstration. The image intensifier experiments have demonstrated a magnification of 4 with good image quality over the 50 x 50 mm image format, for an actual power consumption of 64 watts at 5.2 KV. For operation at 8 KV the power would increase, in proportion, to 98 watts. The B-field shape used in the experiment, is considered to be close to an optimum as regards the power demand for this magnification (given this particular tube geometry). Hence, efforts to reduce the power should concentrate on the coil design, where considerable improvement is likely to be possible. The B-field design approach for the demonstration concentrated mainly on power reduction, and the good image quality appeared as a bonus. As compared to the standard operation of the tube, the resolution uniformity is improved. Figure 4.17 shows 60 LP/mm at the edge and 30 LP/mm in the corner of the image format at 5.2 KV (observed figures referred to photocathode). At 8 KV the corner figure should come closer to 40 LP/ mm. In addition, Figure 4.16 shows that the radial distortion is decreased to a negligible level, while the S-distortion is not much changed, and is in any case probably less than that arising from the scanning system of the camera tube. The results of Sections 3.4.3 and 3.5 suggest that some improvement in resolution uniformity might be obtainable but the increase in power demand is likely to be large.

Zoom Capability. Although not demonstrated it can be asserted on the basis of the computations that the above performance could be essentially maintained over intermediate magnification values. The coil currents would be programmed on curves like those shown in Figure 3.16. Five separate coils were used in the study to provide flexibility. For the type of B-field curves considered, the number of variables could be reduced by combining coils #3 and 4, at a small cost in total power. Coils #1 and 5 also might be combined, leaving only 3 variables for the image section control. This is the minimum number for wide range zooming because the negative contribution of coil #2 is essential to high magnification.

Reading-Section Requirements. The reading-section focus current would be a separate consideration from the above - operating in continuous read/write mode would necessitate four distinct currents (three variable). For the sequential write/read operation most of the coil covering the reading section could be turned off during writing, or it could be left on. The last image control section (coil #4 in Figure 3.14) overlaps the target and would adjust for either condition. An advantage of the type of B-field shape suggested (Figure 4.15) is that it lends itself to good matching with the reading-section field. Development work could be done using the continuous mode, which is convenient, and the final result would be applicable in either continuous or sequential modes.

The camera tube testing did not indicate any interference with reading section performance due to the image-section field shaping. However, operation of the WX31958 tested only a 1" image diameter, and so leaves open the question of beam landing quality outside of that area. The WX32193 tests on the WX31958 test-set were not adequate to give valid information on that subject. It is safe to assert that any matching problem revealed by further camera-tube tests could be overcome by tailoring the image section field shape, without significant effect on the zoom capability. This would probably involve lifting the tail of the

B-field shown in Figure 4.15 to a slightly higher level. It is re-emphasized that the only relevance of this is to the convenience of development in continuous mode.

Power/Heat Problem. The most significant problem to be overcome in the power demand of the magnifying mode. The dissipation of 50 watts in coil #5 (8 KV operation) close to the photocathode is probably a greater problem than the overall requirement of 98 watts. To measure the extent of the temperature problem an experiment was run with a dummy image tube in the system for an extended period of operation with a thermocouple taped to the center of the faceplate. The temperature was found to reach 60°C after 1 hour and nearly 80°C after a further hour. It is clear, that this is the crucial consideration in relation to the LST because for low-light-level viewing the photocathode must be kept cool in order to minimize noise produced by thermionic emission. In this experiment no precautions were taken to minimize the temperature rise. Coil #5 was pushed close to the input window with only a thin plastic washer between for electrical insulation.

There are three aspects to overcoming this problem. Firstly, measures can be introduced to remove heat generated close to the input window. Secondly, the distribution of the power dissipation can be changed so as to load coil #5 less. Thirdly, the overall power level can be reduced by attention to the individual coil winding design.

In respect of the first of these, our test system is clearly bad, as can be seen from Figure 4.3. To conduct heat away from the tube the coil mounting cylinder would be metal instead of plexiglass, possibly with fins between the segments. This would be extended as a shield between coil #5 and the faceplate, including the inside cylindrical surface of the coil, and an insulating layer added to reduce conduction and radiation to the window.

Power distribution could be improved by optimizing the coil arrangement in a more careful design process. The power to coil #5 could be reduced by loading #1 more, even though this leads to some increase in total power. The scope for reduction of total power is quite large since our test coils were found to dissipate 1.8 times the calculated value based on the "solid copper" model (see Section 4.4). The use of thicker wire permits a good regular winding to be obtained without the need for inter-layer wrappers, and the above figure could approach 1.25, a 30% saving.

Still further scope exists for power reduction in the use of iron. Based on the results of Section 3.5 a factor of 2 reduction in the power to coil #5 in particular, seems a reasonable expectation. A possible disadvantage to this approach may be complication of the design problem for the unit magnification case, as the iron may make it difficult to achieve the desired uniformity of field. However, this problem may already exist due to the kovar elements of the tube (see Section 4.5). In summary, there are good grounds for optimism that the photocathode heating problem can be overcome.

Stability. In the unit magnification case, power supply stability tolerances were established as 0.25% on the coil currents, and 0.5% on the high voltage. These are probably conservative because our viewing methods were of higher capability than the reading section of the camera tube. The corresponding measurements were not made in the magnified condition owing to shortage of time. Five separate current-regulated power supplies were used for the coils, and there appeared to be a slight stability problem with two of them due to temperature rise in the supplies themselves. The impression gained is that this is not likely to be a severe problem, but further work would be necessary to enable a more quantitative answer to be given.

8. RECOMMENDATIONS

The results presented are sufficiently encouraging to warrant serious consideration of the zoom capability for the LST camera tubes. The form of magnetic field used for the image intensifier demonstration (Figure 4.15) should be used as the basis for serious design work on a practical coil system, because of the good all-round performance described. The central problem to be solved is that of heat dissipation, and strong grounds for optimism on this have been outlined.

It is suggested that consideration be given to increasing the length of the image section of the WX32193 by some moderate amount (e.g. 1".) Benefits would accrue from this in respect of power requirements and image uniformity, at no real cost other than the slight increase in physical bulk. The electron optical trade-off is center resolution reduction as the electric field strength is reduced. Since in the present condition the center resolution capability at 8 KV is in excess of 150 lp/mm, a reduction of 25% would not be observable in the overall camera tube performance. A power saving of over 20% might be obtained at M = 4.

Design work on the coils should take into account the effect of the kovar tube elements on the field shape. Computationally this implies that an approach such as is described in Section 3.5 should be adopted on a more serious scale. This would allow a realistic optimization of coil shapes, positions, and loadings, to be performed with the objective of reducing the power in coil #5. A 10% reduction can reasonably be expected. In addition, with improved coil winding it should be possible to increase the efficiency of all the coils by 20%. Using these conservative estimates, the power requirements for M = 4 reduce to 29 watts in coil #5, and 60 watts total.

Further substantial power reduction might be achieved by the use of iron shielding to concentrate the field strength near the photocathode. The computational development suggested in the preceding paragraph would permit a detailed study of this possibility. Should it prove practical, a power reduction of 50% could be expected in coil #5, and perhaps overall. In conjunction with this, careful consideration should be given to the impact of magnetic materials on the achievement of a uniform field for the unit magnification condition. The requirements for improved performance in the standard mode of operation may conflict with those for power reduction in the magnifying mode.

On the experimental side, construction of the coil system should incorporate measures for removing heat from the tube and dissipating it to the outside. Further experiments with the image intensifier system could be conducted to quantify the power supply stability demands of the high magnification mode of operation.

9. ACKNOWLEDGEMENTS

The authors are grateful for help received from many colleagues at Westinghouse Research Center and Westinghouse Tube Division, in particular Mr. R. Kankus for organizing the tube manufacture, and Mr. C. F. Wood for advice on the use of the optimization programs.

10. REFERENCES

1. J. L. Lowrance, "Large Space Telescope Sensor Development", proceedings of NASA Symposium: "Advanced Electro-Optical Imaging Techniques", Washington, D.C., September 1972, NASA SP-338, p81.

2. J. Vine, "Electron Optics", Chapter 10 of "Photoelectronic Imaging Devices" by L. M. Biberman & S. Nudelman, Plenum, 1971, p. 193.

3. See Reference 2, p. 230.

4. P. R. Collings, Westinghouse Electronic Tube Division, internal memorandum, May 4, 1966.

5. C. F. Wood, "Application of Direct Search to the Solution of Engineering Problems", Ⓦ Scientific Paper 6-41210-1-P1, October 12, 1960.

6. "Computation of the Spatial Resolution of the Gamma Ray Camera", C. F. Eve, Ⓦ Res. Report 72-1C2-CAMRA-R1, November 1972.

APPENDIX 1 ELECTRON OPTICS COMPUTATION

The computational analysis of an electron-optical system involves three distinct computations: (a) electrostatic field distribution, (b) magnetic field distribution, and (c) ray tracing. The main aspects of the program package used in this contract in relation to these tasks are briefly described in the following.

A1.1 Electrostatic Field Computation

This involves the solution of the Laplace equation in an axially symmetric system when the electrode shapes and voltages are specified. The method of over-relaxation is employed. The meridian plane of the system is overlaid with a finite-difference net as shown in Figure 3.1, and the solution is sought in the form of the array of values of the electrostatic potential at the mesh points. The relaxation method is an iterative technique whereby successive approximations to the solution are systematically improved. The electrode shapes are specified to the computer as data so that the mesh points corresponding to them can be held fixed at the specified voltages during this process. The iteration continues until the changes in the solution at successive cycles become negligible. The solution then obtained is an approximation to the true solution of the Laplace equation, with errors that depend on the fineness of the net employed, and the magnitude of the field derivatives. When the field is nearly uniform a relatively coarse relaxation net can provide acceptable accuracy, as is the case in Figure 3.1.

The array of potential values representing the solution is stored in the computer for later use by the ray-tracing program. To compute the forces acting on an electron at a general point in the field, the ray-tracing program uses numerical interpolation and differentiation formulas on this two-dimensional data array.

A1.2 Magnetic Field Computation

The data required by the ray-tracing program to define the magnetic field distribution is a one-dimensional array of values, representing the field strength at equally spaced intervals along the axis of symmetry. The magnetic field components B_r, B_z at a general field point r,z are expressible in terms of the on-axis distribution B(z) as

$$B_z = B(z) - \frac{r^2}{4} B^{(2)}(z) + \frac{r^4}{64} B^{(4)}(z) \ldots \qquad \text{(A1.1a)}$$

$$B_r = -\frac{r}{2} B^{(1)}(z) + \frac{r^3}{16} B^{(3)}(z) - \frac{r^5}{384} B^{(5)}(z) \ldots \qquad \text{(A1.1b)}$$

The ray-tracing program uses numerical interpolation and differentiation of the data array in conjunction with these equations in determining the forces on an electron at a general field point. The reason this approach is applicable is that all the sources of the magnetic field (coil current density) are a long way from the axis, and ray-tracing is confined to a relatively paraxial region. The same technique is available for the electric field in principle, but is invalidated for this application by the presence of electrodes at the axis (photocathode and target) introducing discontinuities in the axial field distribution. Hence the need for the two-dimensional data array described for the electric field. The ray-tracing program normally uses terms up to the fourth derivative in equations (A1.1). In this project checks were made on the adequacy of this in representative cases, by dropping the fourth derivative terms and confirming no significant change in results.

The magnetic field computation problem is therefore to set up the axial data array. Three ways of doing this have been described in Section 3.2. In the cases of purely algebraic axial definition, and of definition by solenoids without iron, the computation is simple and is incorporated into the ray-tracing program as a preliminary task. The third facility supplied is for direct input of the axial data. The data in this case may be empirical as in Section 3.3, or it may be obtained by means of a computation separate from the ray-tracing. The latter was the case in the analysis of the effects of iron pole-pieces described in Section 3.6.

A1.3 Ray Tracing

The computational problem of ray-tracing is the integration of the equations of motion of an electron in electric and magnetic field distributions defined as above. This is accomplished in a straightforward stepping technique, algebraic details of which have been published elsewhere (See Reference 2). It is appropriate to discuss here some of the more practical aspects of the problem. Ray-tracing is only a means to an end, the end being an expression of the imaging qualities in a fairly concise way. An important concept in connection with this, is that of differential ray-tracing, which is the technique of computing first-order ray differences, or neighboring paths in a truly limiting sense. Consider the computation of the first-order paraxial focus in the image intensifier problem. This is defined by an electron emitted from the center of the photocathode in a direction tangential to the surface, with a vanishingly small emission velocity v_o (zero axial component of emission velocity). Computers cannot handle vanishingly small numbers with good accuracy, but on the other hand, if v_o is chosen too large then the computation may stray so far from the axis that the result obtained is affected by spherical aberration, which is a third-order effect. This can present the user with problems. The differential technique involves the formulation of the numerical method in such a way that only first-order effects are allowed to enter into the computation. Higher order terms are excluded from the equations and so cannot affect the result regardless of the choice of v_o, which becomes simply a scaling factor chosen for computational convenience. The radial coordinate r_c of the path computed in this way is directly proportional to v_o and is related to the actual coordinate r_a of an electron in the system by

$$r_c/v_o = \lim_{v_o \to 0} (r_a/v_o) \qquad \text{(A1.2)}$$

The point at which r_c becomes zero is the true first-order focus (ignoring truncation errors due to the stepping interval size).

In application to this project, the first task of the ray-tracing program is to establish a first-order paraxial focus at the user-specified target position. It does this by adjusting the magnetic field strength in an iterative loop. The user supplies a starting guess for B_c, the field strength at the cathode. The data array defining the field distribution shape is immediately scaled to conformity with this value, and the first-order focus is computed. The result is compared with the specified target position and a new estimate for B_c is calculated to bring the two into closer agreement. This process is repeated until the focus is close enough to the target--a tolerance of 0.1 mm typically requires four or five iterations. With this focus field strength set, the program then proceeds to compute the imaging properties of the system in the plane of the paraxial focus.

The first property is paraxial magnification, which is computed by the differential technique. Consider a principal ray leaving the photocathode at radius r_{in} and arriving at the focal plane at radius r_{out} (the principal ray from an object point is defined as the path followed by an electron emitted with zero energy from that point). The paraxial magnification is defined as

$$M_o = \mathcal{L}t_{r_{in} \to 0} \, (r_{out}/r_{in}) \qquad \text{(A1.3)}$$

This limit is computed directly.

The off-axis imaging properties are computed for a set of object points defined by the user. Typically about six points would be specified across the object field, usually on the x-axis (defined as in Figure 2.1). For each object point the principal ray is computed. This is a non-differential computation that uses field strengths determined locally at the electron position, and therefore incorporates the complete aberrations of the system. The position where this path crosses the paraxial focal plane is accurately determined, and from it are calculated the magnification and rotation, and hence the distortion values, according to the definitions given in Section 2. Concurrently with the principal ray, two "secondary" rays are computed differentially with respect to it. Each of these is for an electron with emission velocity v_o tangential to the cathode surface, one being radially directed and the other perpendicular to that (θ- directed). These rays reveal the first-order departures δ from the principal ray, which determine the resolution relating to the object point. The reason for having two secondary rays is the astigmatic effect mentioned in Section 2. At the paraxial focal plane, each δ value implies a value for the first-order confusion disk diameter d_1 used in equation (2.9) to obtain the resolution estimates for the radial and tangential directions.

No computations are carried out for electrons emitted with non-zero normal-velocity components. These relate to chromatic aberration, which is a second-order effect universally defined by equation (2.7). This is directly calculable from knowledge of the E-field strength at the object point, and so does not require any ray-tracing.

An additional second-order (in v_o) effect is the coma which ideally would be computed for off-axis points and figured into the resolution estimates. The program has not been developed to do that, and it is not known how important that contribution might be.

APPENDIX 2 OPTIMIZATION TECHNIQUE

Program OPTIM mentioned in Section 3.6.1 searches for coil currents that establish a set of field conditions (constraints) specified by the user, with the minimum possible power. The main computational tool used to do this is the general optimization subroutine PATternsearch.$^{(5)}$ Consider a problem of five geometrically fixed solenoids wherein we wish to hold specified values $\overline{B}_c$ and $\overline{B}'_c$ for the strength and gradient of the magnetic field at the cathode. Let I_j, $j = 1 \ldots 5$ be the current variables. Let h_j and g_j be the field and gradient at the cathode produced by unit current in the jth coil when all other coils are turned off. By the superposition principle, the field and gradient at the cathode for a general set of current values will be

$$B_c = \sum_{j=1}^{5} h_j I_j$$

$$B'_c = \sum_{j=1}^{5} g_j I_j \qquad \text{(A2.1)}$$

In order to apply two constraints, use must be made of two of the variables--say I_4 and I_5. Given any set of values I_1, I_2, I_3, values of I_4 and I_5 can be computed such that $B_c = \overline{B}_c$ and $B'_c = \overline{B}'_c$. From A2.1) we have

$$h_4 I_4 + h_5 I_5 = \overline{B}_c - \sum_{j=1}^{3} h_j I_j$$

$$g_4 I_4 + g_5 I_5 = \overline{B}'_c - \sum_{j=1}^{3} g_j I_j \qquad \text{(A2.2)}$$

which can be solved for I_4, I_5. In the search process I_1, I_2, I_3 can be varied freely--they define a three-dimensional search space. For a chosen point in the space, values of I_4 and I_5 are computed from equation (A2.2), and the power into the system is calculated as

$$W(I_1, I_2, I_3) = \sum_{j=1}^{5} I_j^2 R_j \qquad \text{(A2.3)}$$

where R_j are the coil resistances. This is called the penalty function, which has a unique value for every point in the search space. Subroutine PAT is set up to receive a value for the penalty function (from the user program) in return for a set of coordinates (I_1, I_2, I_3). Given a starting guess by the user it moves through the search space in a systematic way reducing the penalty until it can find no further improvement.

Program OPTIM computes the coil strength coefficients h_j, g_j and resistances R_j from the geometrical coil data. A separate subroutine is set up, called by PAT, which takes any given coordinate set (I_1, I_2, I_3) and returns the corresponding value of W. Inequality constraints are imposed on the search variables used by PAT. These are specified by the user as maximum and minimum values for each variable, and define a bounded region to which the search is restricted. Note that in this application I_4 and I_5, computed by solving equations (A2.2), cannot readily be restricted. Care was taken in running the problems described in Section 3.6, to choose for PAT variables those coil currents most likely to need limitation. In the event, only coil #5 was found to hit its limit, set at about 200 amp/cm^2.

The description given can readily be extended for additional field constraints. Up to four were employed in this project, reducing the search space to one dimension.

APPENDIX 3 MTF COMPUTATION

Given a line-spread function (LSF) $y(x)$ for an imaging system or component, measured with the aid of a slit whose width is small in relation to the modulation frequencies of interest, the modulation transfer function (MTF) is given by the Fourier transform:

$$R(f) = A \int_{o}^{\infty} y(x) \cos(2\pi f x)\,dx \tag{A3.1}$$

where A is a normalizing constant, set to make $R(o) = 1$, and f is frequency. The units of f are the inverse of those of x. The LSF measurements are described in detail in Section 4.1. Typically 20 to 30 data points are taken from the measured profile, equally spaced from $x = 0$ to some maximum x_1 such that $y(x_1)$ is a few percent of $y(0)$. The MTF program fits a cubic spline approximation $\overline{y}(x)$ to the given data values, replaces the upper limit of integration in equation (A3.1) by x_1, and employs exact algebraic expressions (6) for the approximate MTF

$$\overline{R}(f) = \overline{A} \int_{o}^{x_1} \overline{y}(x) \cos(2\pi f x)\,dx \tag{A3.2}$$

evaluated at a range of values of f specified by input.

C3

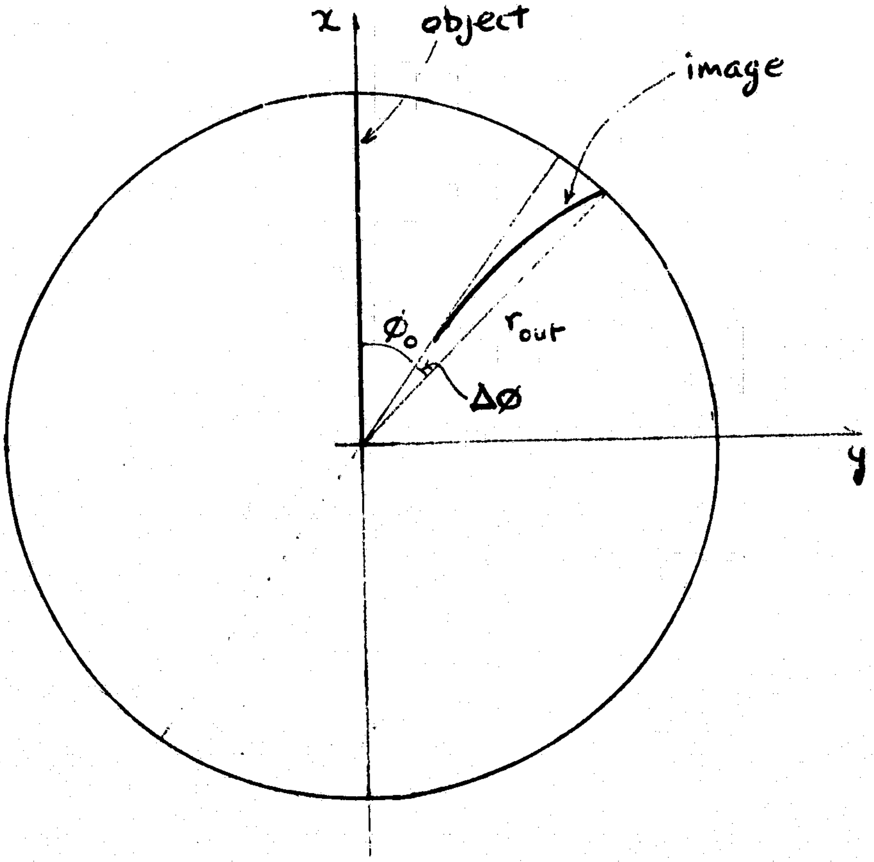

FIGURE 2.1 Definition of Rotation and S-Distortion

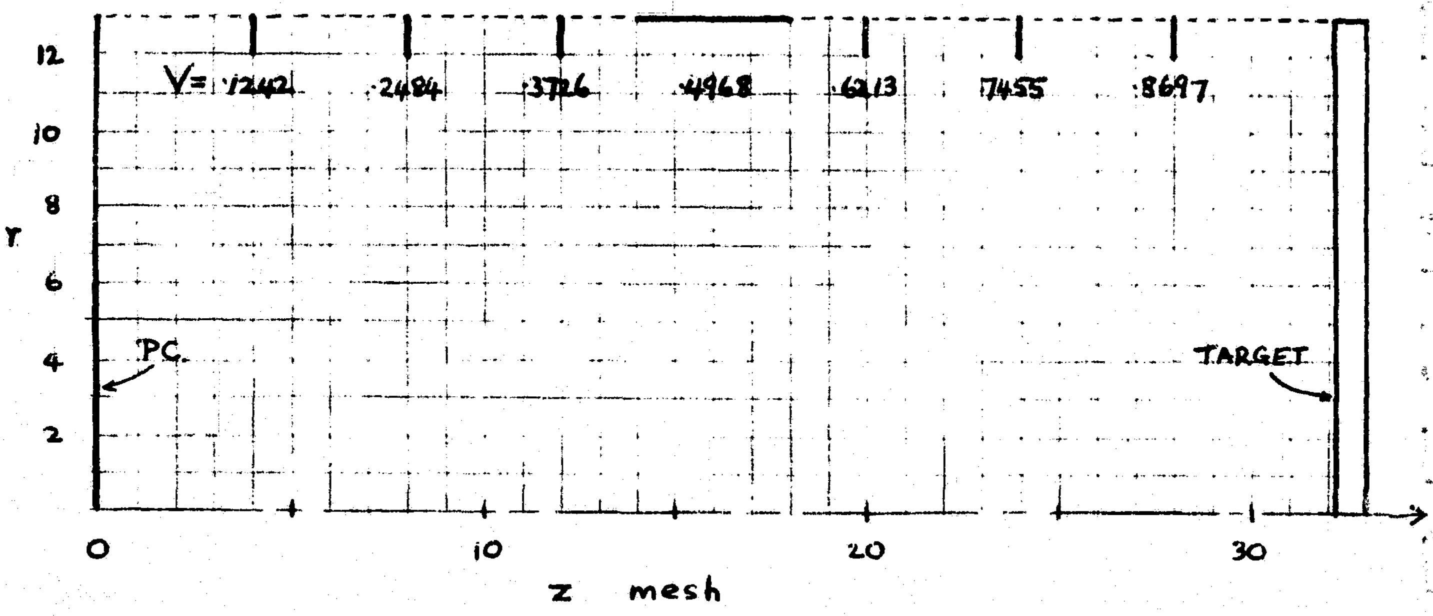

FIGURE 3.1 Computer Model for E-Field Distribution

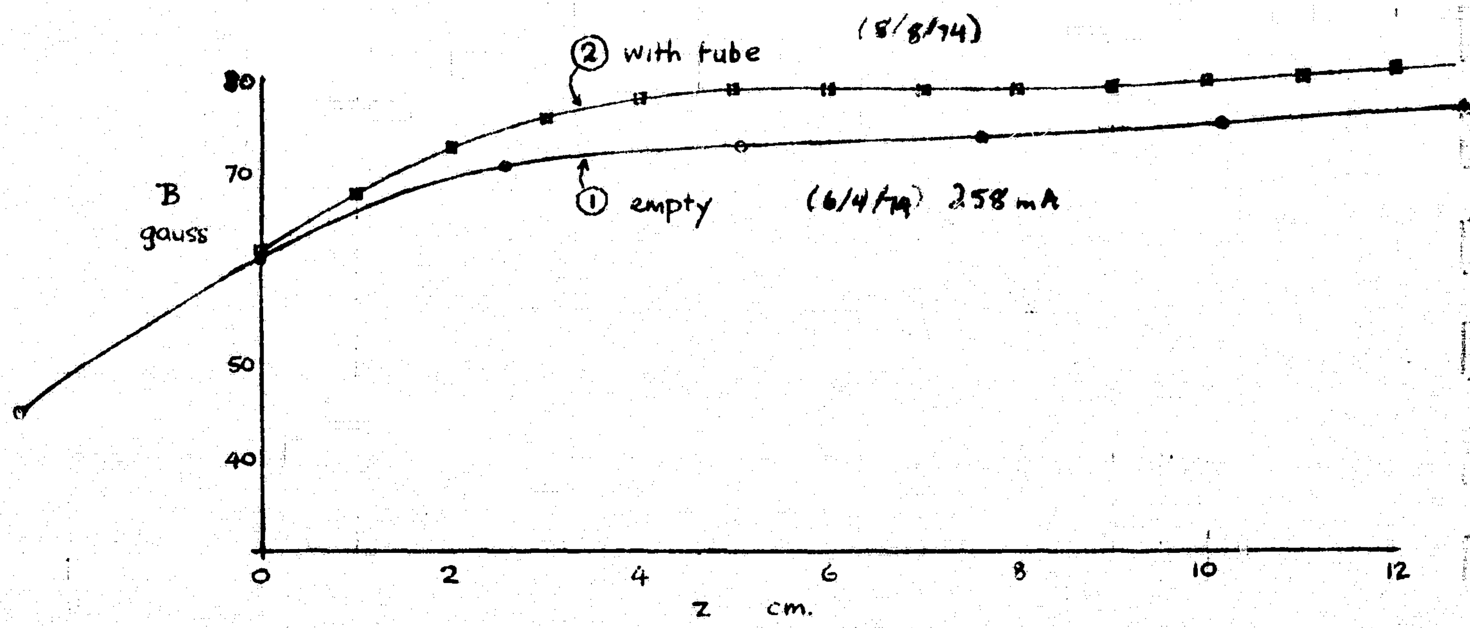

FIGURE 3.2 Axial B-Field Distribution of Standard Focus Coil

Curve 1. Without Tube (6/4/74)
Curve 2. With Tube (8/8/74)

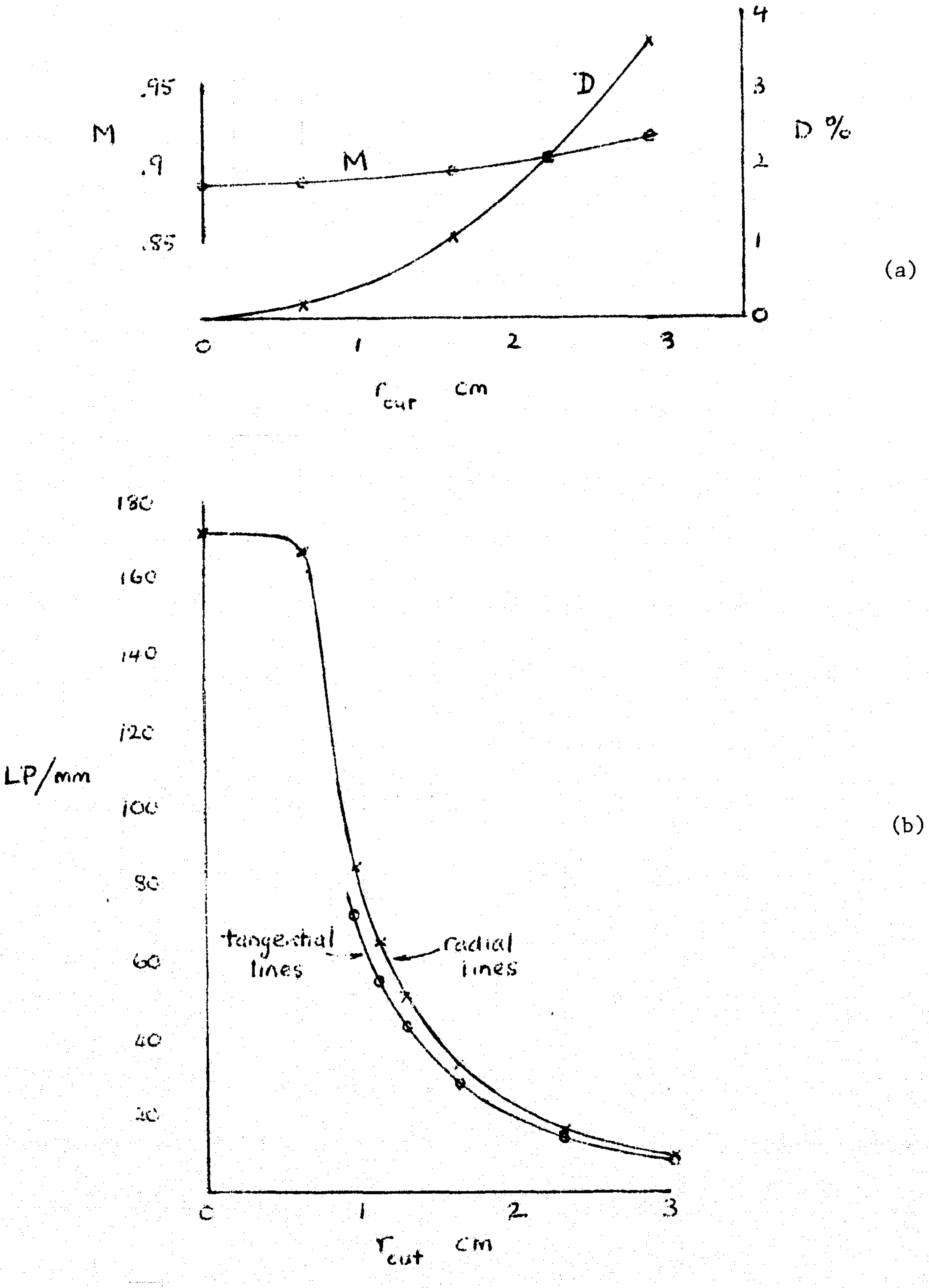

FIGURE 3.3 WX32193 Image Section Computed Performance in Standard Operating Mode

(a) Magnification and Distortion vs. Radius
(b) Limiting Resolution vs. Radius

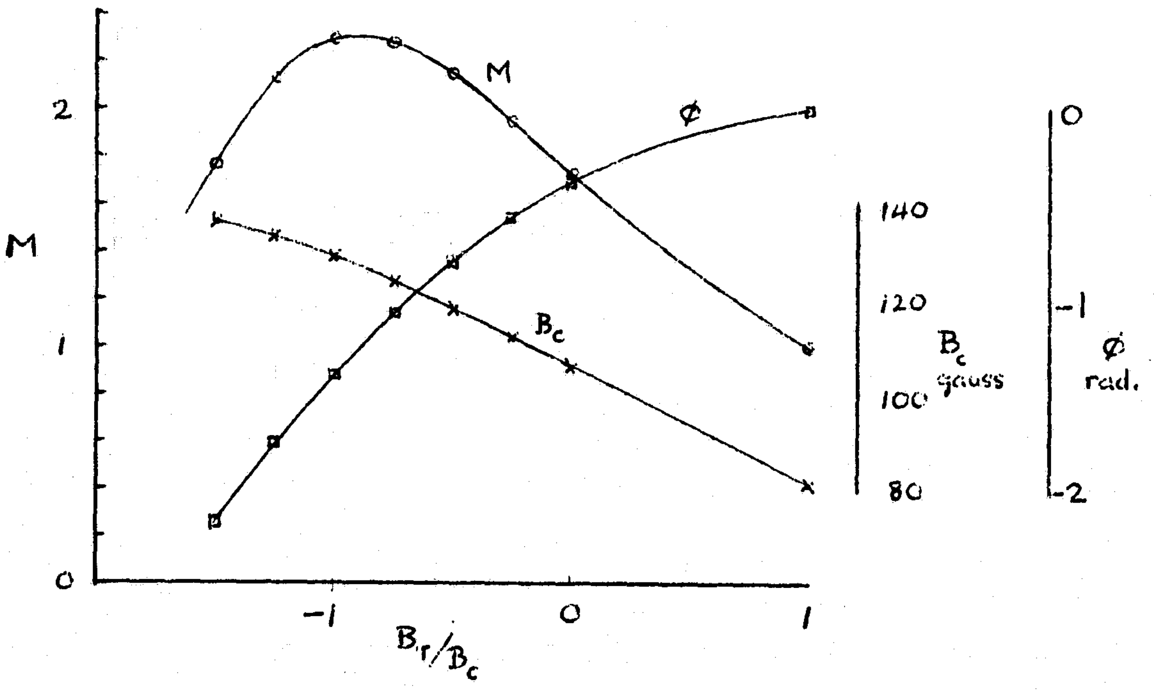

FIGURE 3.4 Linear B-Field Distribution. Paraxial Performance vs. Field Strength Ratio $B_T/B_c = b_1$

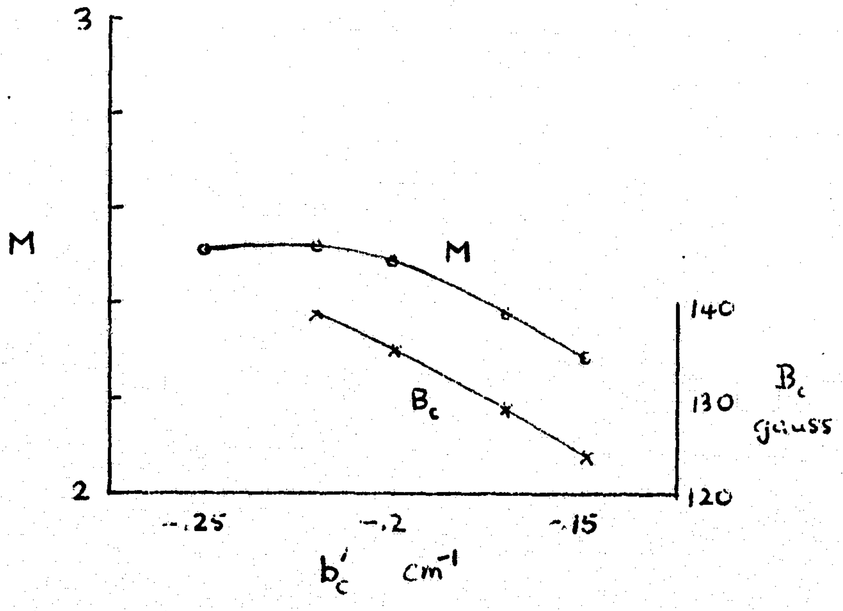

FIGURE 3.5 Parabolic B-Field Distribution. $b_1 = -.75$ cm^{-1}

Paraxial Performance vs. Normalized Field Gradient $B_c'/B_c = b_c'$

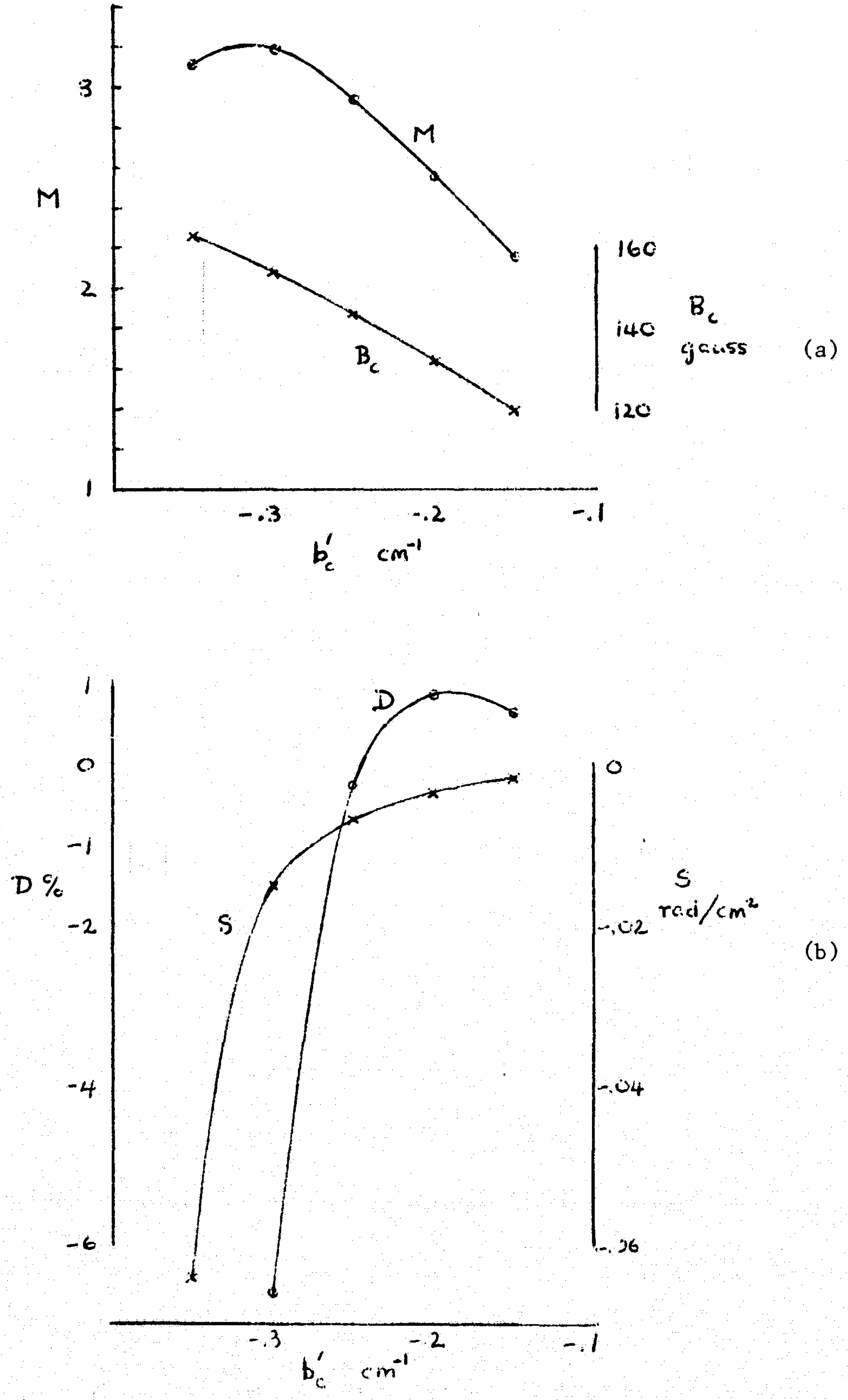

FIGURE 3.6 Parabolic B-Field Distribution. $b_1 = 0$

Performance vs. Normalized Field Gradient $B_c'/B_c = b_c'$

(a) Magnification and Focus Field

(b) Radial and S-Distortions

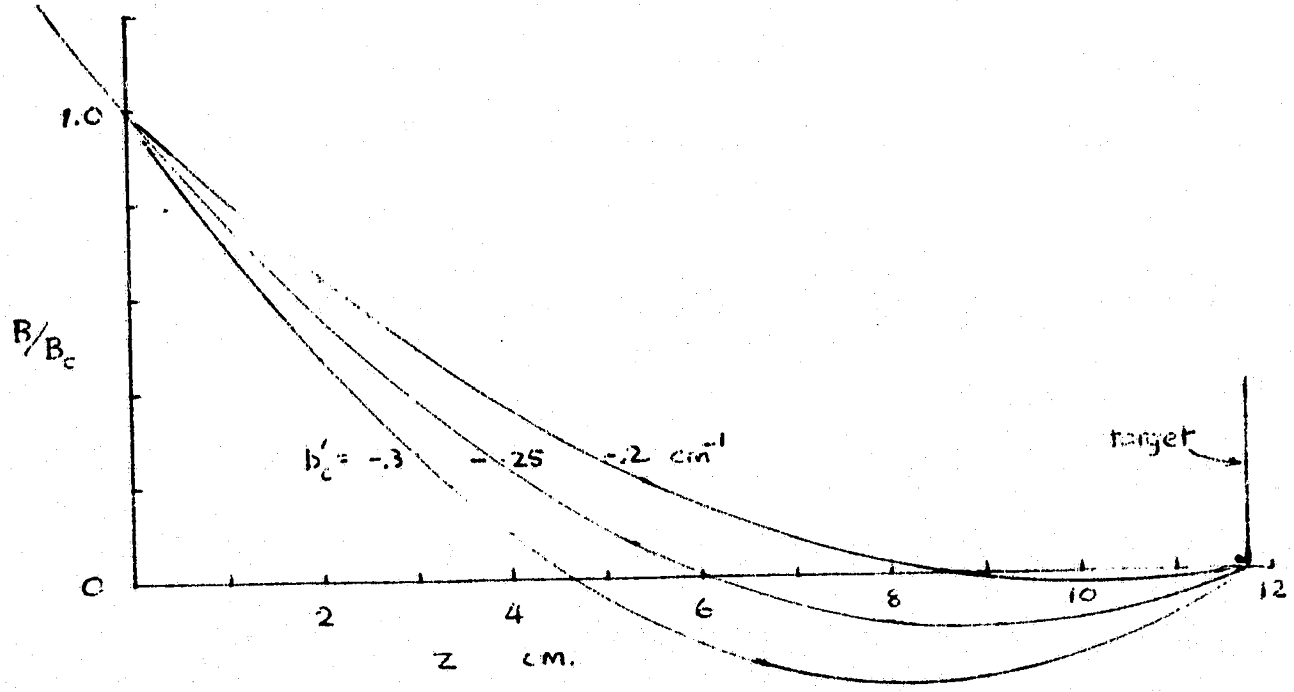

FIGURE 3.7 Parabolic B-Field Distributions for Various b_c' $(b_1 = 0)$

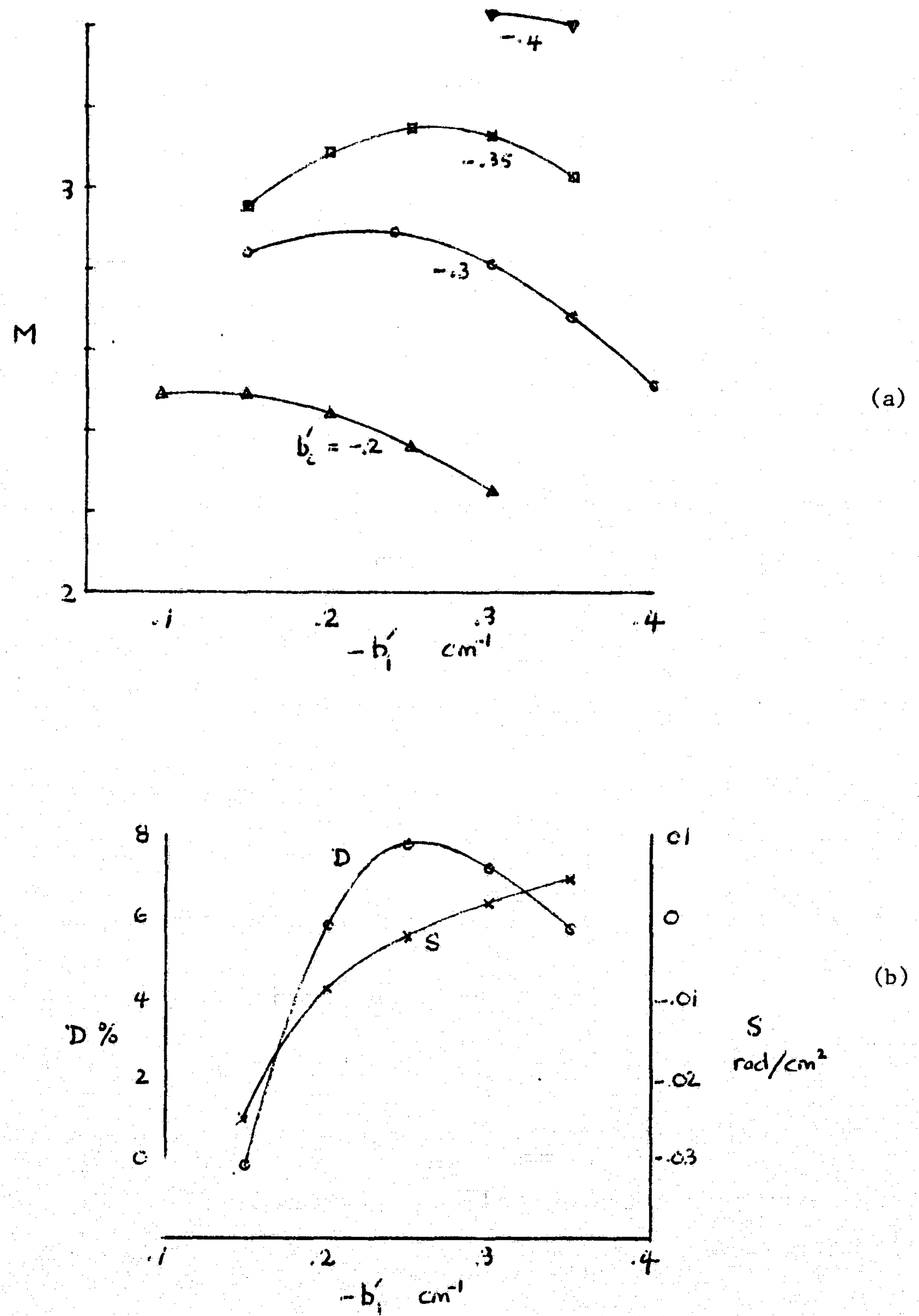

FIGURE 3.8 Cubic B-Field Distribution ($b_1 = -.75$) Performanc vs. Normalized Field Gradient $B_T'/B_c = b_1'$

(a) Magnification Curves for Various b_c'

(b) Radial and S-distortion for Case $b_c' = -.35$ cm^{-1}

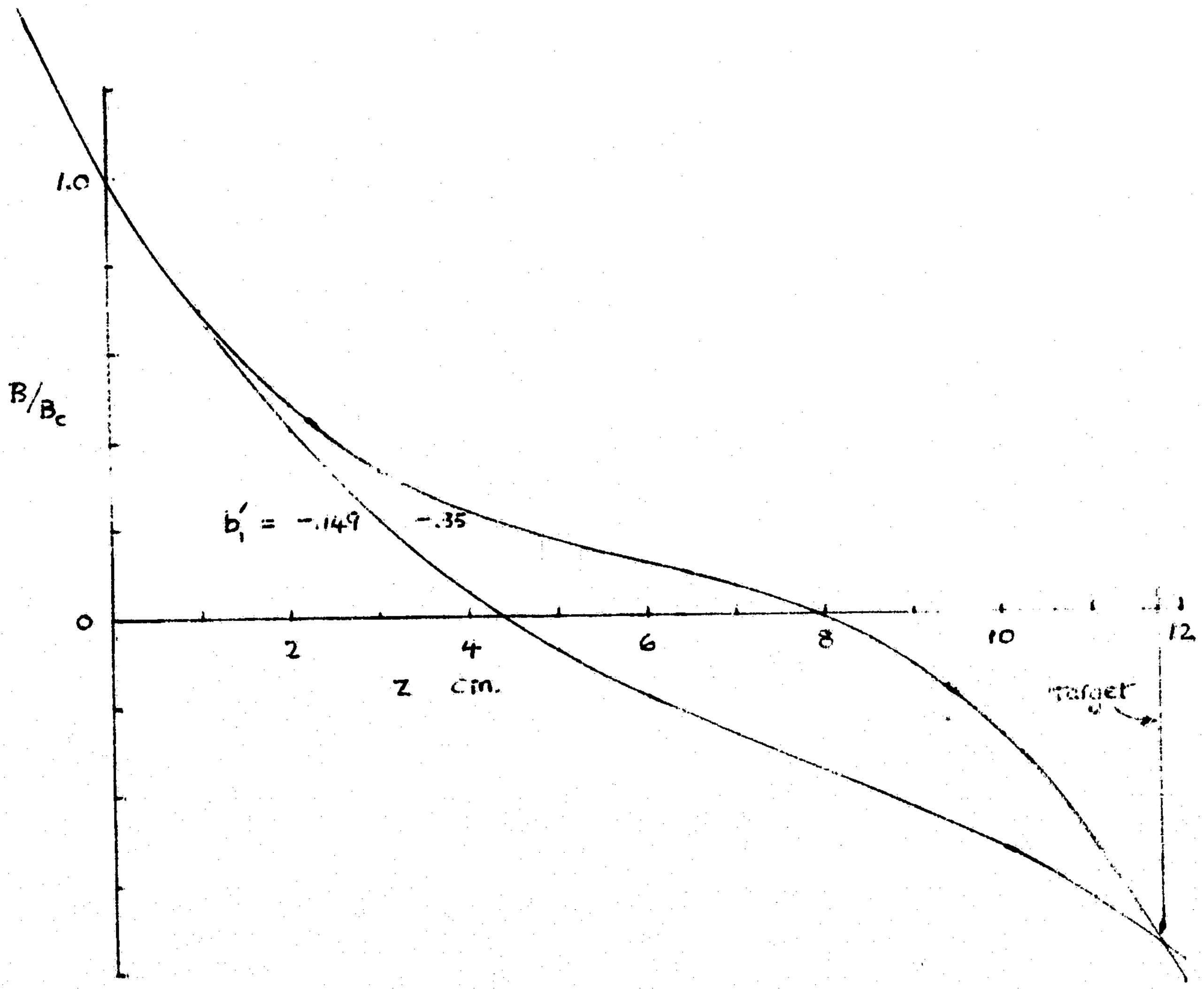

FIGURE 3.9 Cubic B-Field Distributions for Two Values of b_1'

(b_1 = -.75, b_c' = - .35 cm^{-1})

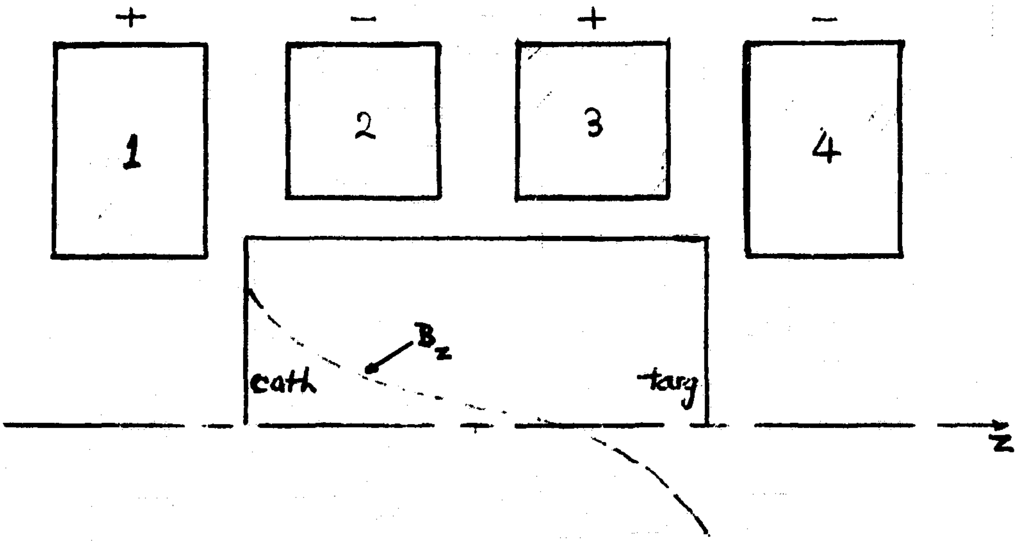

FIGURE 3.10 Schematic of Coil System to Establish Approximate Cubic B-Field Distribution

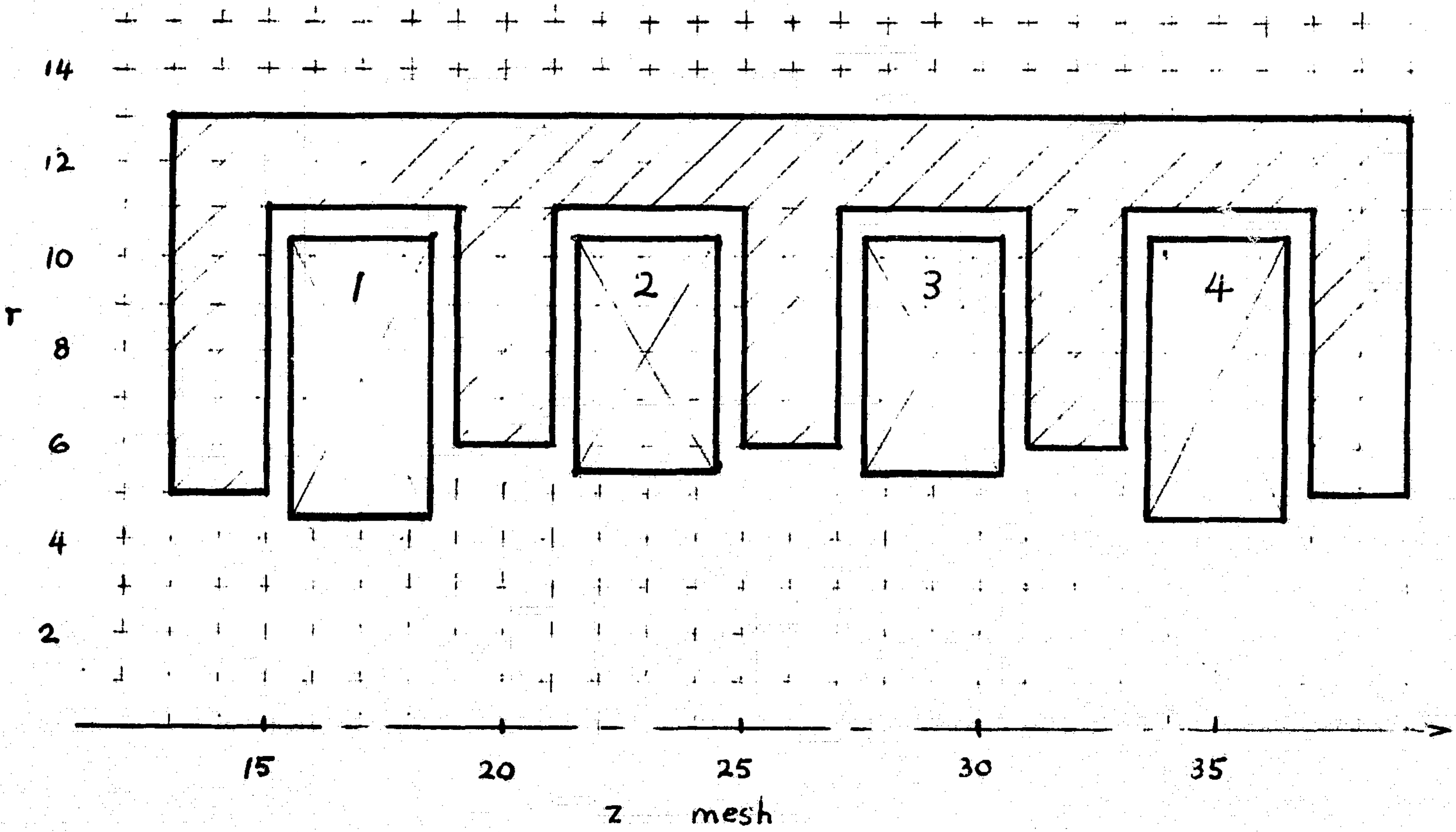

FIGURE 3.11 Computer Model of Iron-Shrouded Coil System Showing Relaxation Net

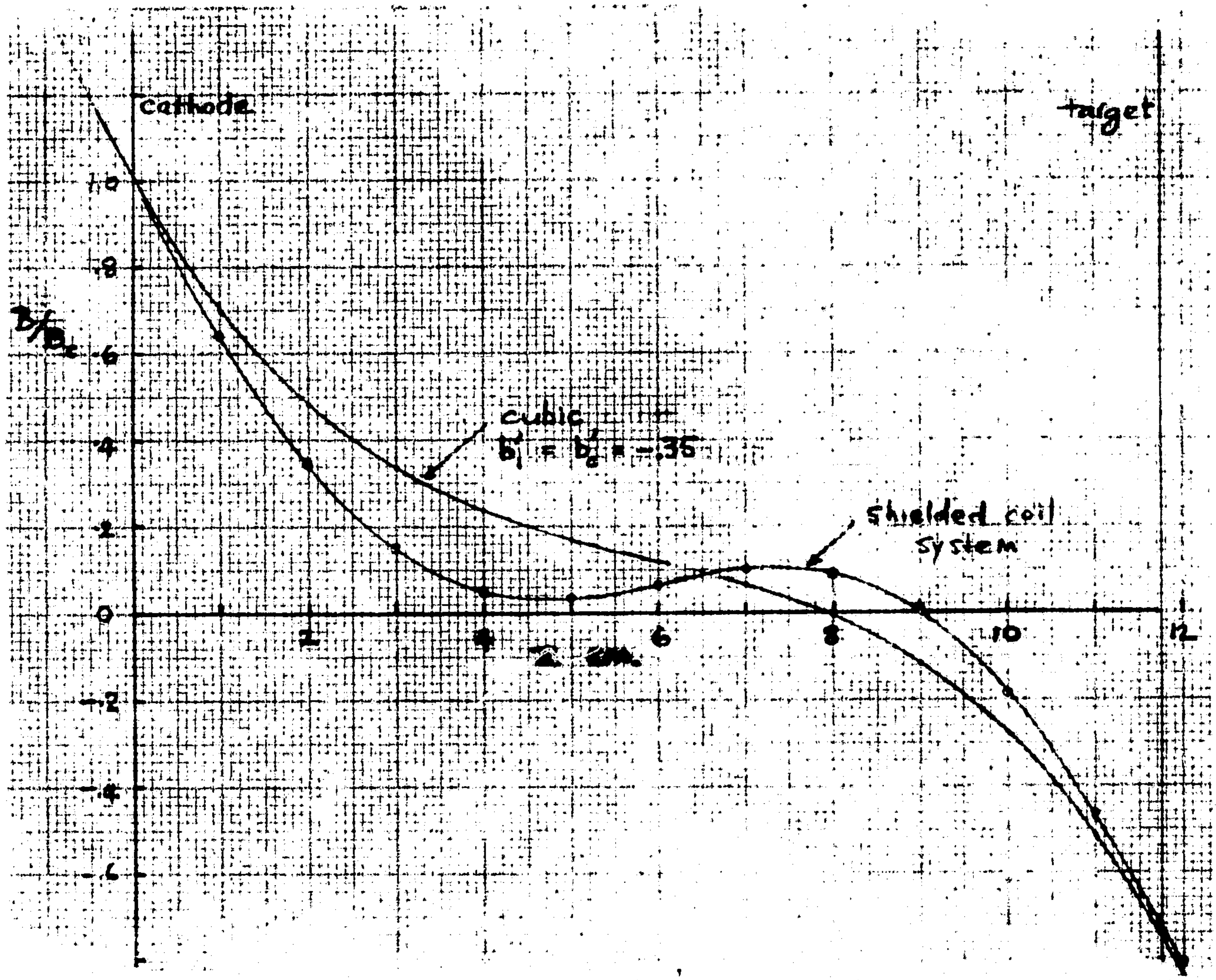

FIGURE 3.12 Field Distribution for the Coil System of Figure 3.11 Compared with Original Cubic Form

$b_1 = -.75$, $b_c' = b_1' = -.35\ \text{cm}^{-1}$

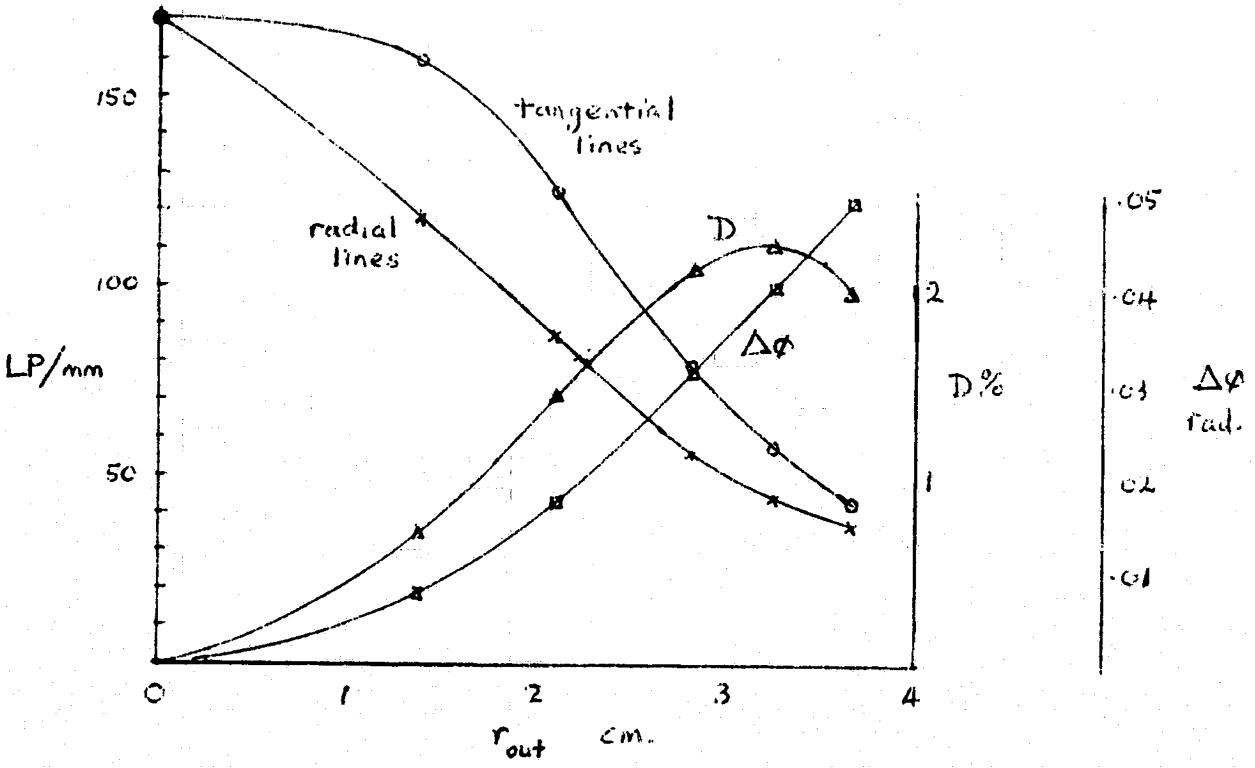

FIGURE 3.13 Performance vs. Radius for the Coil System of Figure 3.11 at 8 KV, B_c = 171 gauss.

Coil Power = 57 watts
Magnification = 3.78

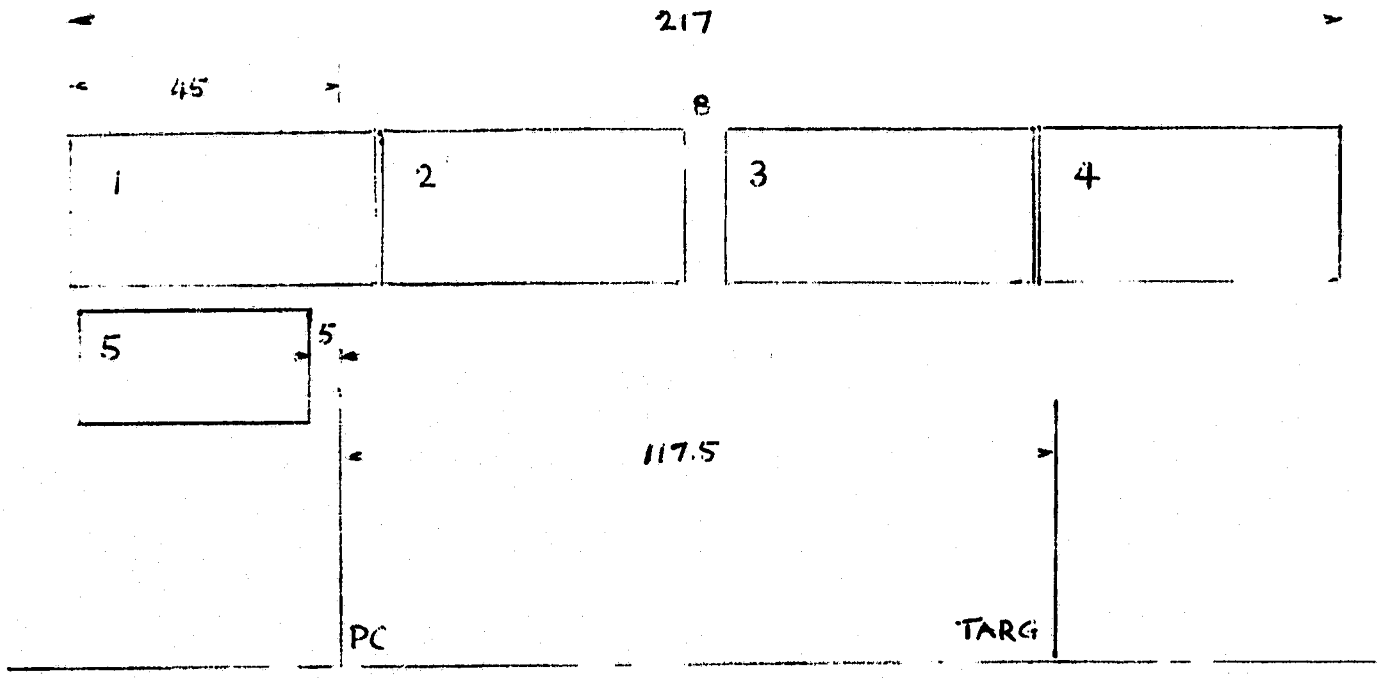

FIGURE 3.14 Coil System Details for Image Intensifier Tests Dimensions in mm.

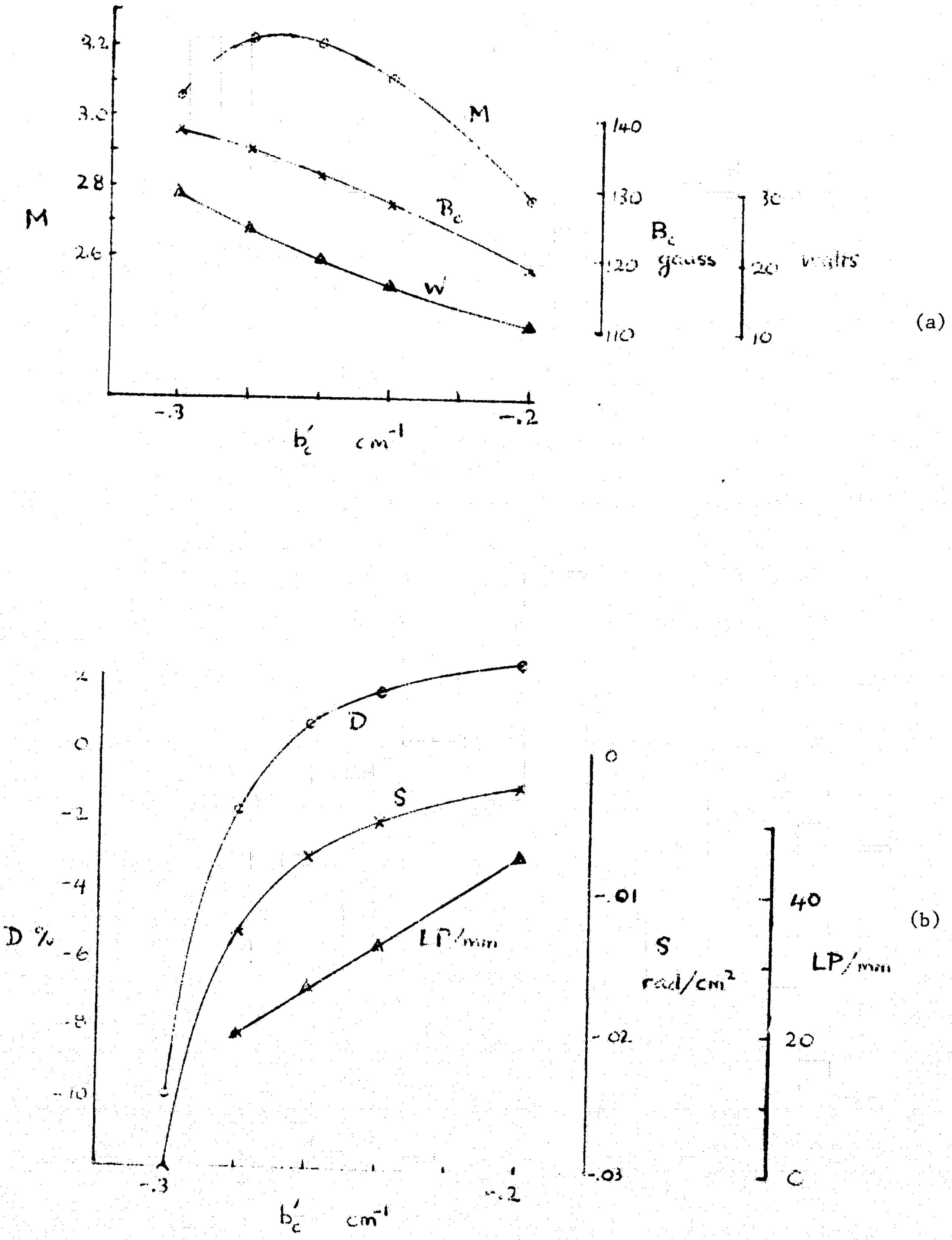

FIGURE 3.15 Performance vs. Normalized Field Gradient $B_c'/B_c = b_c'$ (6 KV operation)

(a) Magnification, Focus Field, and Power
(b) Radial and S-Distortions, and Mean Corner Resolution (referred to input)

ORIGINAL PAGE IS
OF POOR QUALITY

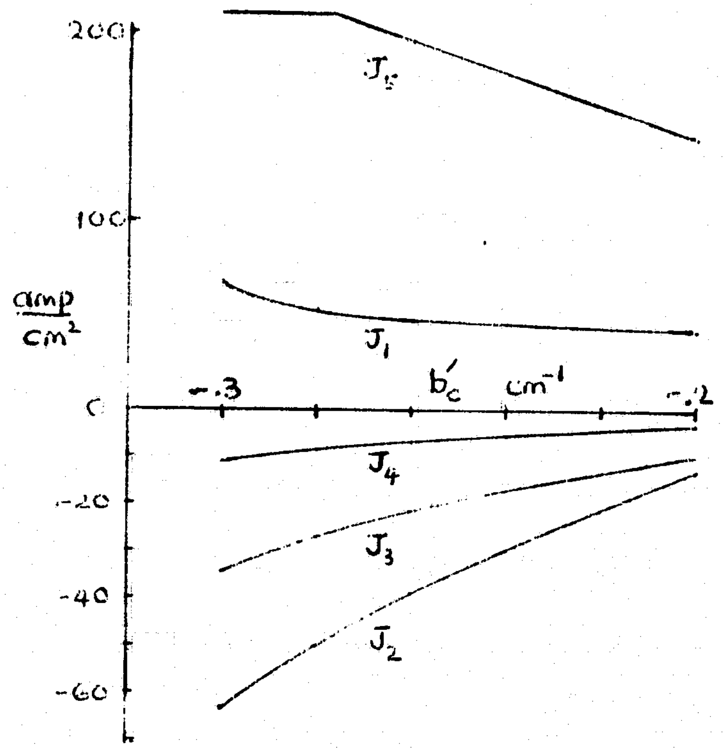

FIGURE 3.16 Coil Currents vs. Normalized Field Gradient b_c'. (6 KV)

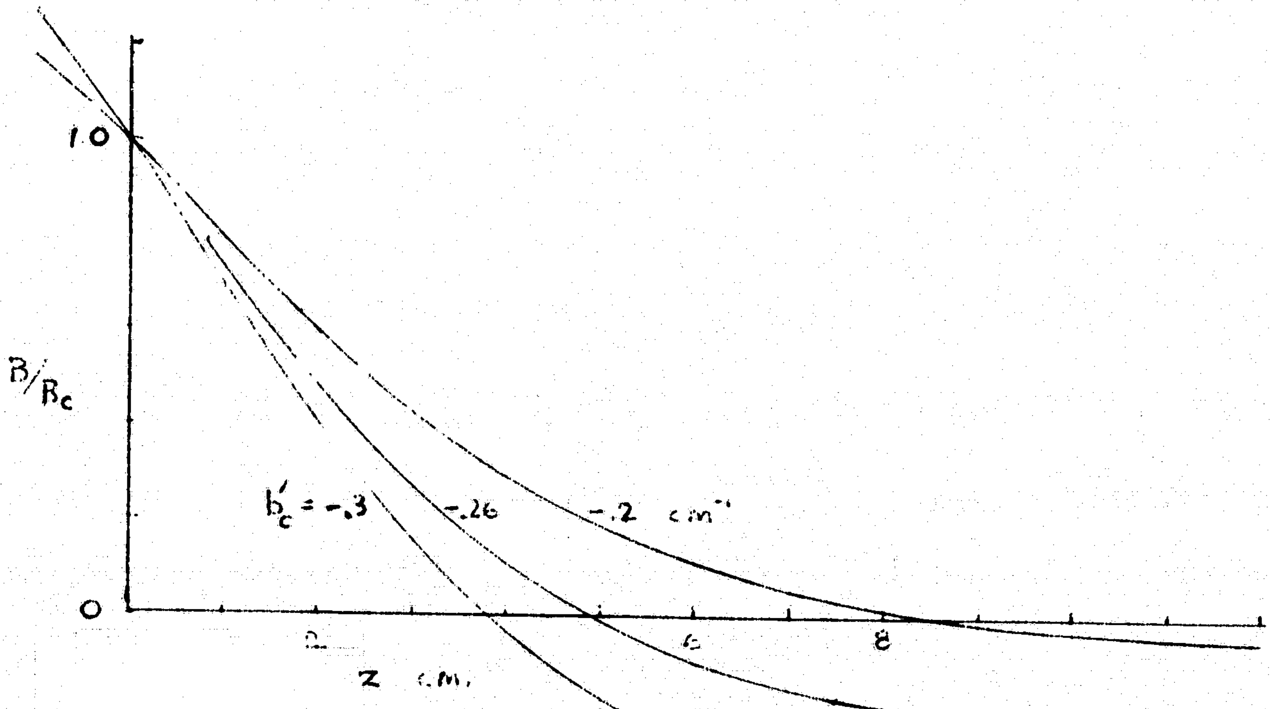

FIGURE 3.17 B-Field Distributions for Various Values of b_c'

ORIGINAL PAGE IS
OF POOR QUALITY

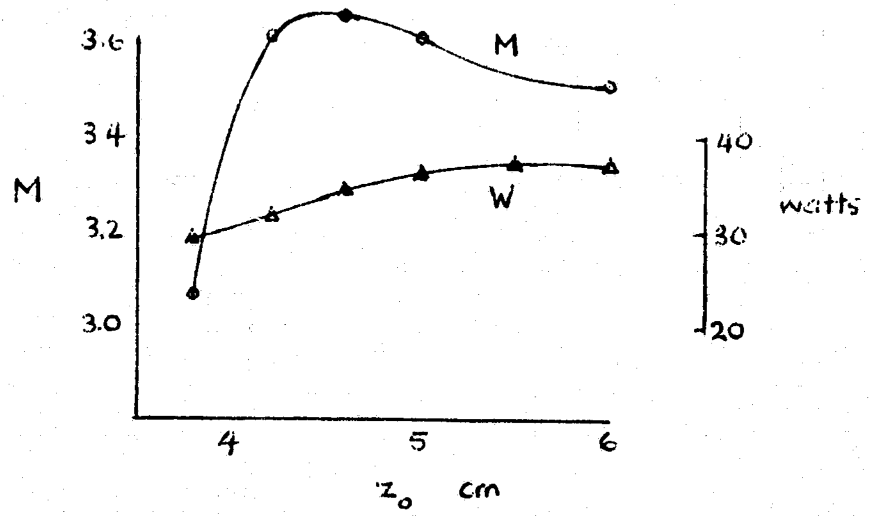

(a)

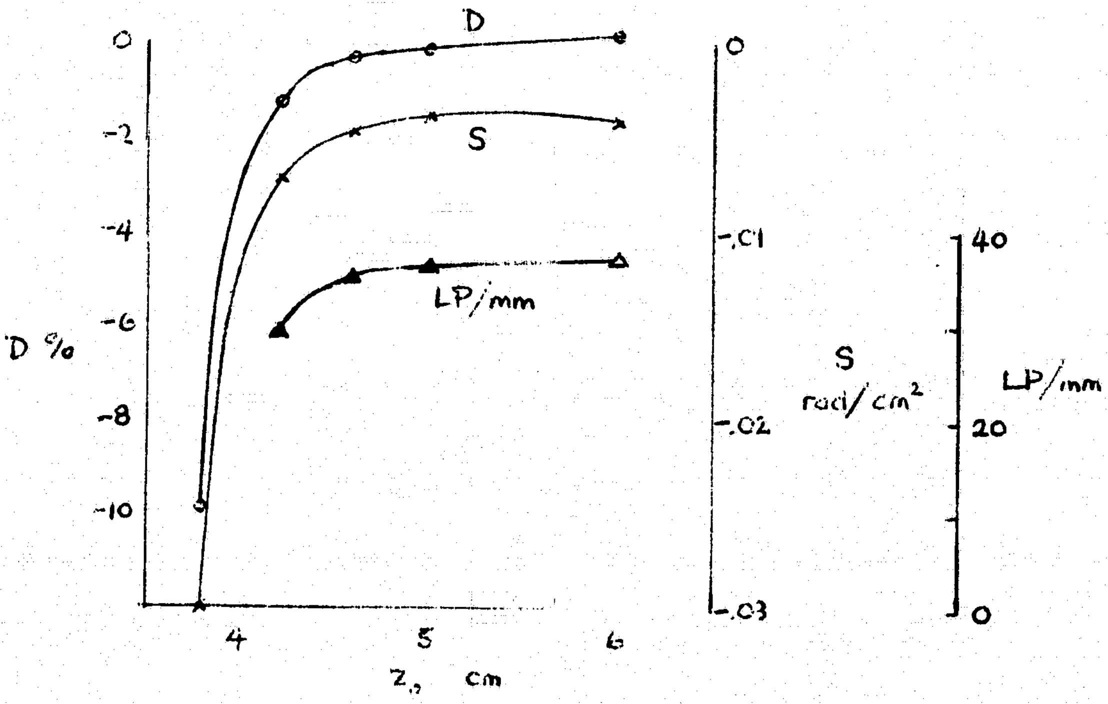

(b)

FIGURE 3.18 Performance vs. Field Reversal Coordinate z_o ($b_c' = -.3$ cm^{-1}, 6 KV)

(a) Magnification and Power
(b) Radial and S-Distortions, and Mean Corner Resolution (Referred to Input)

ORIGINAL PAGE IS
OF POOR QUALITY

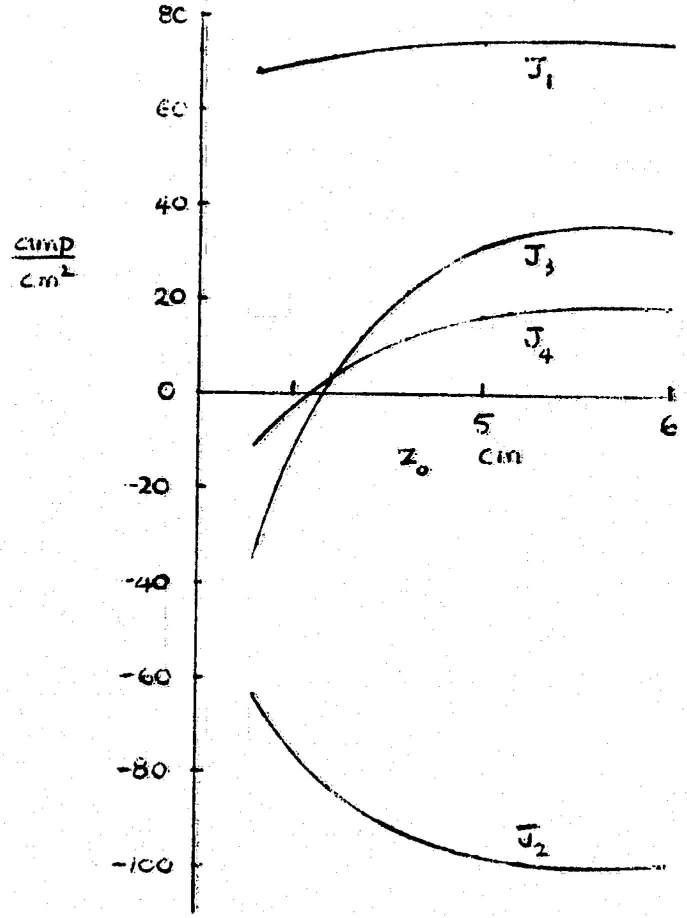

FIGURE 3.19 Coil Currents vs. Field Reversal Coordinate z_o

($b_c' = -.3\ \text{cm}^{-1}$, 6 KV)

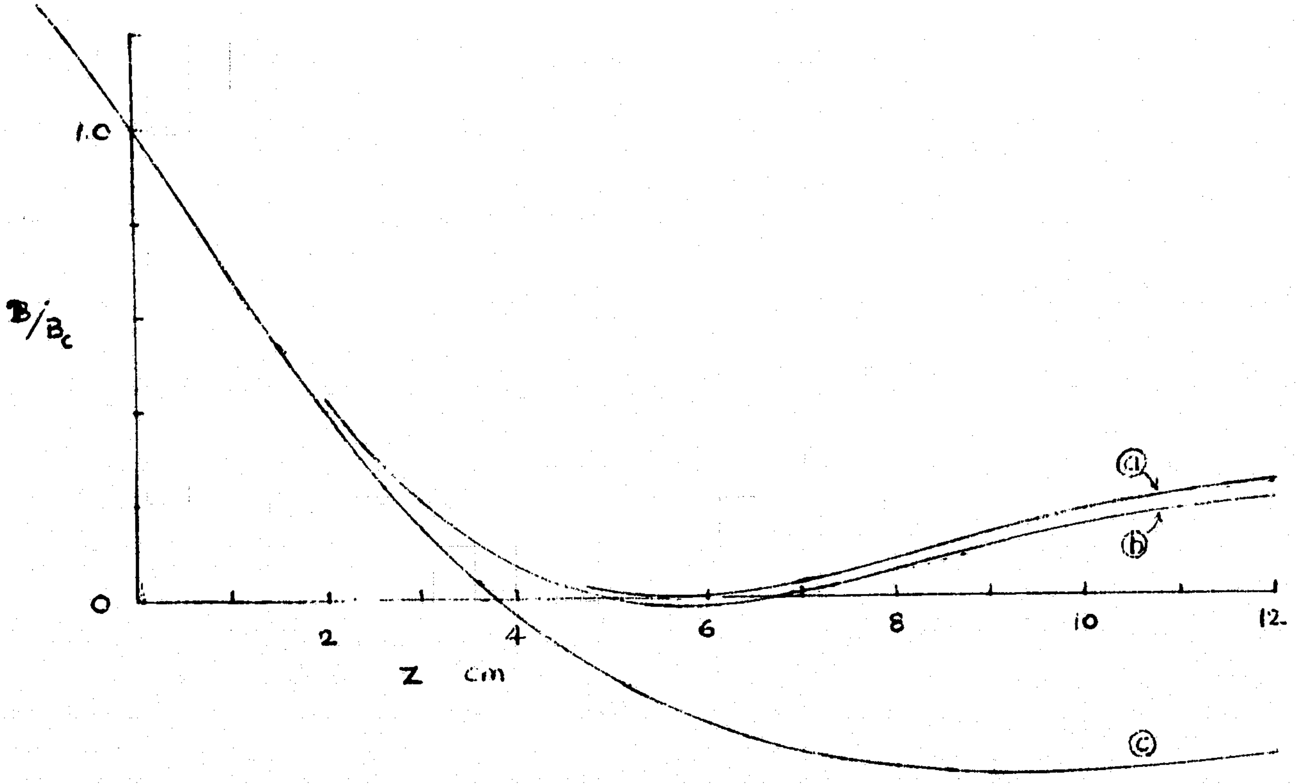

FIGURE 3.20 B-Field Distributions for $b_c' = -.3\ \text{cm}^{-1}$

(a) $z_o = 5.6$ cm, (b) $z_o = 5$ cm, (c) $z_o = 3.8$ cm

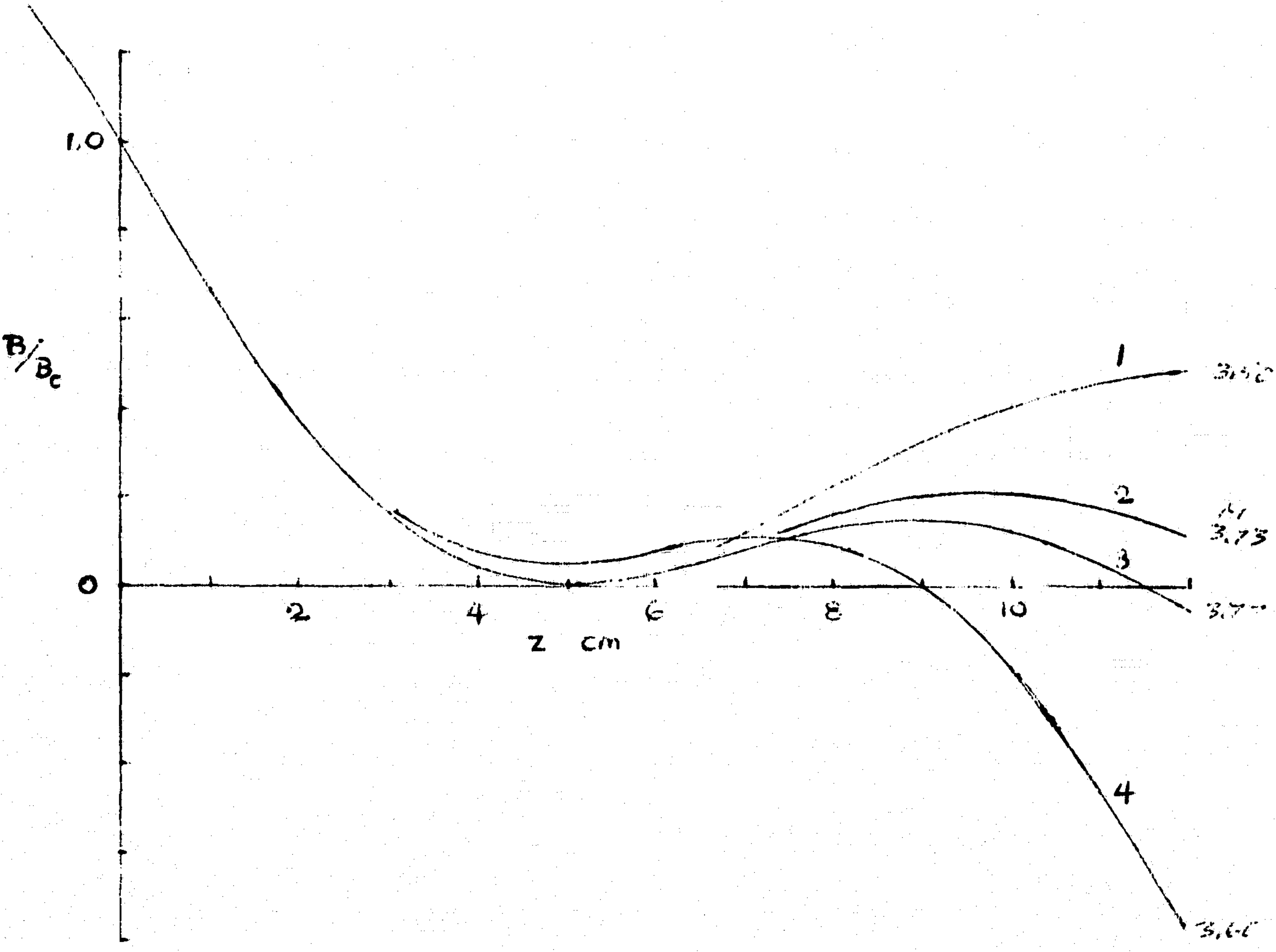

FIGURE 3.21 B-Field Distributions for $b_c' = -.33\ \text{cm}^{-1}$

(1) $z_o = 5$ cm
(2) $z_o = 5$ cm, $J_4 = -60\ \text{amp/cm}^2$
(3) $z_o = 5$ cm, $J_4 = -100\ \text{amp/cm}^2$
(4) $b_T = -.7$, $b_T' = -.33\ \text{cm}^{-1}$

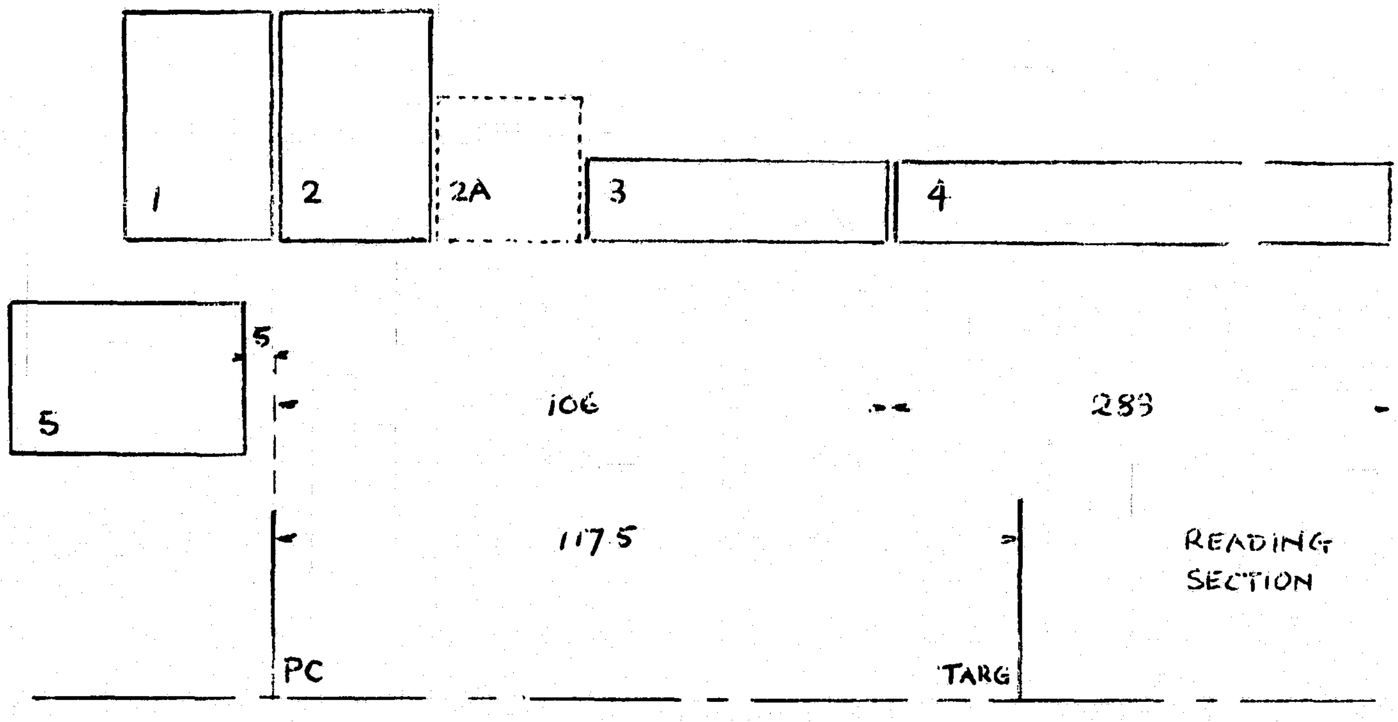

FIGURE 3.22 Coil System Details for Camera Tube Test Study - Dimensions in mm.

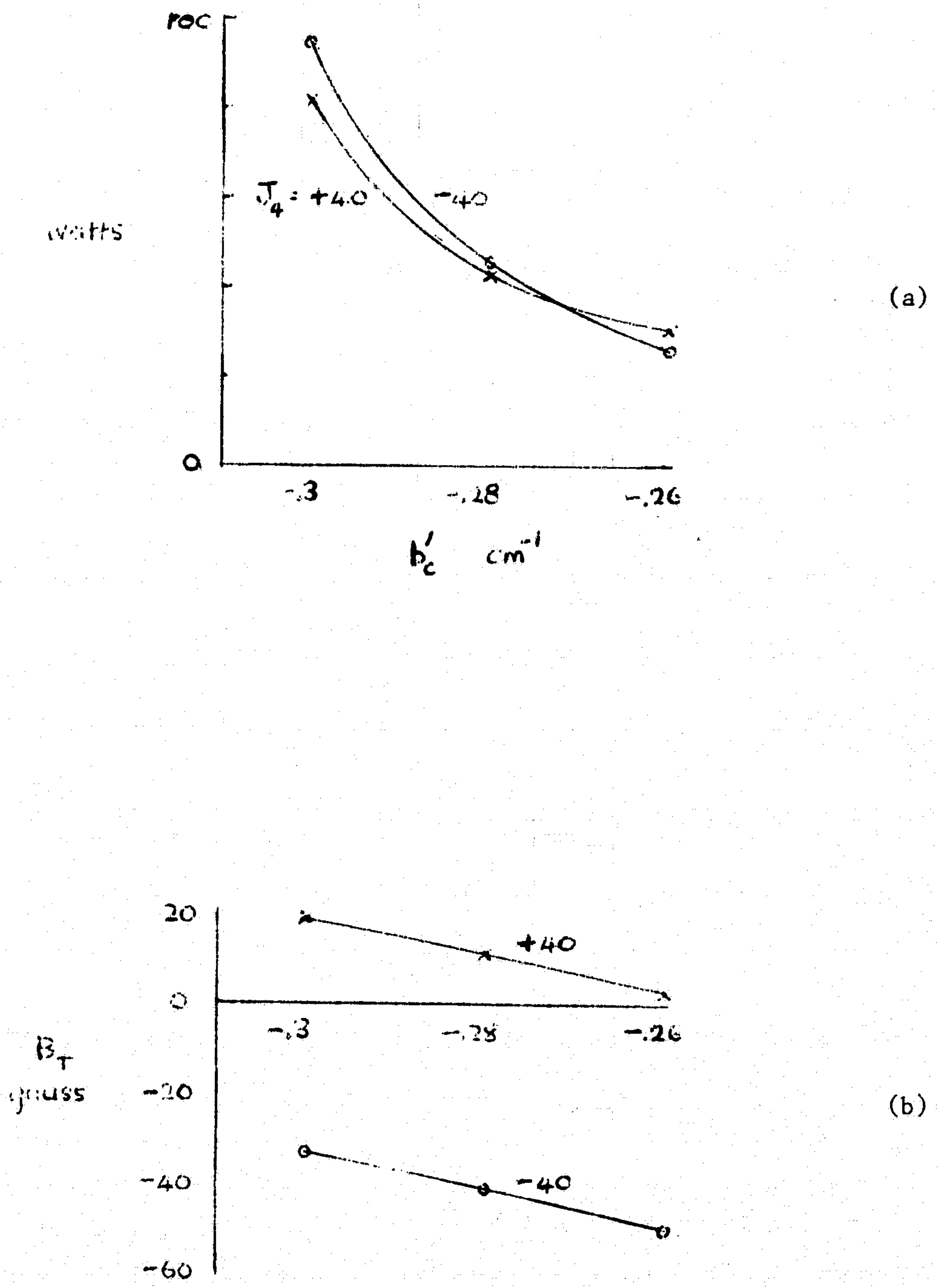

FIGURE 3.23 (a) Power vs. Normalized Field Gradient b_c' for Two Values of J_4

(b) Field Strength at the Target vs. b_c'

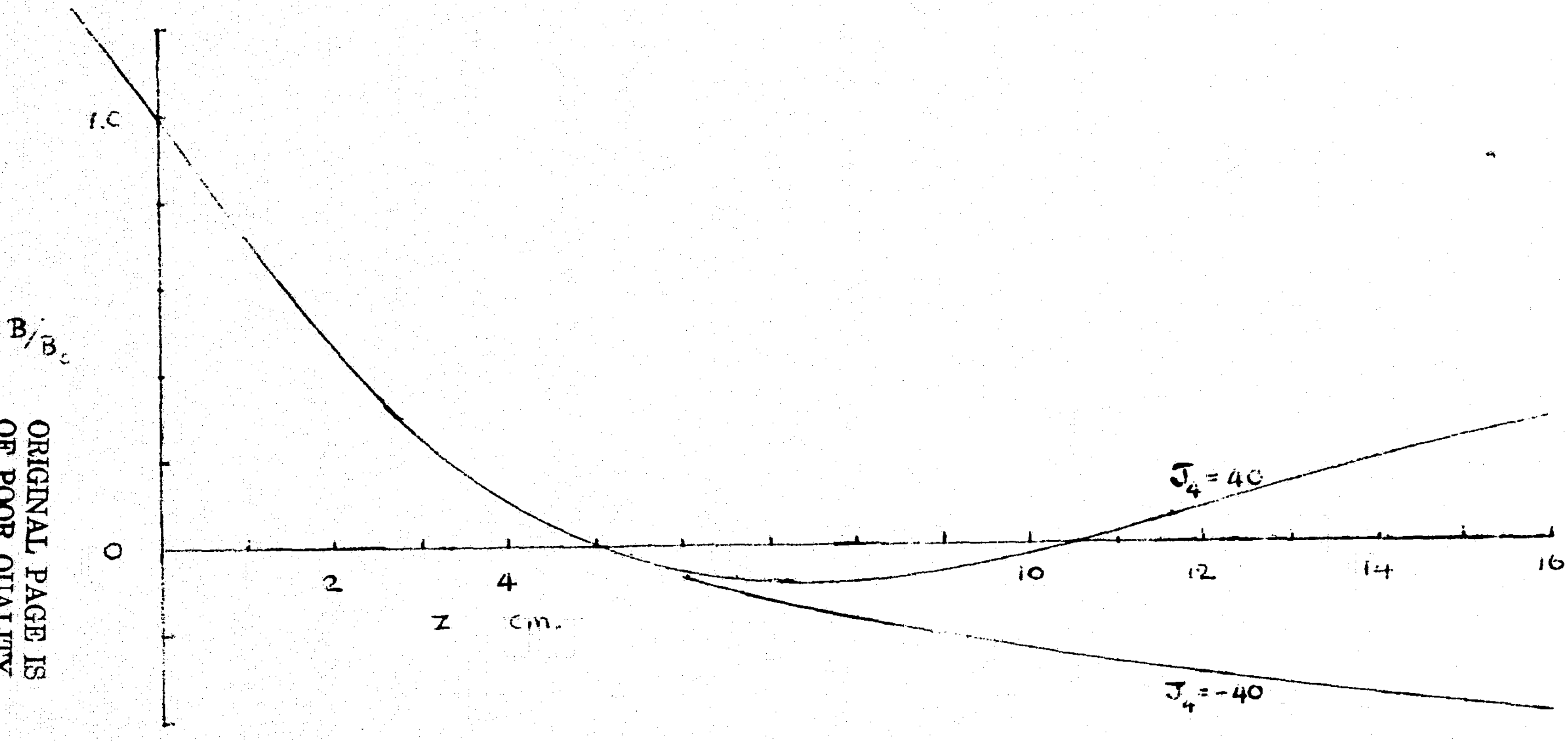

FIGURE 3.24 B-Field Distributions for $b_c' = -.28$, $J_4 = \pm 40$ amp/cm^2

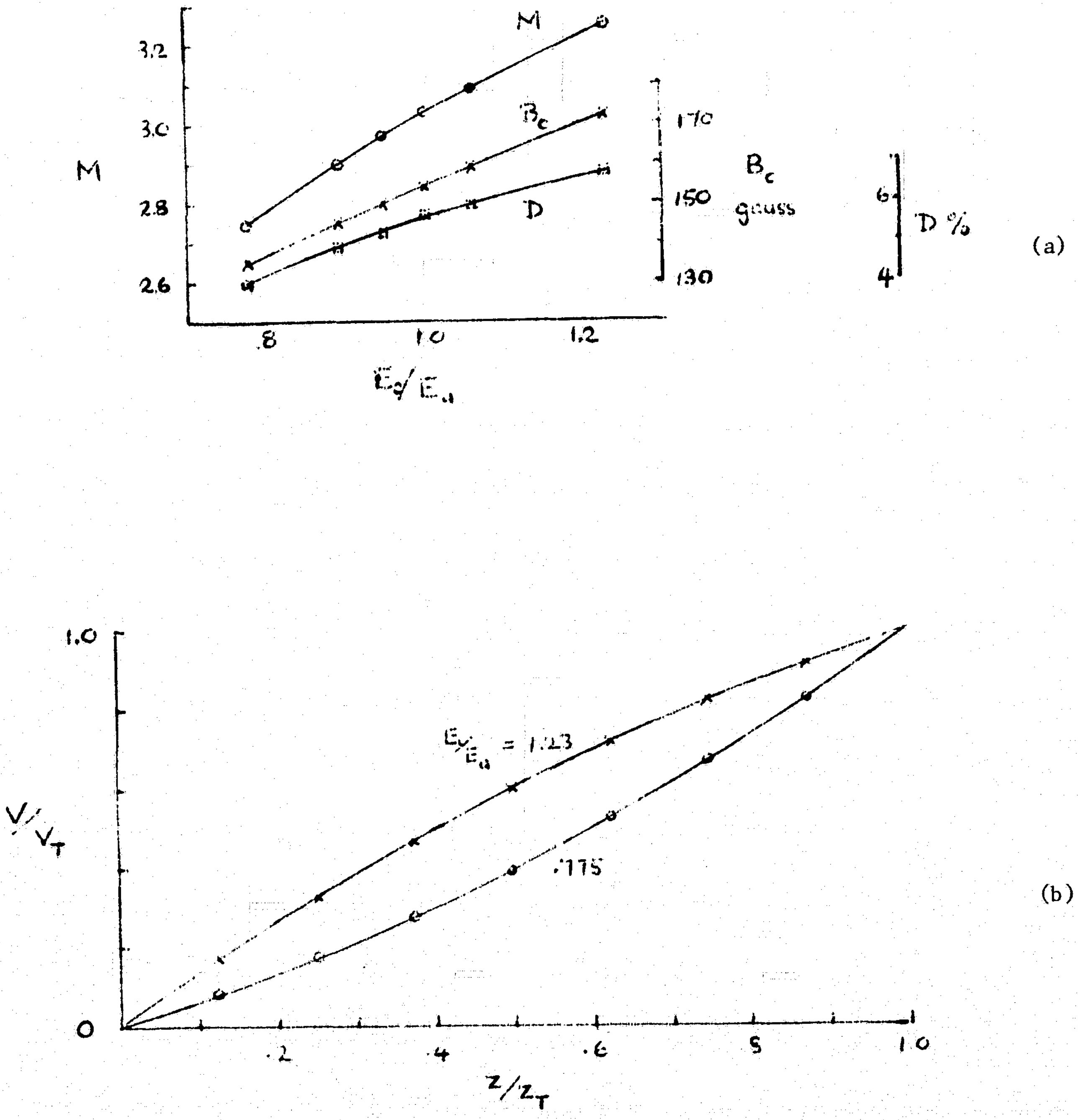

FIGURE 3.25 Non-Uniform E-Field (B-Field Distribution as Figure 3.9, $b_1' = -.35$)

(a) Performance vs. Cathode Field Strength (8 KV)

(b) E-Field Distributions for the Extreme Cases

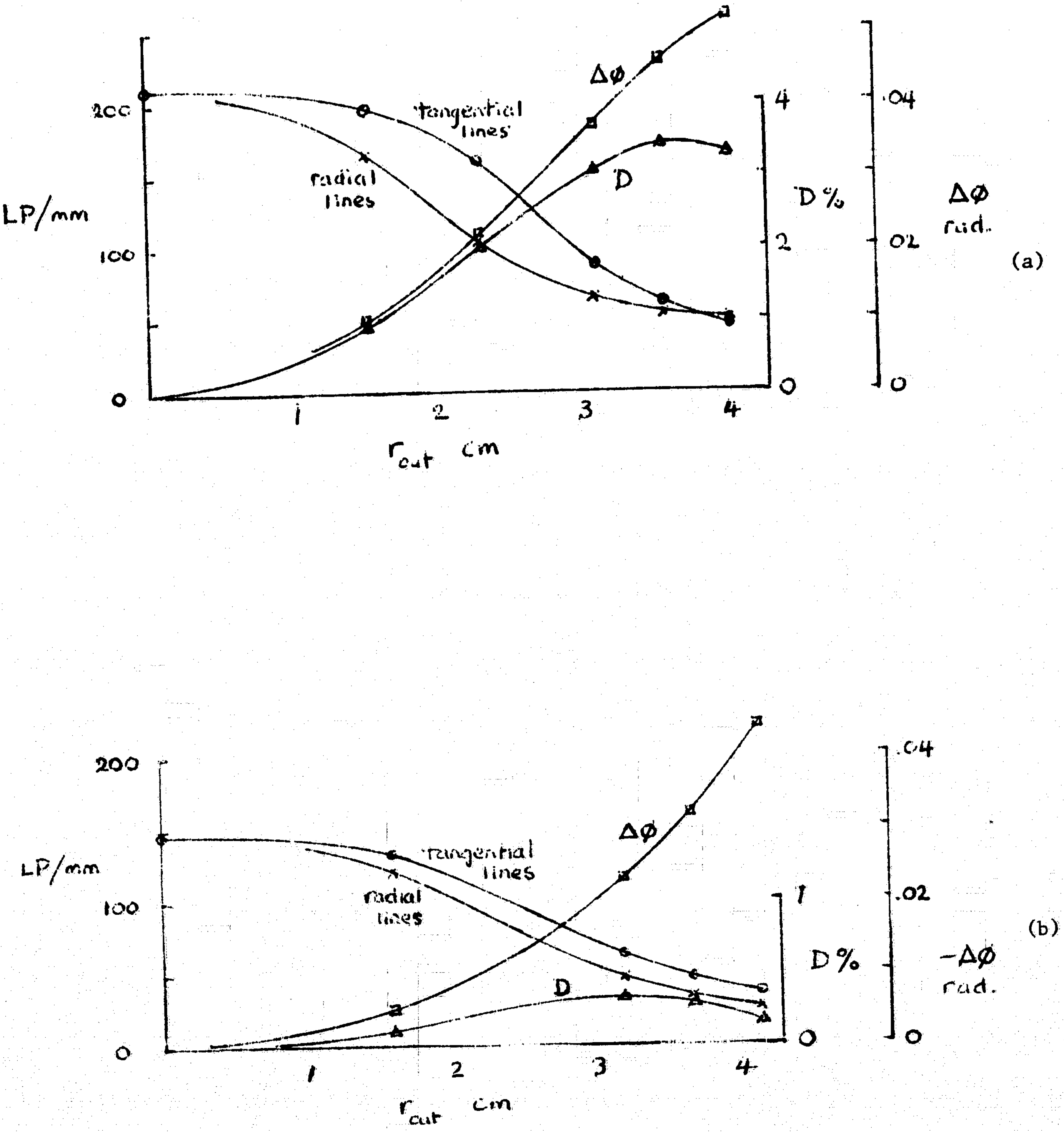

FIGURE 3.26 Non-Uniform E-Field $E_c/E_u = 1.23$

(a) B-Field of Figure 3.12. 8KV. M = 4.08

(b) B-Field (b) of Figure 3.20. 6 KV. M = 3.99

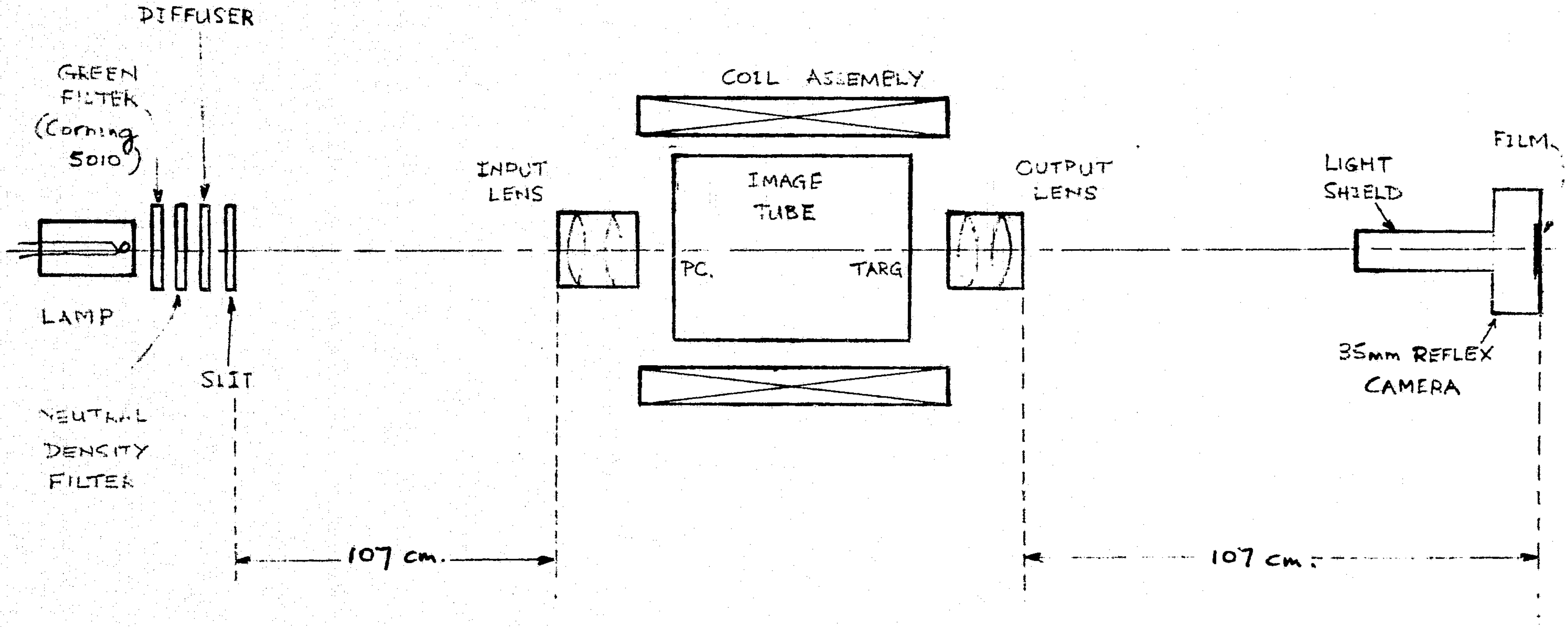

FIGURE 4.1 Image Intensifier Test Arrangement - Schematic

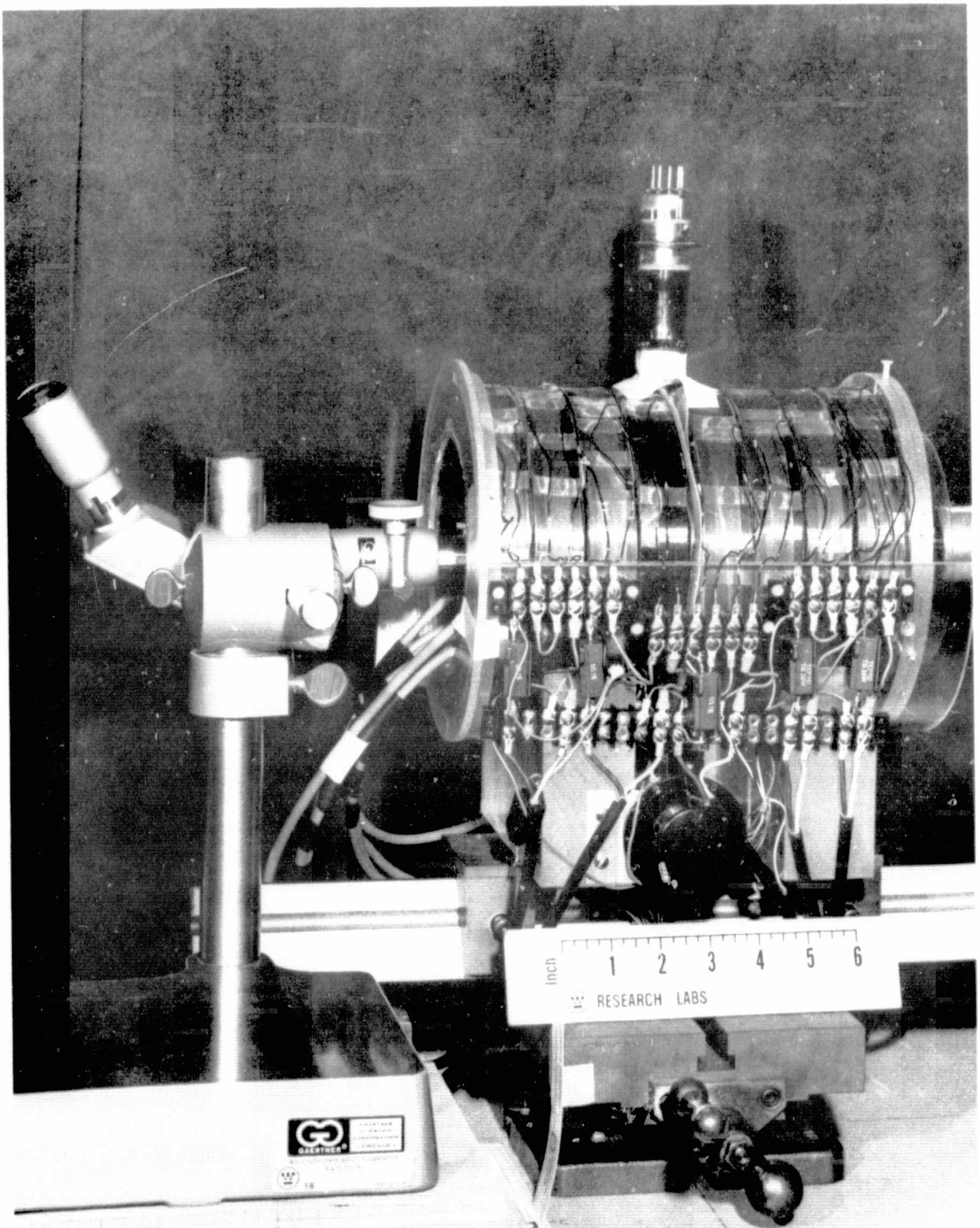

FIGURE 4.2 Image Intensifier Test Arrangement - Side View

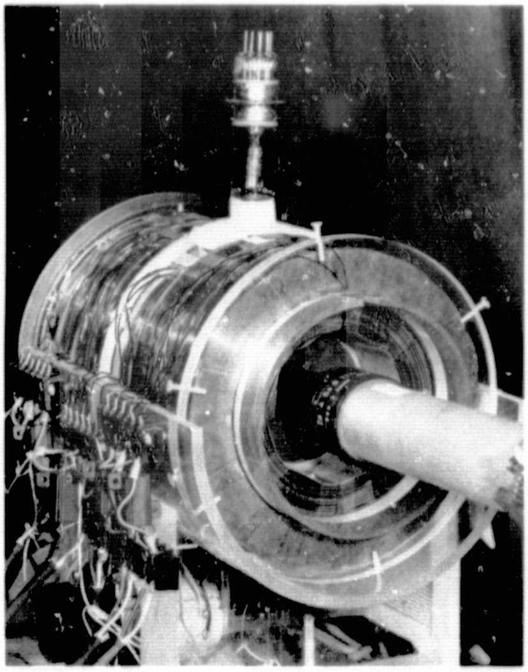

FIGURE 4.3 Image Intensifier Test Arrangement - Input End

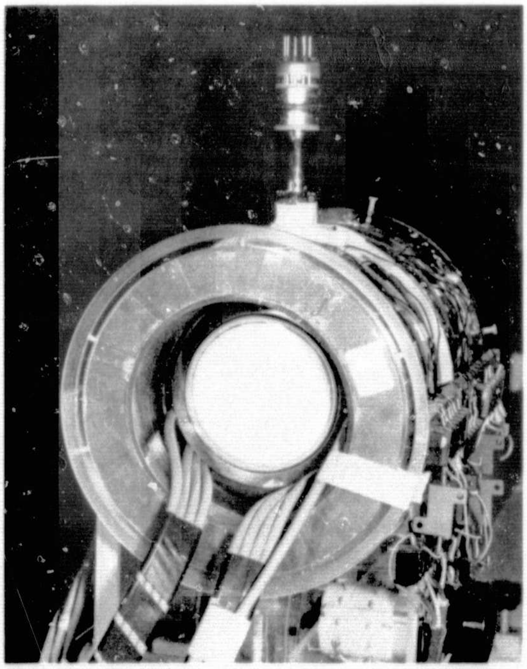

FIGURE 4.4 Image Intensifier Test Arrangement - Output End

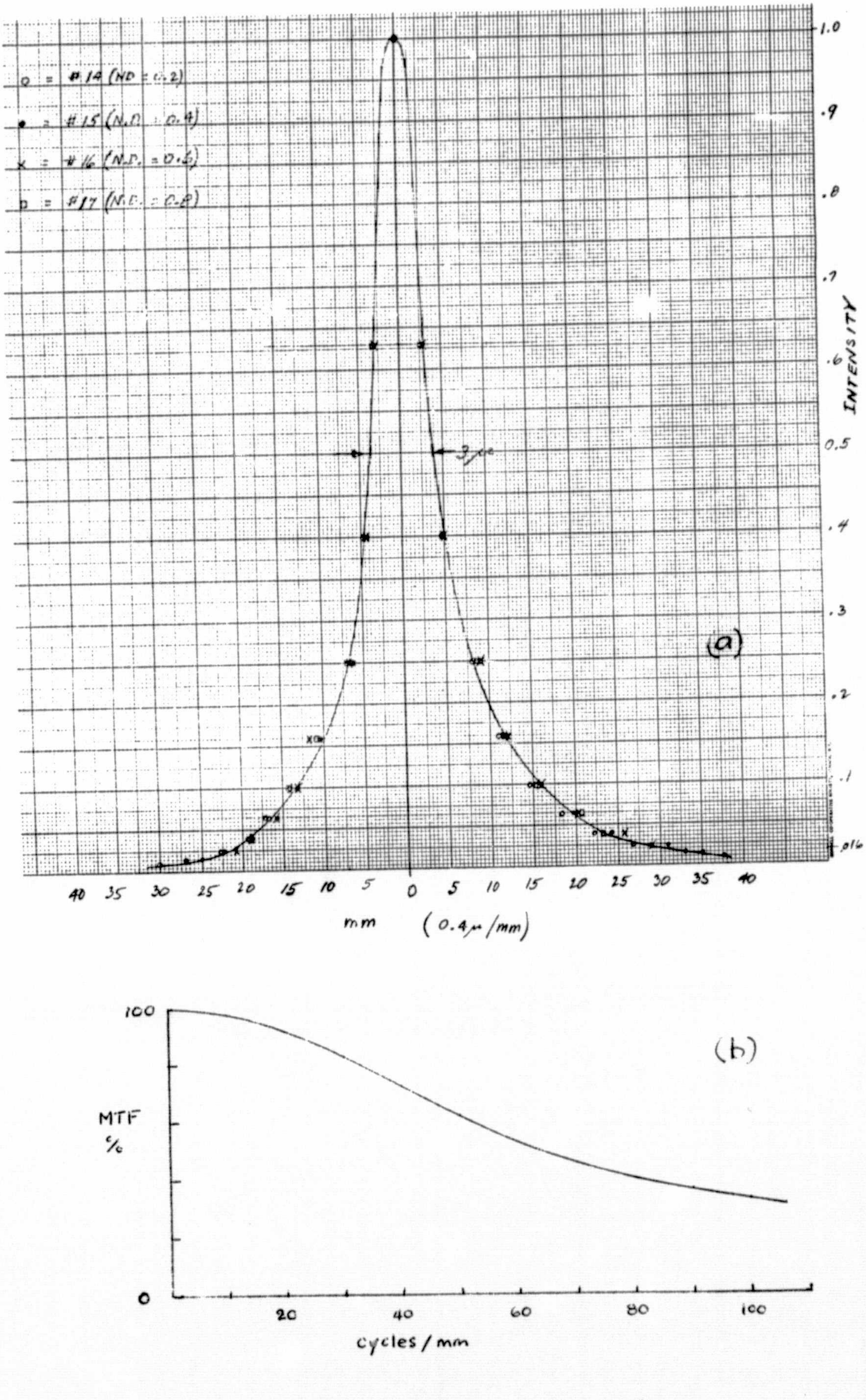

FIGURE 4.5 Optics Calibration Results

(a) Line-Spread Function
(b) Sine-Wave MTF

ORIGINAL PAGE IS
OF POOR QUALITY

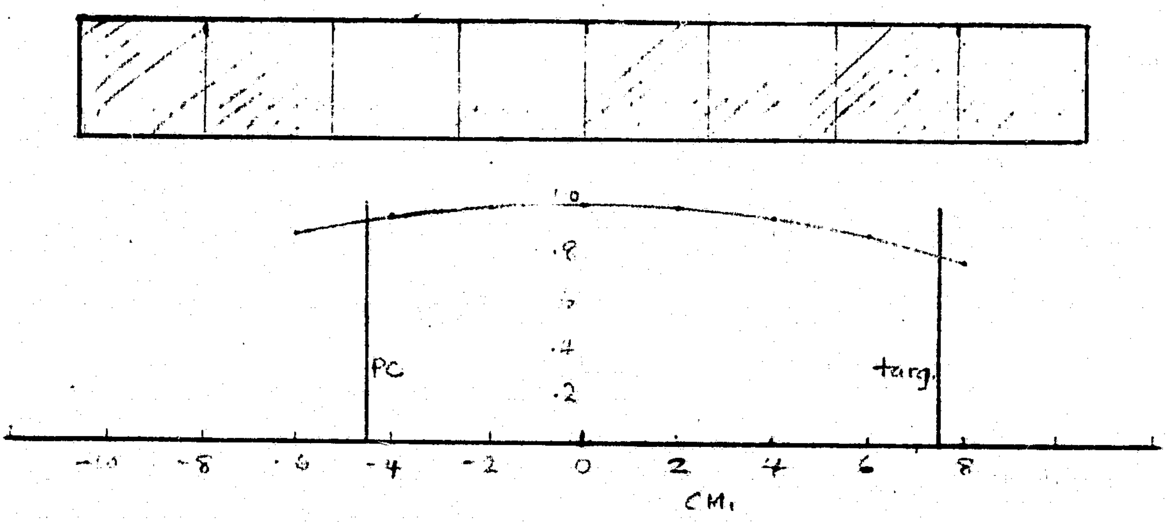

FIGURE 4.6 Location of IT #1 in the Test Coil System, and B-Field Distribution for Standard Mode

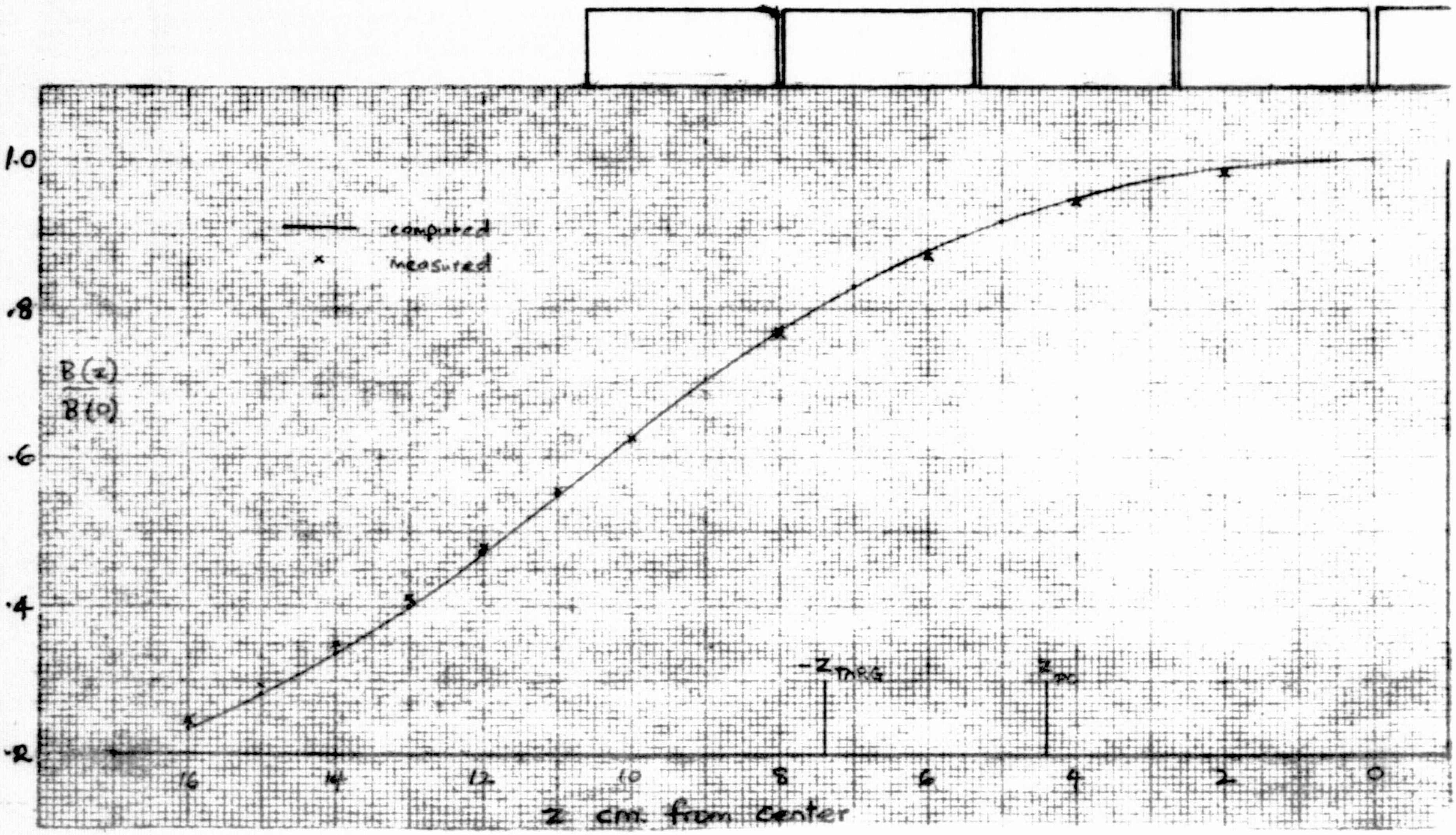

FIGURE 4.7 Comparison of Measured and Computed B-Field in Stanard Mode (Without Tube)

ORIGINAL PAGE IS
OF POOR QUALITY

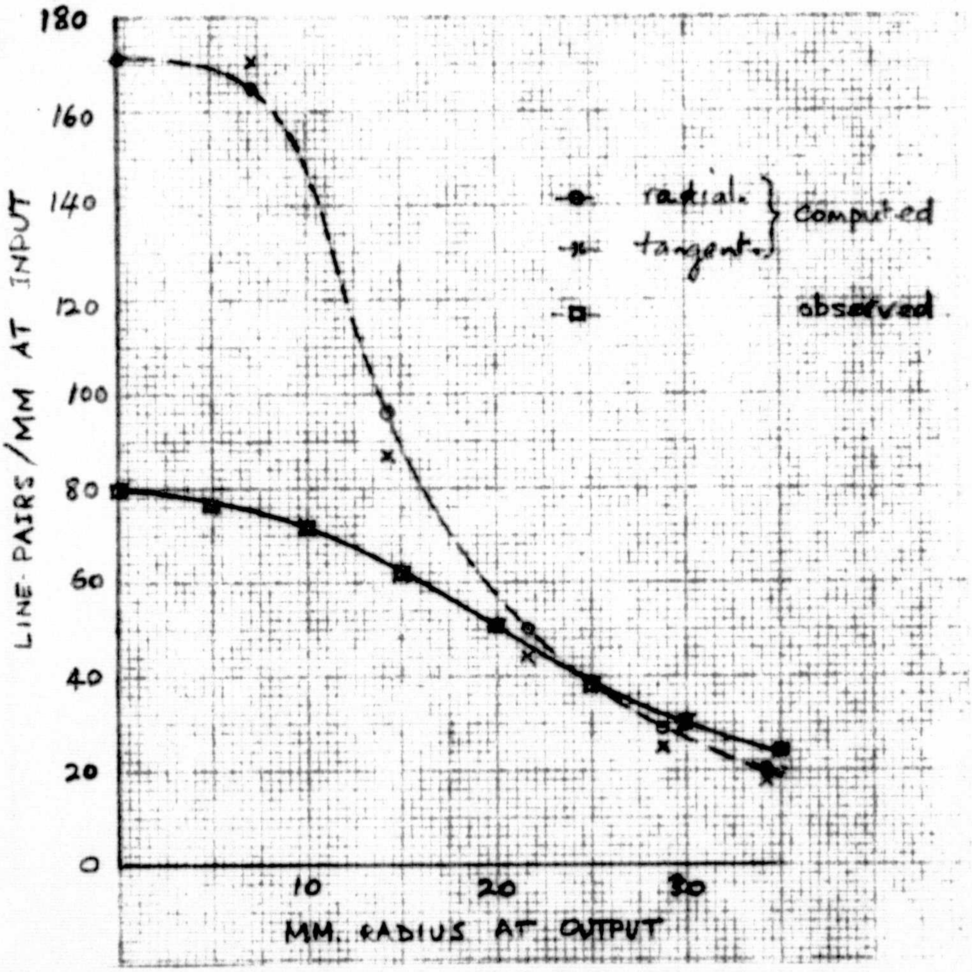

FIGURE 4.8 IT #1 Standard Mode Limiting Resolution (8 KV Operation)

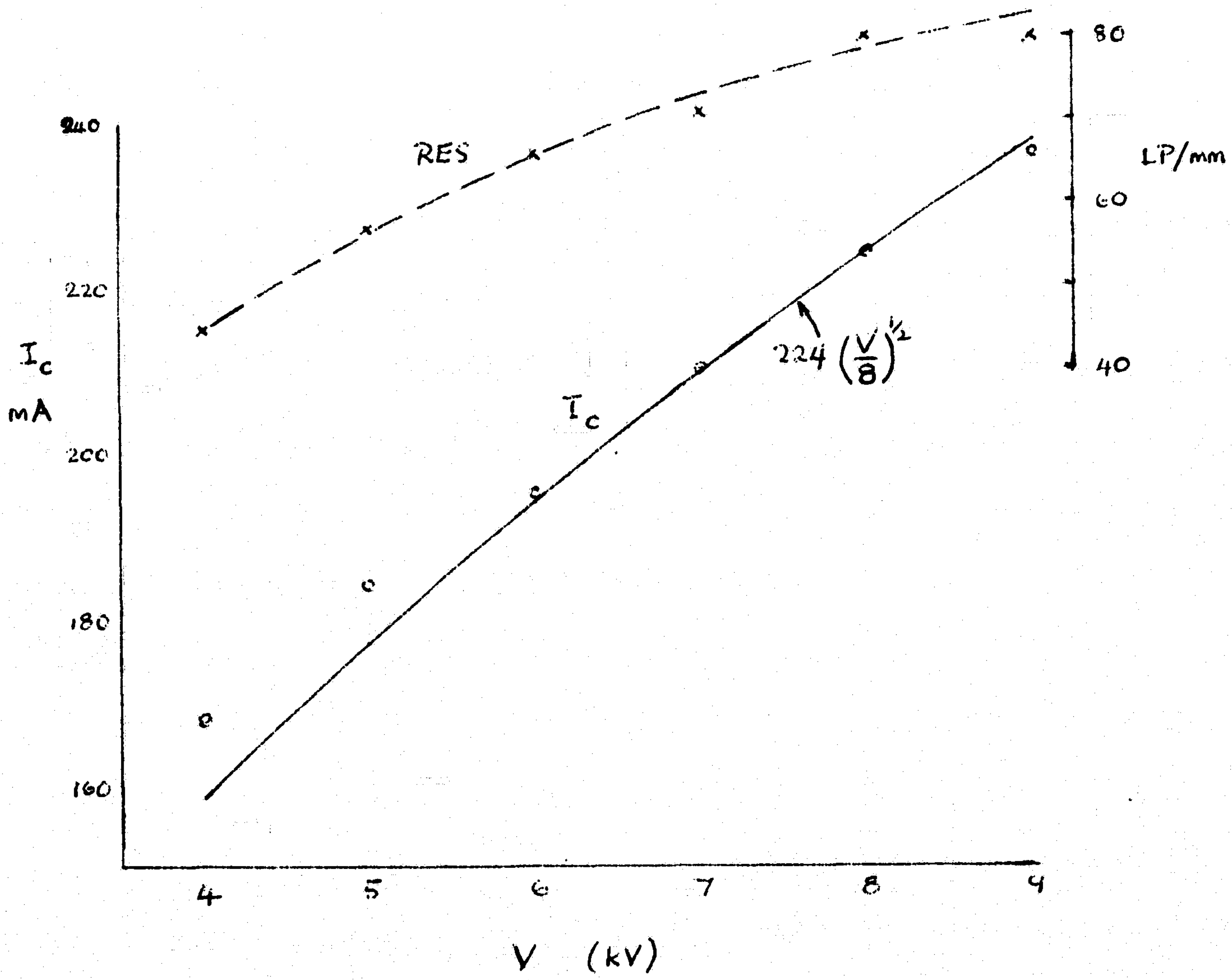

FIGURE 4.9 IT #1 Standard Mode. Focus Current and Center Limiting Resolution vs. Operating Voltage

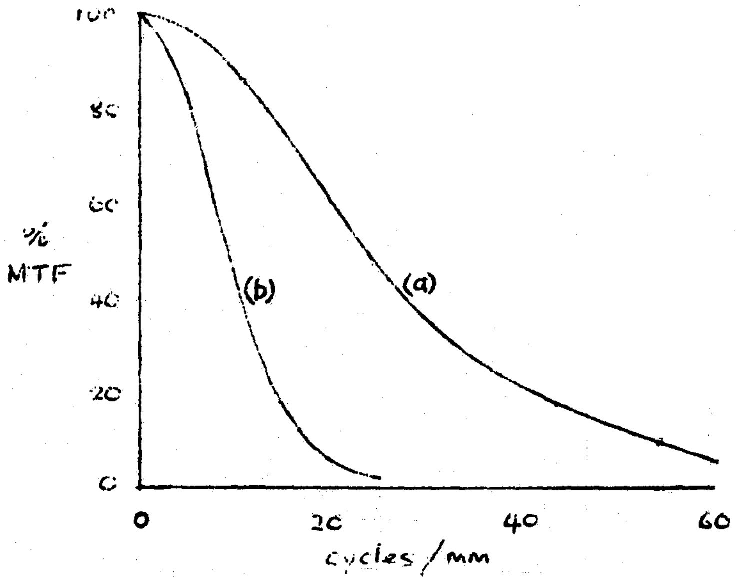

FIGURE 4.10 IT #1 Standard Mode (8 KV). Sine-Wave MTF Measurements

(a) Center
(b) 2.5 cm Radius (Tangential)

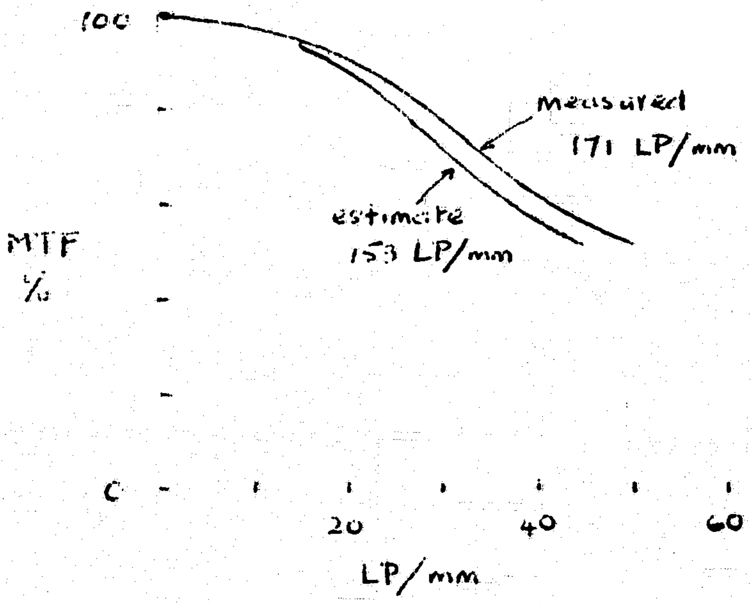

FIGURE 4.11 Square-Wave MTF Curves for Phosphor Screens

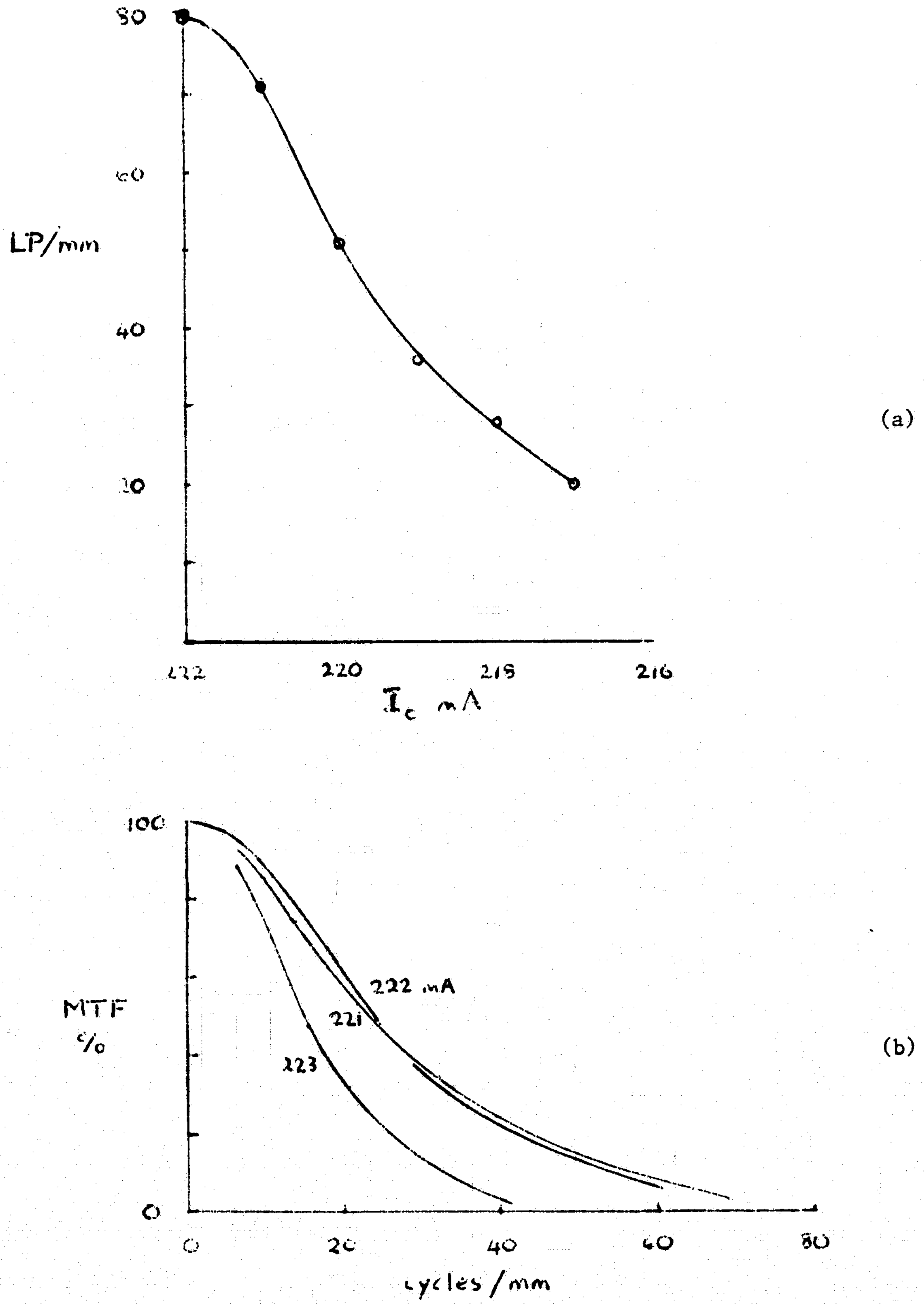

FIGURE 4.12 IT #1 Resolution Loss with Defocusing (8 KV)

(a) Center Limiting Resolution vs Coil Current
(b) Sine-Wave MTF Curves at 3 Coil Currents

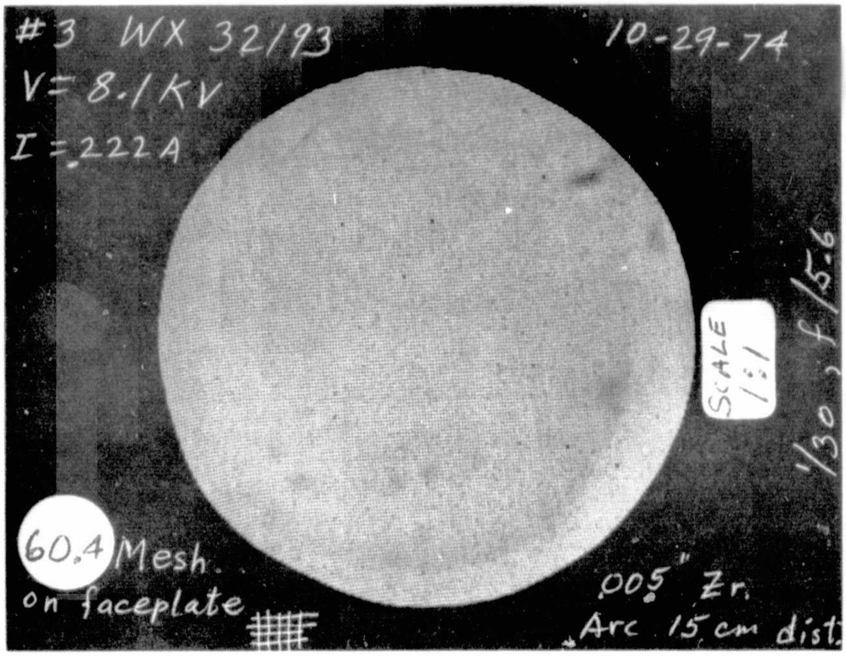

FIGURE 4.13 IT #3 Standard Mode Image of a 60 Line/Inch Mesh (M = 0.96)

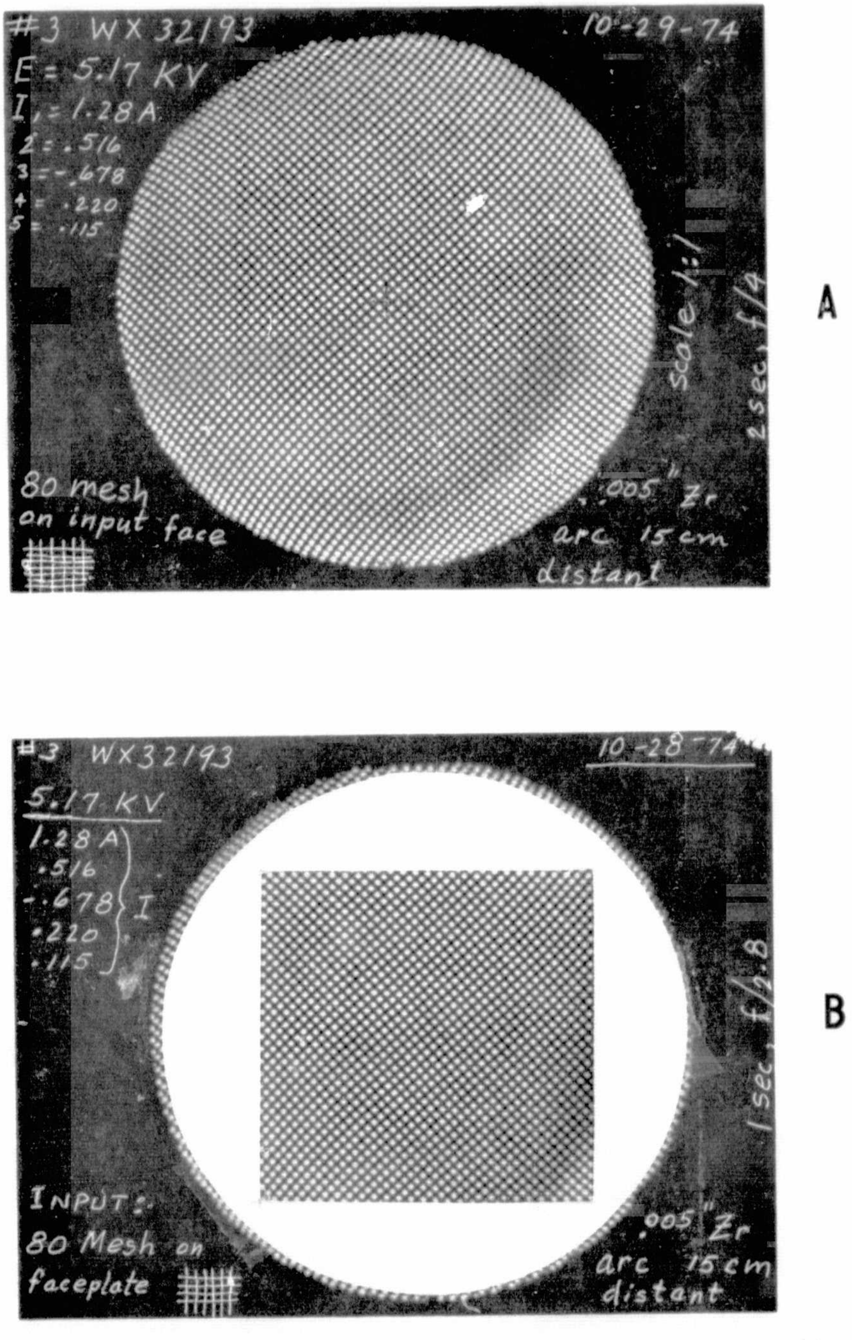

FIGURE 4.14 IT #3. 80 Line/Inch Mesh Imaged at M = 4.08

(a) Full Phosphor Diameter (8 cm)
(b) Masked to 50 × 50 mm.

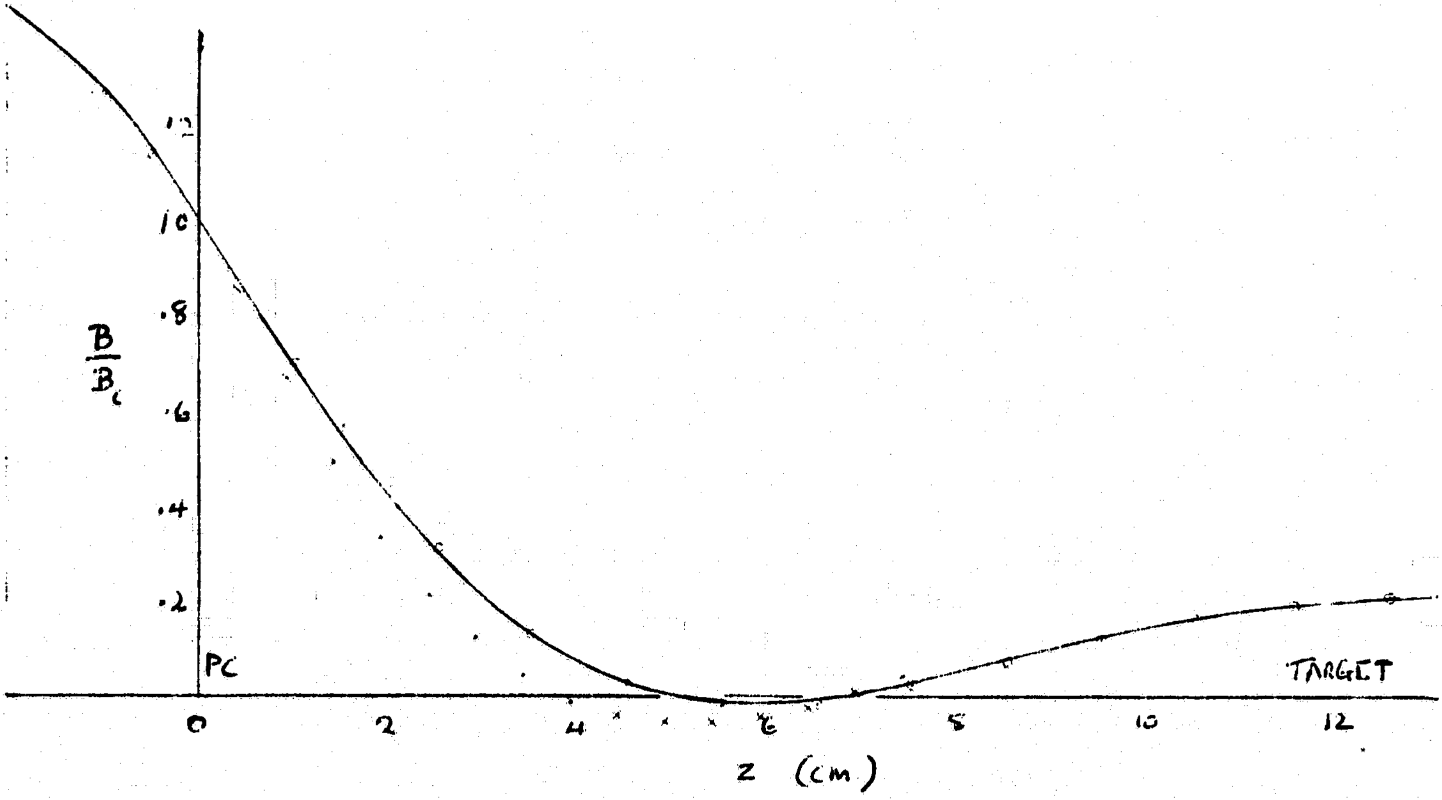

FIGURE 4.15 B-Field Distrbution for Magnification Test

(a) Full Curve - Computed Without Tube
(b) o - Measured Without Tube
(c) x - Measured With Tube

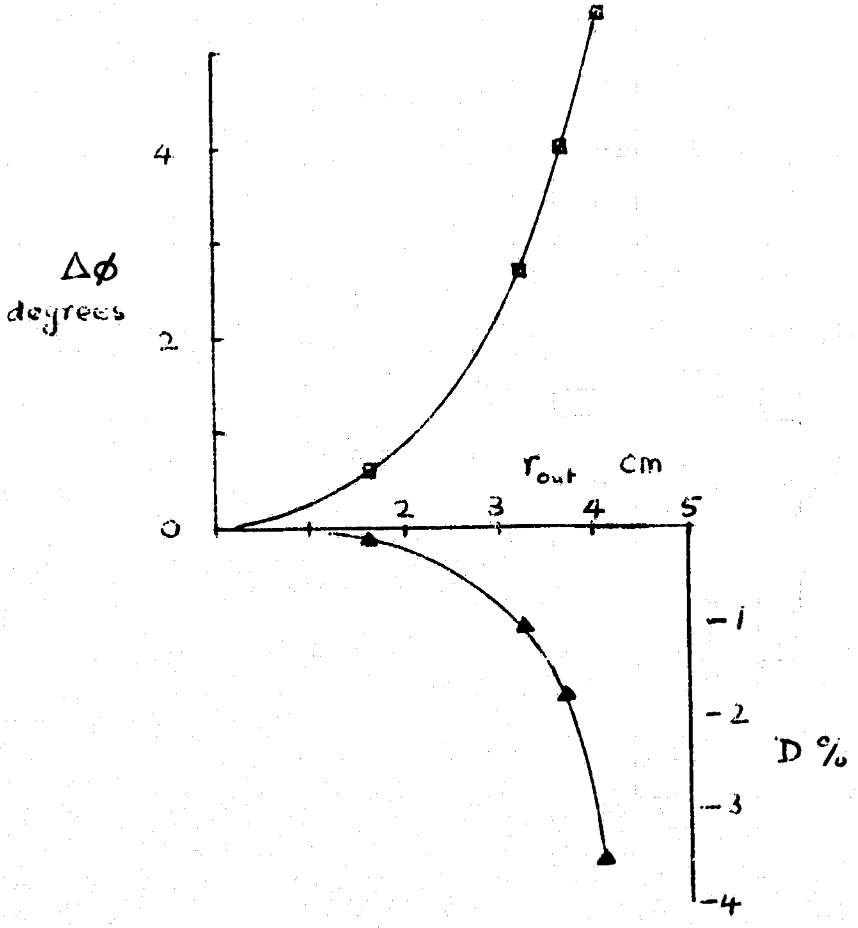

FIGURE 4.16 Computed Radial and S-Distortions for B-Field Curve (c) of Figure 4.15

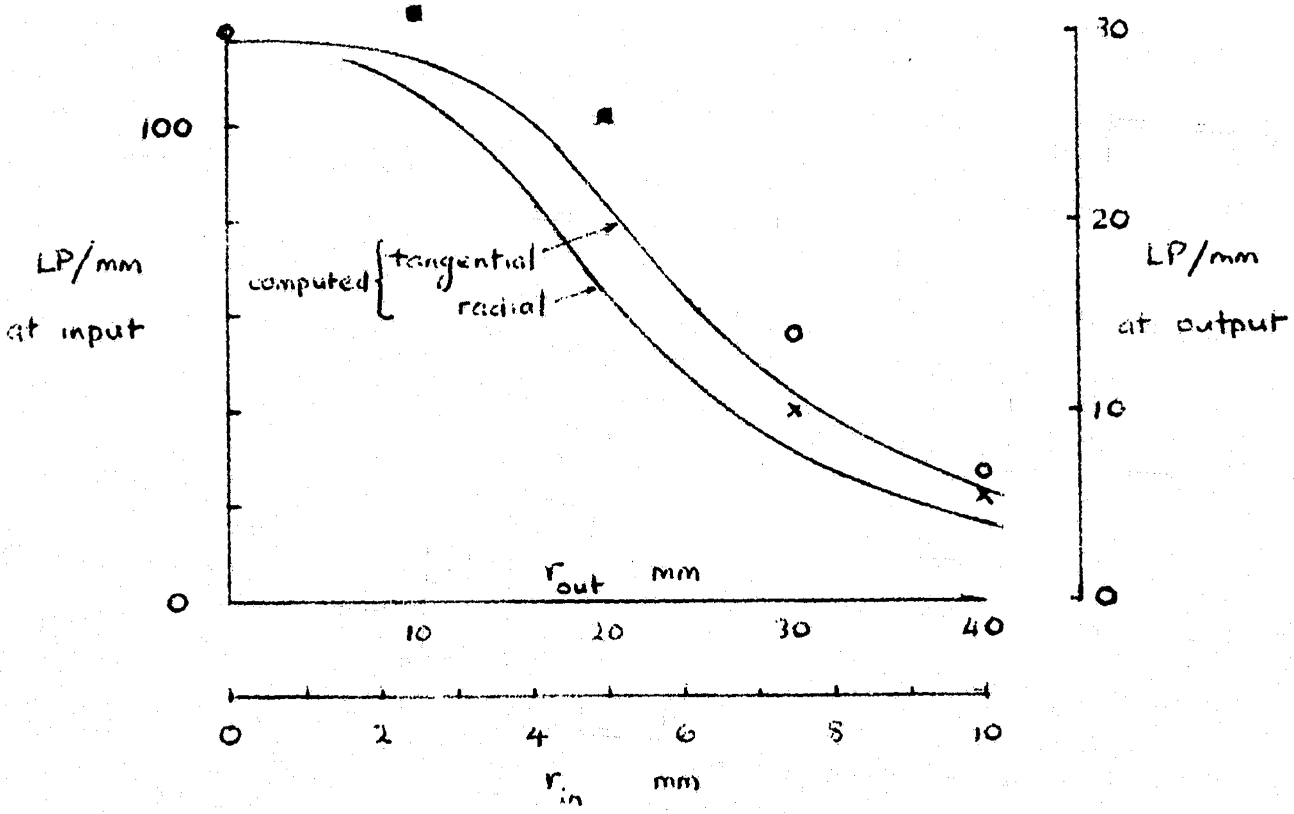

FIGURE 4.17 IT #3 Limiting Resolution Readings (5.17 KV) and Computed Estimates (6 KV), for M = 4

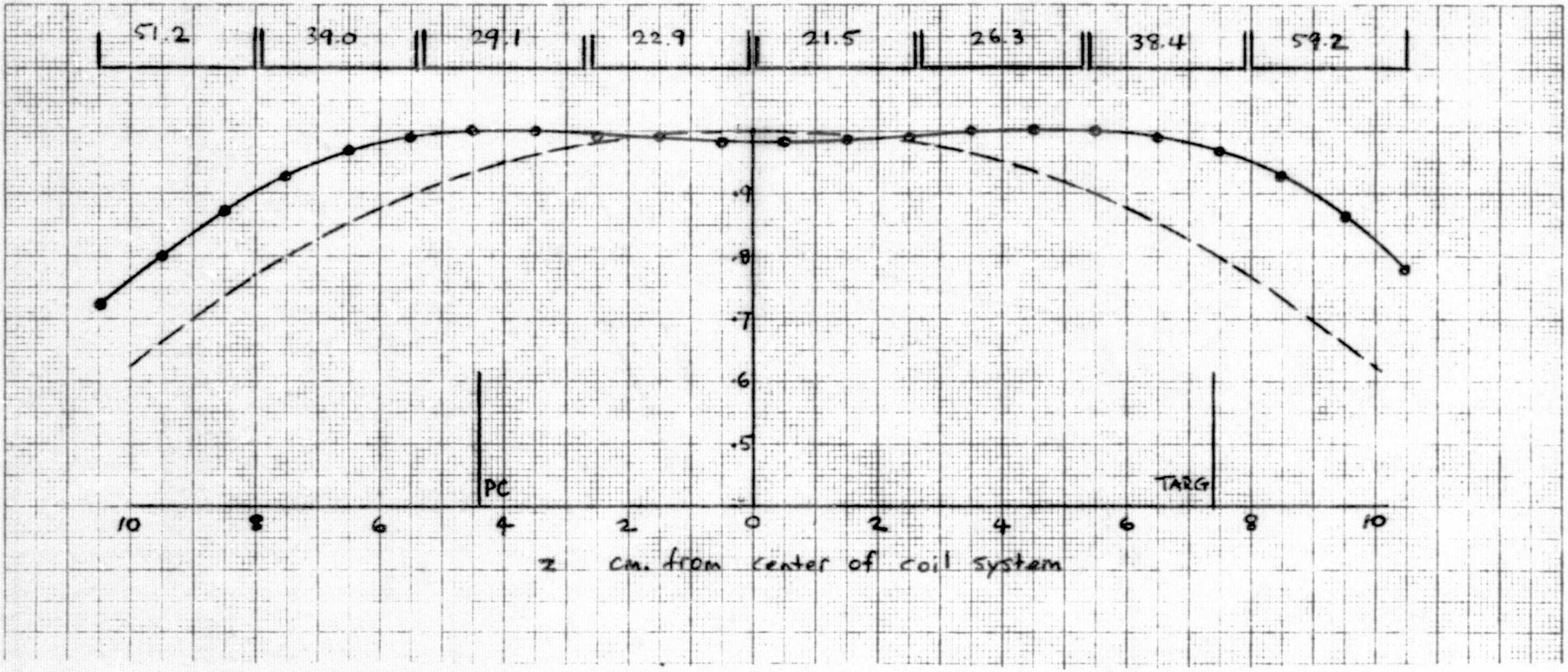

FIGURE 4.18 B-Field Distributions for M = 1

(a) Broken Curve - Equal Coil Currents
(b) Solid Curve - "Optimized" Coil Currents (Computed)
(c) o - "Optimized" Coil Currents (Measured) (Without Tube)

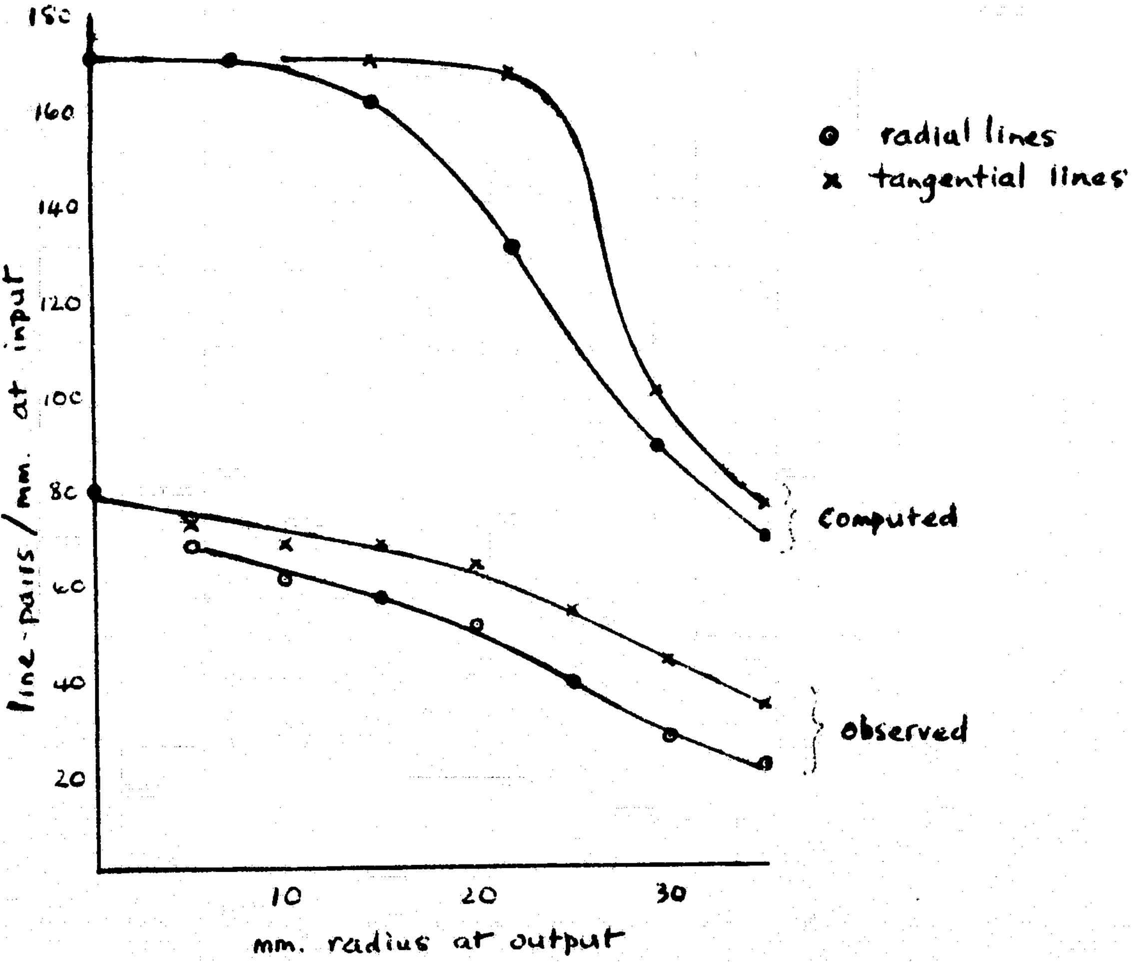

FIGURE 4.19 IT #3 Limiting Resolution with B-Field Distribution (b) of Figure 4.18 (7.8 KV)

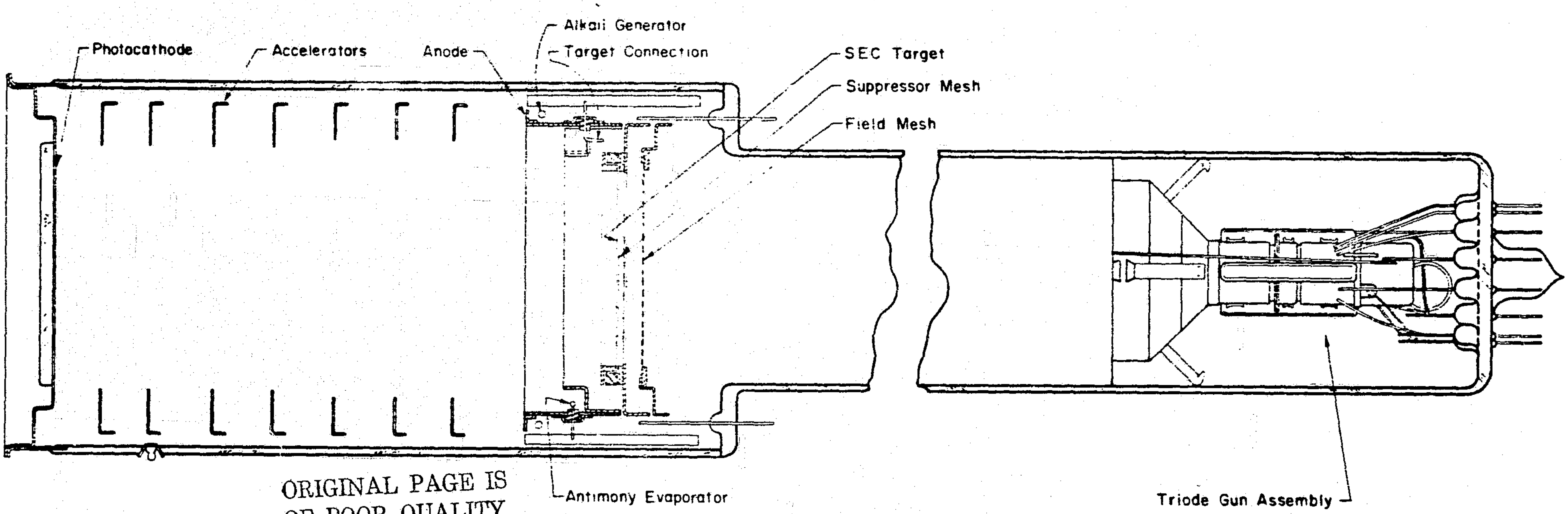

FIGURE 5.1 WX31958 S.E.C. Camera Tube Layout

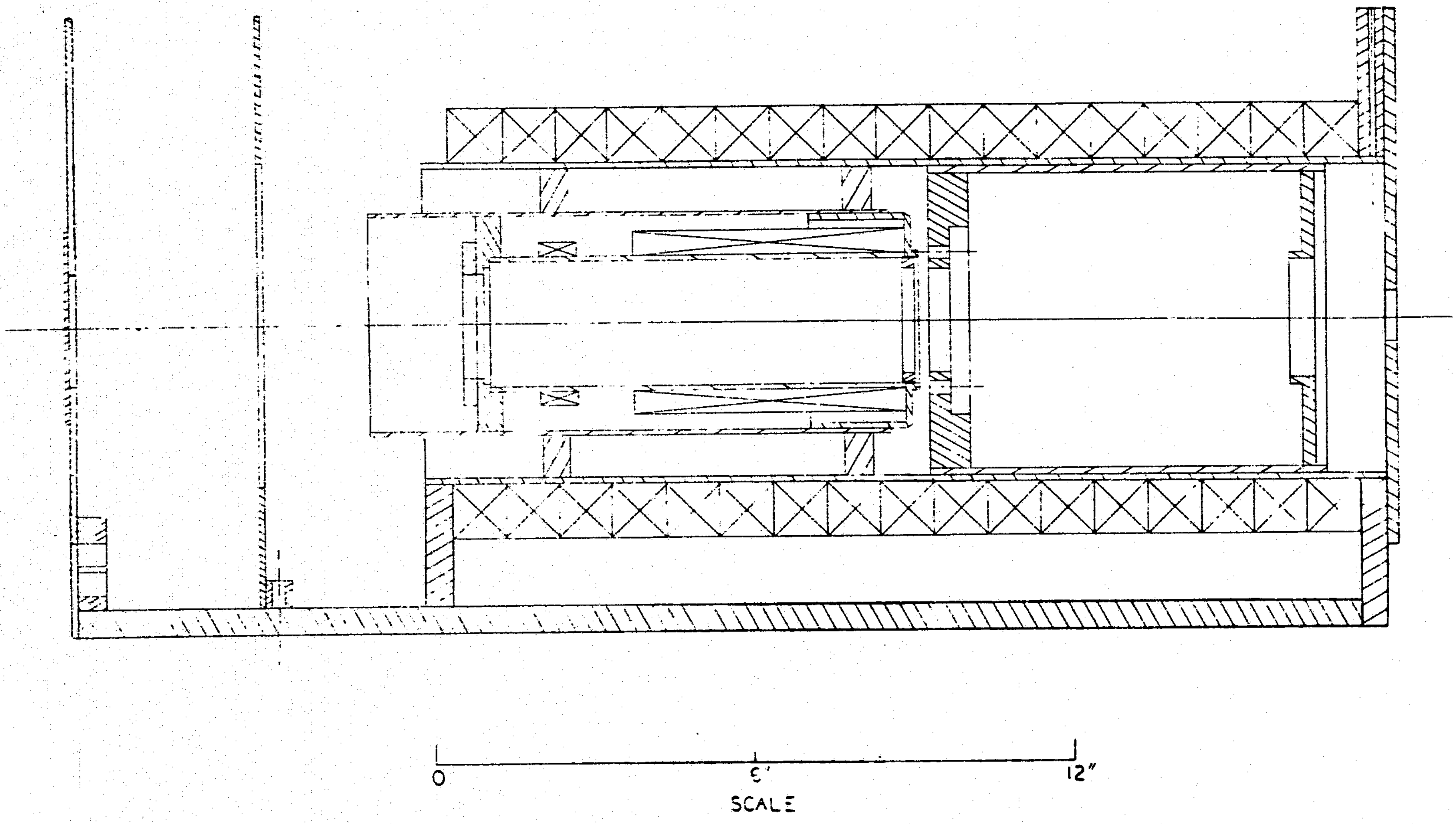

ORIGINAL PAGE IS
OF POOR QUALITY

FIGURE 5.2 Sectional Drawing of WX31958 Camera Head

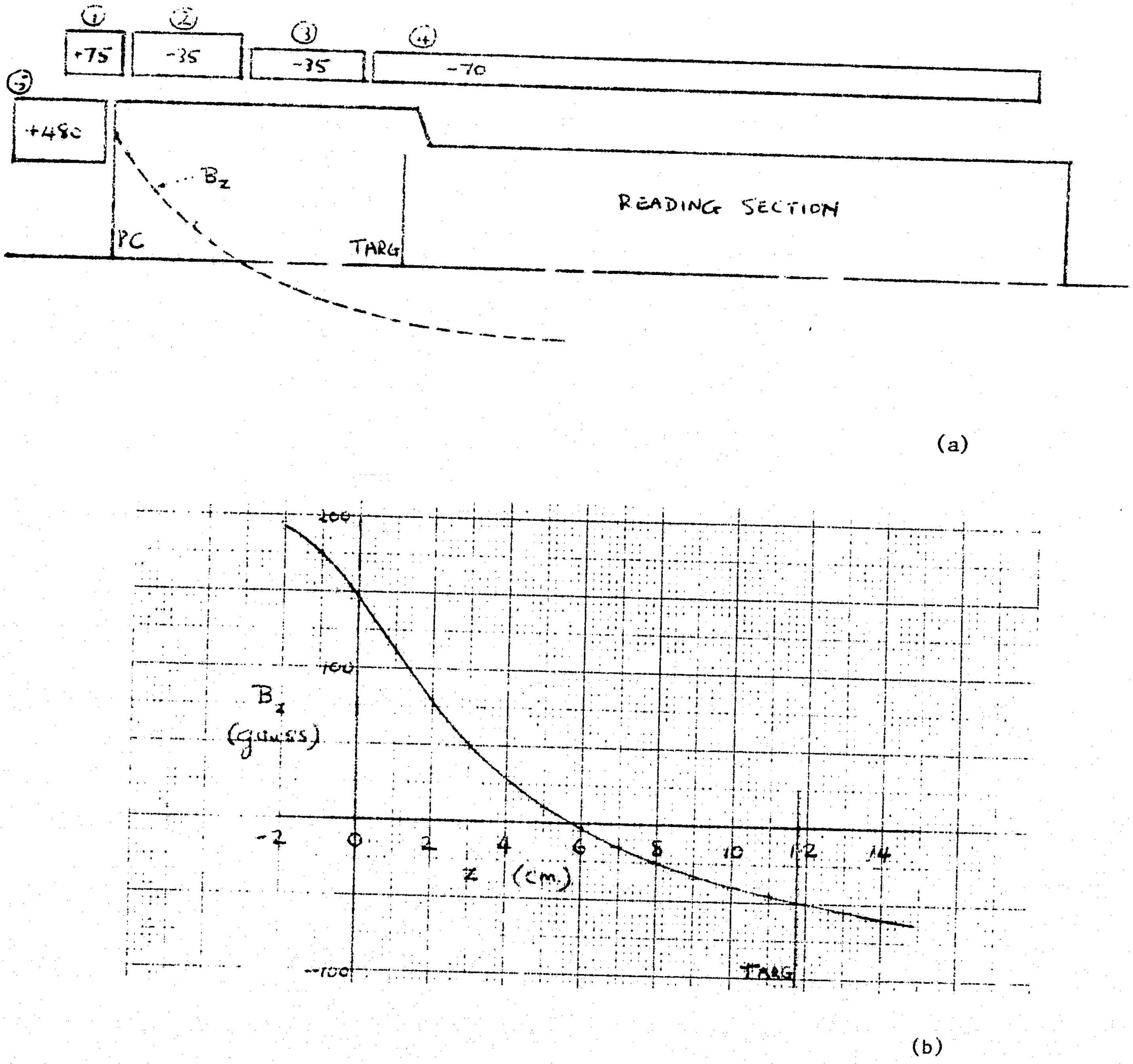

FIGURE 5.3 WX31958 Test

(a) Coil Strengths (amp/cm)
(b) B-Field Distribution Computed (Without Tube)

ORIGINAL PAGE IS
OF POOR QUALITY

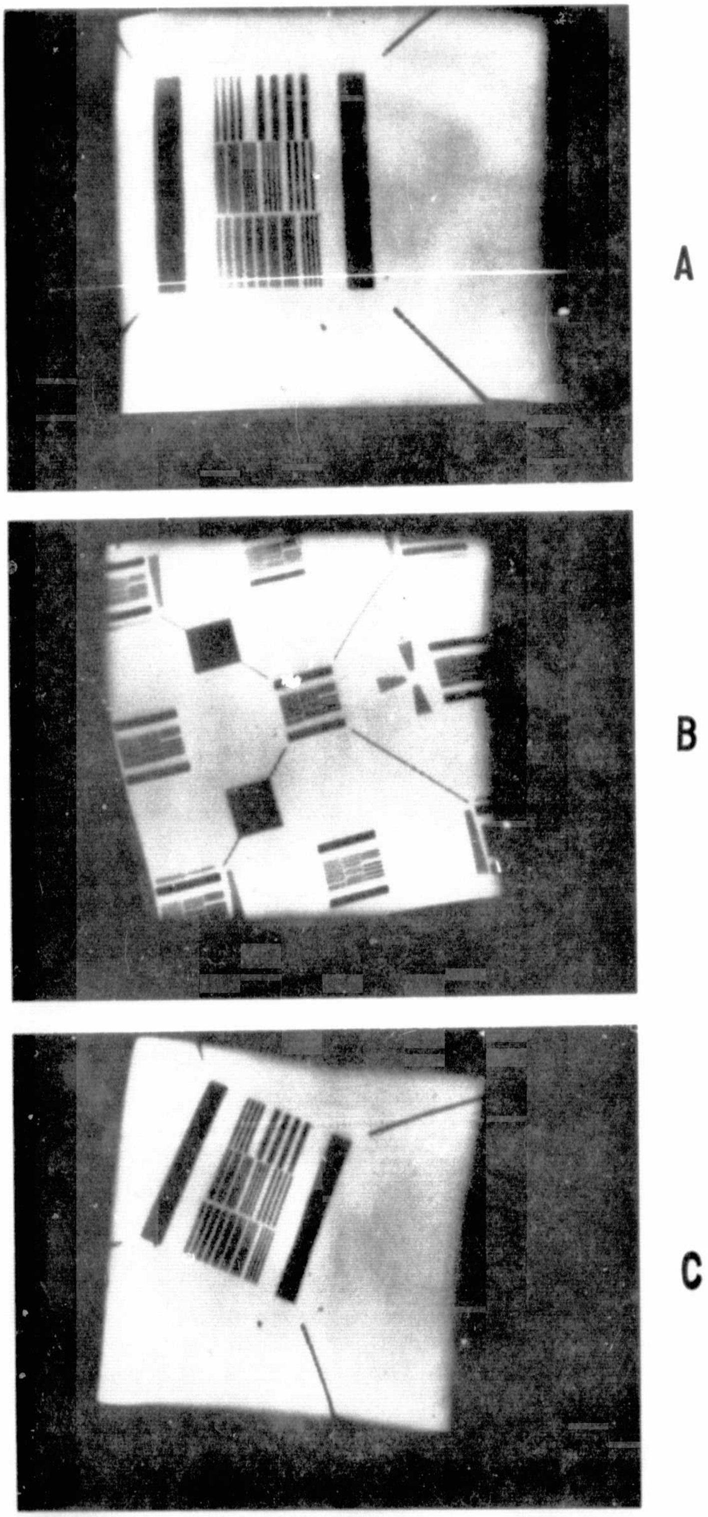

FIGURE 5.4 Monitor Screen Photographs of WX31958 Test

(a) M = 3
(b) M = .9
(c) M = 2.7

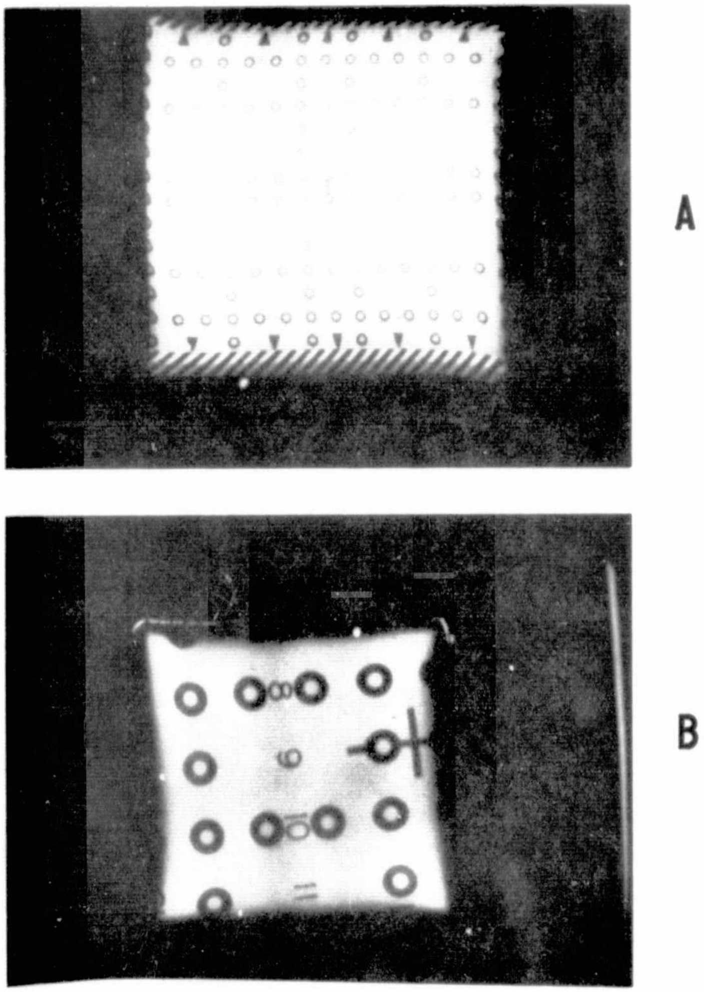

FIGURE 5.5 Monitor Screen Photographs of WX31958 Test

(a) $M = 0.9$

$V_{PC} = -8.1$ KV

$I_1 = I_2 = I_3 = I_4 = 2.9$ amp

$I_5 = 0$

(b) $M = 3.2$

$V_{PC} = -5.1$ KV

$I_1 = 2.9$ amp

$I_2 = -1.5$

$I_3 = -1.75$

$I_4 = -2.9$

$I_5 = 1.3$

Reading Section: $V_{G2} = 200$ $V_{G3} = 150$

$V_{mesh} = 400$ $V_{targ} = 17$

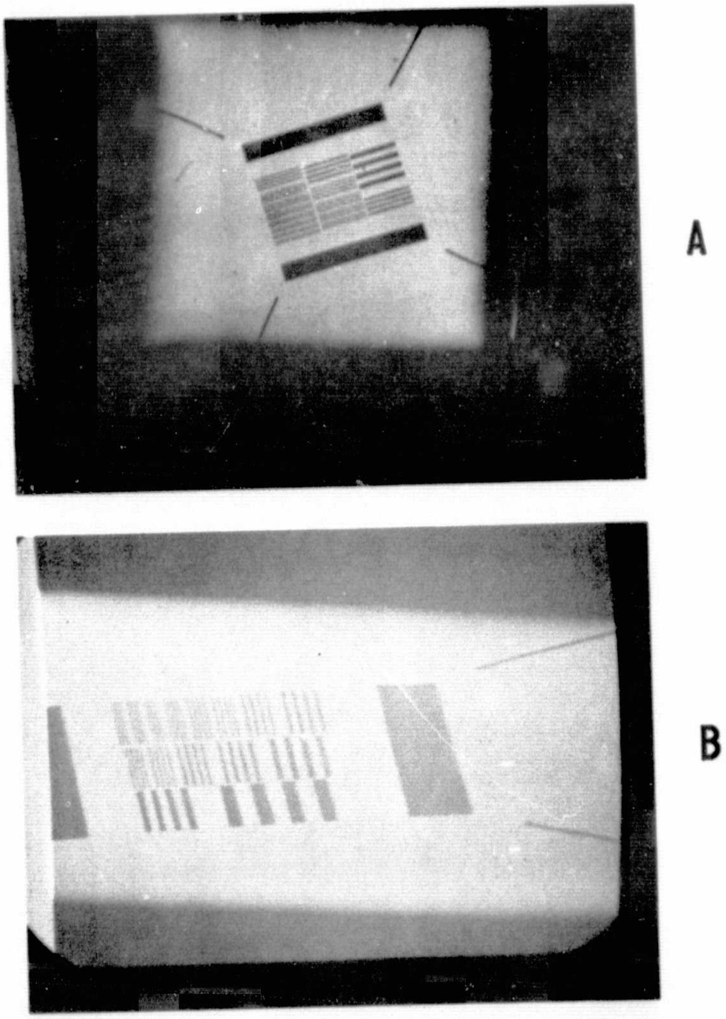

FIGURE 5.6 Monitor Screen Photographs of WX31958 Test

$V_{PC} = -5.2$ KV

$I_1 = 2.5$ amp

$I_2 = -.9$

$I_3 = -1.8$

$I_4 = -2.9$

$J_5 = 1.0$

Reading Section: $V_{G2} = 320$ $V_{G3} = 160$

$V_{mesh} = 300$ $V_{targ} = 15$

(a) OVERSCANNED

(b) LINE UNDERSCANNED

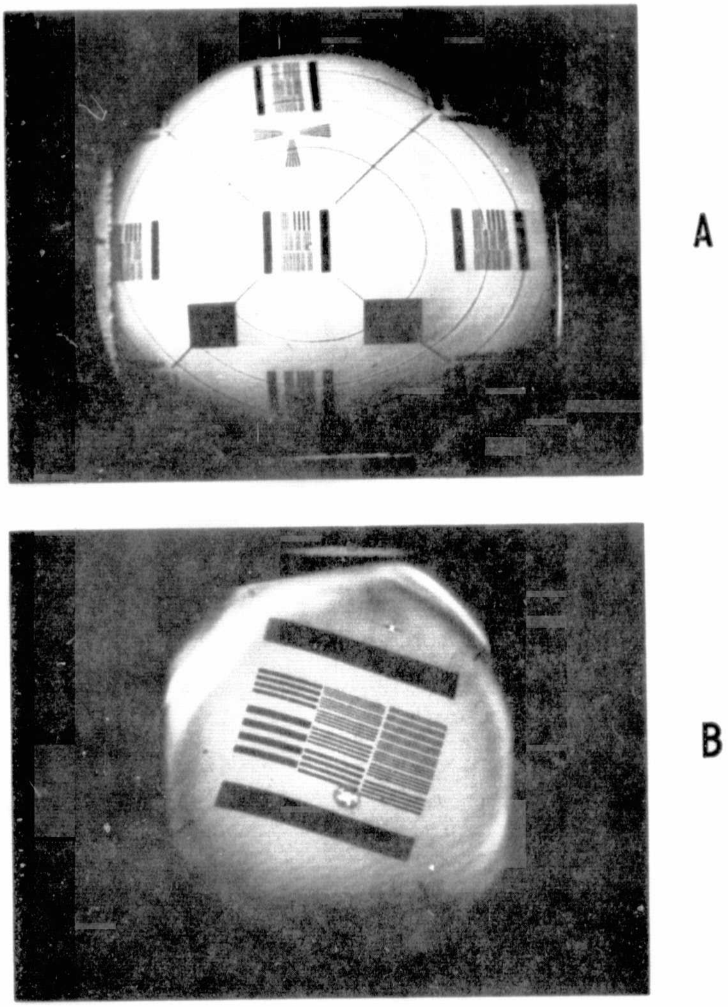

FIGURE 5.7 Monitor Screen Photographs of WX32193 Test

(a)

$M = 1.0$

$V_{PC} = -7.8$ KV

$I_1 = I_2 = 1.1$ amp

$I_{2A} = 2.1$

$I_3 = I_4 = 3.0$

$I_{4A} = 0.6$

Reading Section

$V_{G2} = 300$ $V_{G3} = 20$

$V_{mesh} = 360$ $V_{targ} = 15$

(b)

$M = 3.4$

$V_{PC} = -6.8$ KV

$I_1 = 2.5$ amp

$I_2 = I_{4A} = -.9$

$I_3 = -1.8$

$I_4 = -2.9$

$V_{G2} = 300$ $V_{G3} = 35$

$V_{mesh} = 370$ $V_{targ} = 15$

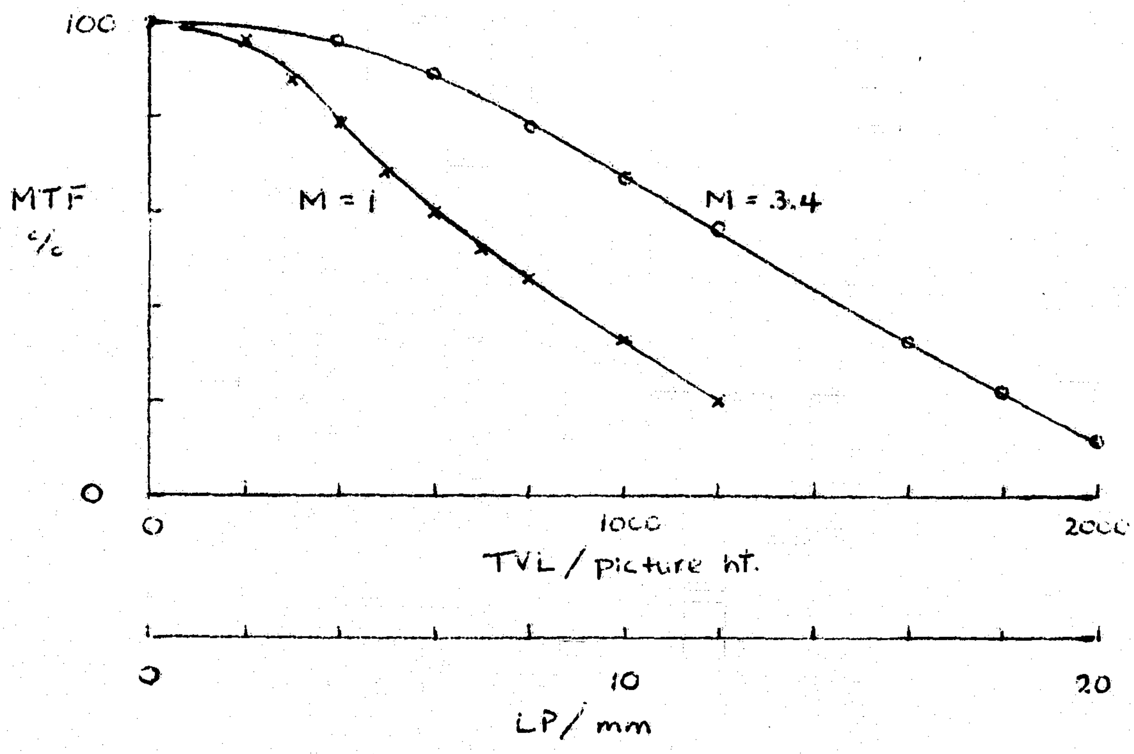

FIGURE 5.8 WX32193 Measured MTF Curves for Two Magnifications (Resolution Referred to Input). Operating Conditions as Defined in Figure 5.7

Dwg. 6250A15

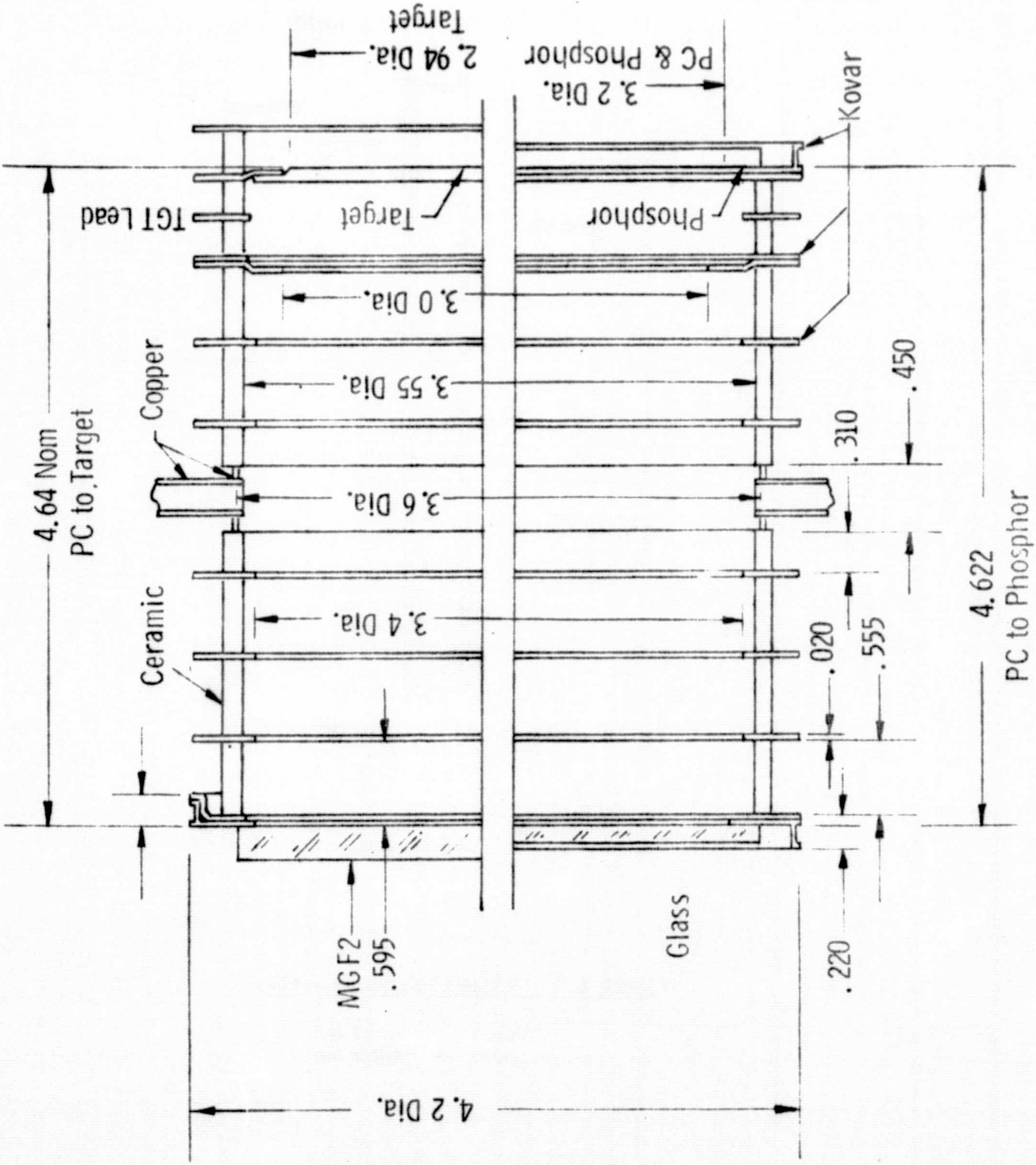

FIGURE 6.1 WX32193 Image Section Construction

Upper - For Camera Tube
Lower - For Image Intensifier

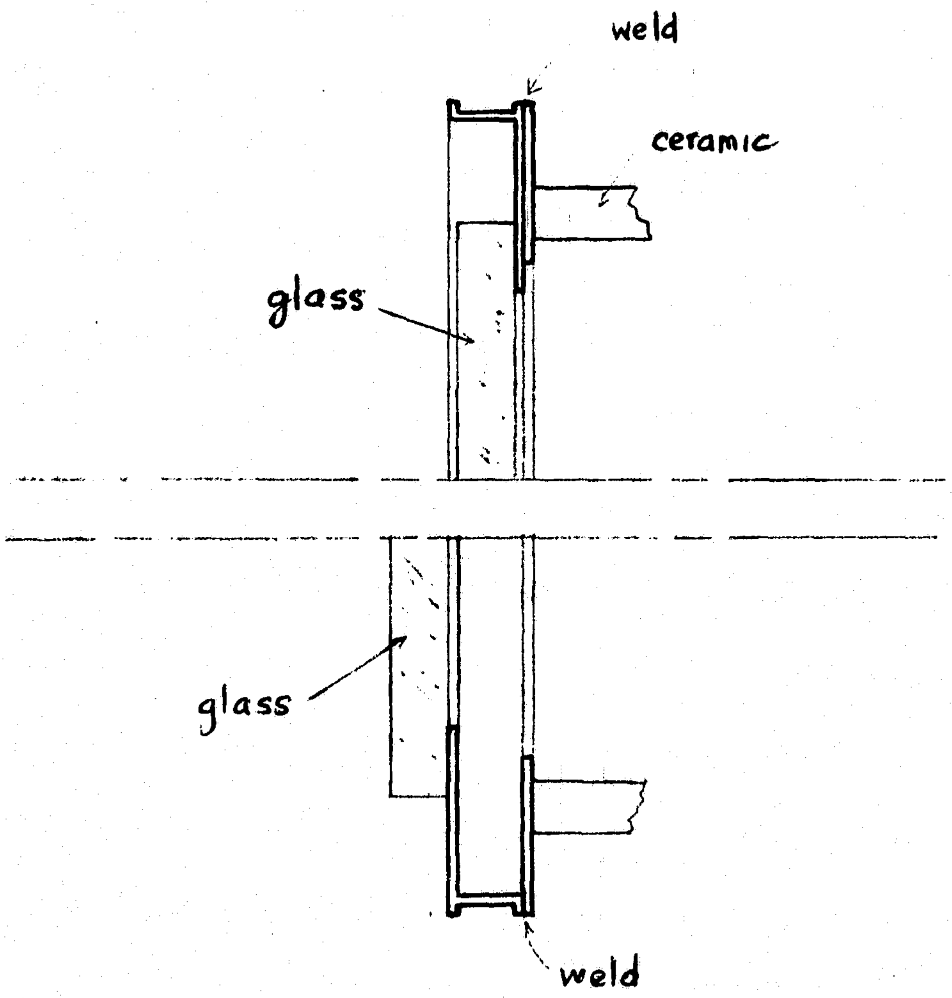

FIGURE 6.2 WX32193 Window Mounting

Upper - Original
Lower - Modified

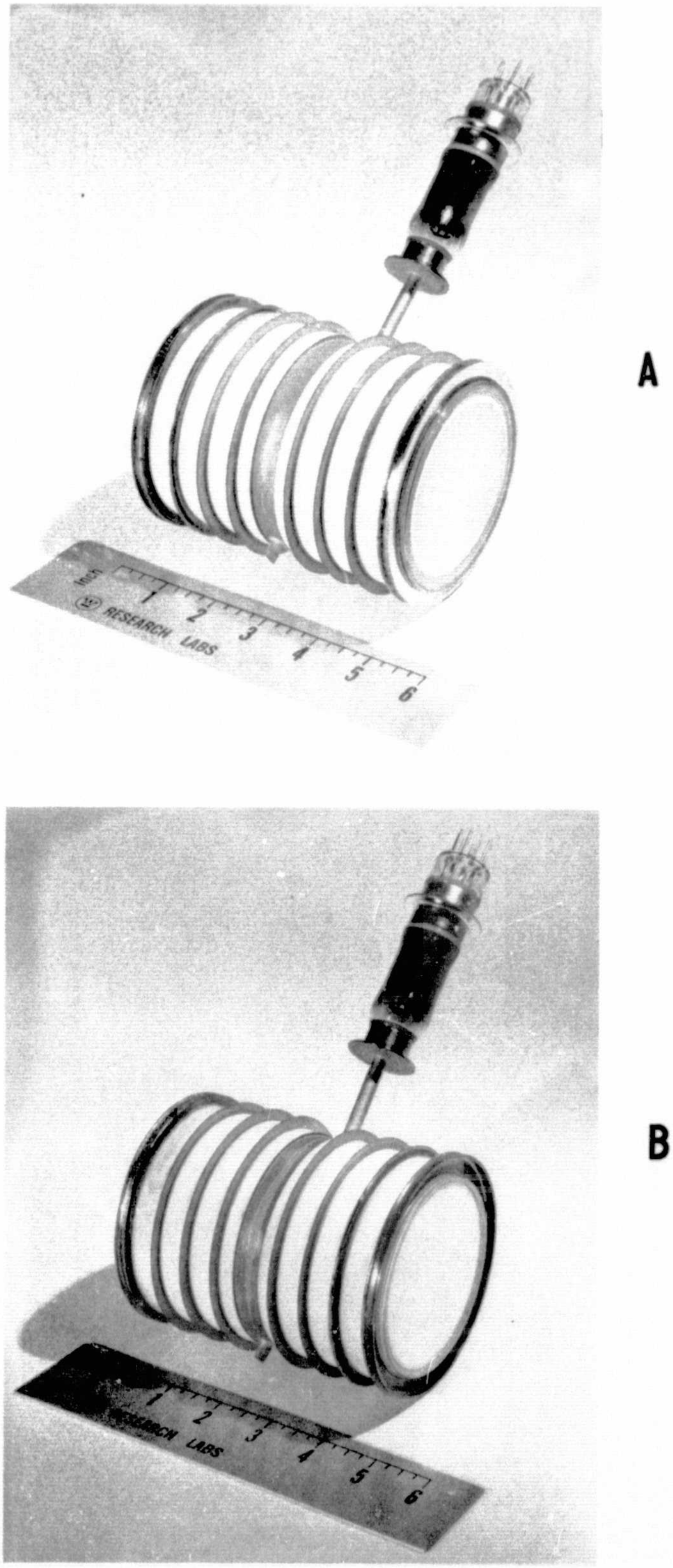

FIGURE 6.3 Image Intensifier #2

(a) Input End - Modified Window Mounting
(b) Output End - Original Window Mounting